

R-matrix theory for attosecond spectroscopy

vorgelegt von
B.Sc.-Physik und M.Sc
Danilo Simoes Brambila
geb. in Maringa, Brasilien

Von der Fakultät II – Mathematik und Naturwissenschaften
der Technischen Universität Berlin
zur Erlangung des akademischen Grades

Doktor der Naturwissenschaften
-Dr.rer.nat.-

genehmigte Dissertation

Promotionsausschuss:

Vorsitzende: Prof. Dr. Birgit Kanngießer
Berichterin/Gutachterin: Dr. Olga Smirnova
Berichter/Gutachter: Prof. Dr. Andreas Knorr
Berichter/Gutachter: Prof. Dr. Jonathan Tennyson

Tag der wissenschaftlichen Aussprache: 26. Februar 2016

Berlin 2016

Acknowledgments

I would like sincerely thank Olga and Alex for their guidance and support in the last 3 and half years. I had also awesome colleagues in MBI, it was great working with you guys.

I thank my family for their unconditional love and for enduring the long distance between us. This journey would not be possible without them.

I am also grateful for all the good friends that I made here in Berlin: Fede, Judith, Foudhil, Szymon, Nils, Henri, Chris, Jakov and others. Life would not be so beautiful without you guys.

Last, but not the least, I would like to thank Natalia for all her love and the long hours she spent in trains and planes from Berlin-Cologne-Berlin-Cologne...

Contents

1	Introduction	10
1.1	The time-scale of chemical reactions	10
1.2	Femtosecond spectroscopy	12
1.2.1	Time-resolved photoelectron spectroscopy	15
1.3	XUV sources	15
1.3.1	Free-electron Lasers (FEL)	17
1.3.2	High Harmonic Generation (HHG)	18
1.4	Attosecond electron dynamics	20
1.5	Theoretical methods in ionization	21
1.6	Outline of the thesis	23
2	Basic Scattering theory	25
2.1	Single channel scattering theory: short range potentials	26
2.2	Single channel scattering theory: the Coulomb potential	28
2.3	The R-Matrix theory	31
2.3.1	Approximate R-Matrix methods	33
2.4	Multichannel Scattering	35
2.4.1	Derivation of the close coupling equations	37
2.5	Resonances	39
3	Principles of quantum chemistry	41
3.1	Basic concepts in electronic structure calculations	42
3.1.1	Spin-orbital basis set	43
3.1.2	The Roothaan equations	44
3.1.3	Configuration state functions	46
3.2	Hartree-Fock method	46
3.3	Configuration interaction	47
3.4	Multiconfigurational and multireference methods	48

4	Photoionization of molecules	50
4.1	Differential cross sections and asymmetry parameters	51
4.2	Experiments	57
4.2.1	PEPICO	57
4.2.2	Adiabatic alignment and orientation	58
4.2.3	Field free alignment	58
5	Molecular R-Matrix theory and the UKRmol package	61
5.1	Molecular R-Matrix theory	62
5.1.1	Scattering states	62
5.1.2	Inner region	64
5.1.3	Outer and Asymptotic region	66
5.2	The UKRmol package	67
5.2.1	Target preparation	68
5.2.2	Inner region	68
5.2.3	Outer region	69
5.2.4	The UKRmol+ codes	70
5.3	Photoionization with the R-Matrix method	71
5.3.1	Expansion coefficients	73
5.3.2	Bound states and inner region dipoles	73
5.3.3	Calculating the dipoles	73
5.4	Photoionization with the UKRmol package	76
5.4.1	CDENPROP	76
5.4.2	DIPELM	77
6	Photoionization of molecules in the equilibrium geometry	81
6.1	Photoionization of N ₂	82
6.1.1	Molecular orbitals and target states	82
6.1.2	Inner and outer region	83
6.1.3	Partial photoionization cross sections and asymmetry parameters	83
6.2	Photoionization of CO ₂	85
6.2.1	Molecular orbitals and target models	86
6.2.2	Inner and outer region	87
6.2.3	Partial photoionization cross sections	87
6.2.4	Photoelectron angular distributions	89
6.3	Photoionization of NO ₂	94
6.3.1	Molecular orbitals and target models	94
6.3.2	Inner and region	95

6.3.3	Partial photoionization cross sections and asymmetry parameters	96
6.3.4	Photoionization dipoles	99
6.4	Discussion	102
7	Photoionization of NO₂ for a range of nuclear geometries for time-resolved photoelectron spectroscopy	103
7.1	The Born Oppenheimer approximation and beyond	105
7.1.1	Conical intersections and avoided crossings	106
7.2	Photoelectron spectroscopy with the R-Matrix method: case study of NO ₂	107
7.2.1	Molecular orbitals and target models	108
7.2.2	Inner and outer region	113
7.2.3	Total photoionization cross sections	114
7.2.4	Partial photoionization cross sections and asymmetry parameters	116
7.2.5	Dyson Orbitals	119
7.2.6	PADs	119
7.3	Discussion	121
8	R-Matrix with weak static fields	129
8.1	R-Matrix with static electric field	130
8.1.1	Inner region	131
8.1.2	Outer region	132
8.1.3	Asymptotic region	133
8.2	Resonance Analysis	133
8.3	$e - H_2^+$ scattering in a static electric field.	133
8.4	$e - He^+$ scattering and He photoionization in a static electric field.	136
8.4.1	Field free calculations.	136
8.4.2	The effect of a static electric field on the Rydberg series of He**	138
8.4.3	Photoionization of He	141
8.5	Discussion	142
9	Accurate photorecombination matrix elements for high harmonic spectroscopy	144
9.1	Theory	145
9.2	High high harmonic spectroscopy of CO ₂	148
9.2.1	Wavefunctions of CO ₂ and CO ₂ ⁺	149
9.2.2	Ionization	150

9.2.3	Propagation	151
9.2.4	Recombination	151
9.2.5	High harmonic spectra	152
9.3	Observation window in HHG: an example on He	155
9.3.1	Observation window of the high harmonic light	156
9.4	Discussion	157
10	Conclusions	159
Appendix A		162
A.1	Multipole expansion	162
Appendix B		164
B.1	Adaptations to the UKRmol package	164
B.2	STCFLD organization and input data	165

Zusammenfassung

Das XUV Licht, welches mithilfe neuartiger Quellen, wie Freie-Elektronen-Laser und High-Harmonic-Generation (HHG) verfügbar ist, eröffnet die Möglichkeit der Beobachtung, Initiierung und Kontrolle schnellster intramolekularer Prozesse. Bei Einwirkung von XUV-Licht emittieren Atome und Moleküle oftmals Valenz- oder sogar Rumpfelektronen durch Ein- oder Mehrphotonenionization. Die Winkel- und Energieverteilung der frei gewordenen Elektronen kodiert Information über das ursprüngliche Molekül. Die Menge an Informationen, die aus dem Photoelektronenspektrum gewonnen werden kann, ist optimal, wenn das Molekülensemble wird vor der Ionisation ausgerichtet wurde. Darüber hinaus können die Photoionisationsmatrixelemente im Ruhesystem des Moleküls auch verwendet werden, um die Erzeugung von HHG-Licht zu modellieren, da die Photorekombination, die eine Schlüsselrolle in der HHG spielt, einfach der Prozess der Photoionisation bei Zeitumkehr ist.

Die theoretische Beschreibung von Photoionisationsexperimenten und die Analyse der HHG-Strahlung erfordern eine hohe numerische Qualität der Matrixelemente für Photoionisation und Photorekombination im molekularen Ruhesystem. In dieser Arbeit wird die Photoionisation bzw. Photorekombination von mehratomigen Molekülen unter Verwendung der *ab initio* Multichannel-R-Matrix-Methode untersucht. Zu diesem Zweck haben wir neue Module für UKRmol (eine spezielle Software, für die Berechnung von Elektronenstreuung an mehratomigen Molekülen) implementiert, welche die Observablen bei Photoionisation berechnen. Wir prüfen die Qualität der Ergebnisse unserer Berechnungen durch den Vergleich mit den verschiedenen Berechnungen und experimentellen Daten für CO_2 , N_2 , NO_2 und He aus der Literatur. Wir untersuchen Photoionisation von Systemen, in denen Elektronenkorrelation von Bedeutung ist, z.B. wenn das nach der Photoionisation zurückbleibende Molekülion in einem angeregten Zustand oder einem sogenannten Satellitenzustand verbleibt. Wir berechnen auch die Photoionisation von NO_2 für eine Reihe von Molekülgeometrien, die für die zeitaufgelöste Photoelektronen-HHG-Spektroskopie relevant ist. Weiterhin untersuchen wir den Effekt eines schwachen, statischen, elektrischen Feldes auf die Photoionisation von He und H_2 . Abschliessend verwenden wir die Matrixelemente für Photorekombination, die wir mithilfe unserer UKRmol-Module berechnen, um HHG-Spektren von CO_2 und He zu untersuchen.

Abstract

The XUV light obtained from the new free electron lasers and high harmonic generation (HHG) sources have opened up the possibility of observation, initiation and control of the fastest intra molecular processes. Upon exposure to XUV light, atoms and molecules often ejects valence or even core electrons via single or multiphotoionization. The angular- and energy-resolved distribution of the ejected electron encodes sensitive information about the parent molecule. The amount of information that can be extracted from the photoelectron is optimal if the molecular ensemble is oriented prior to ionization. In addition, the photoionization in the molecular frame can be also used to model the emission of HHG light, since photorecombination, which plays a key role in HHG, is simply the time reversal of photoionization.

The theoretical description of photoionization experiments and the analysis of HHG light require a high quality calculation of the photoionization/photorecombination matrix elements in the molecular frame. In this thesis we investigate the photoionization/photorecombination of polyatomic molecules in the molecular frame using the *ab initio* multichannel R-Matrix method. To this end, we have implemented new modules in the UKRmol suite (a specialized software that previously dealt with electron scattering with polyatomic molecules) to calculate photoionization observables. We benchmark our codes by comparing our results with several other calculations and experimental data for CO₂, N₂, NO₂ and He. We investigate photoionization of systems where electronic correlation is important, such as when the photoionization leaves the residual ion state in an excited or a satellite states. We also calculate the photoionization of NO₂ for a range of molecular geometries, which is relevant for time-resolved photoelectron/high harmonic spectroscopy. In addition, we studied the effect of a weak static electric field on the photoionization of He and H₂. Finally, we use the photorecombination matrix elements obtained with the UKRmol codes for investigating the HHG spectra of CO₂ and He.

Parts of this thesis have been published in the following articles:

- **D. S. Brambila**, A. G. Harvey, Z. Masin, J. Gorfinkiel and O. Smirnova. "The role of multichannel effects in the photoionization of the NO₂ molecule: an ab initio R-matrix study". *Journal of Physics B: Atomic, Molecular and Optical Physics* 48, 245101, **2015**.
- **D. S. Brambila**, A. G. Harvey, Z. Masin, J. Gorfinkiel and O. Smirnova. "NO₂ molecular frame photoelectron angular distributions for a range of geometries using the R-matrix method". *Journal of Physics: Conference Series* 11, 112126, **2015**.
- O. Pedatzur, G. Orenstein, V. Serbinenko, H. Soifer, B. D. Bruner, A. J. Uzan, **D. S. Brambila**, A. G. Harvey, L. Torlina, F. Morales, O. Smirnova and N. Dudovich. "Attosecond Tunneling interferometry". *Nature Physics*, 11, 815819, **2015**.
- W. J. Brigg, A. G. Harvey, A. Dzarasova, S. Mohr, **D. S. Brambila**, F. Morales, O. Smirnova and J. Tennyson. "Calculated photoionization cross sections using Quantemol-N". *Japanese Journal of Applied Physics* 54, 06GA02, **2015**.
- A. G. Harvey, **D. S. Brambila**, F. Morales and O. Smirnova. "An R-matrix approach to electron photon molecule collisions: photoelectron angular distributions from aligned molecules". *Journal of Physics B: Atomic, Molecular and Optical Physics*, 47, 215005, **2014**.
- A. Rouze, A. G. Harvey, F. Kelkensberg, **D. Brambila**, W. K. Siu, G. Gademann, O. Smirnova and M. J. J. Vrakking. "Imaging the electronic structure of valence orbitals in the XUV ionization of aligned molecules". *Journal of Physics B: Atomic, Molecular and Optical Physics*, 47, 124017, **2014**.

Chapter 1

Introduction

1.1 The time-scale of chemical reactions

Improvements of our ability to measure the duration of events has been a key factor in the technological progress and economic prosperity since antiquity. One interesting example is the Egyptian astronomical calendar, which was entirely based on the motion of stellar bodies and could accurately predict periodic events such as the seasons of the year, solstices and eclipses. This enabled the Egyptian farmers to know, within an accuracy of days, the right time of the year to plant their crops on the shores of the Nile. In fact, not only the Egyptians, but also the Mayans, Chinese, Byzantine and other great civilizations have developed their own calendar, mainly for agricultural needs.

When Galileo first started to investigate the kinematics of bodies in the seventeenth century, he needed a time-resolution in the order of seconds for measuring events, such as the free fall of metallic balls from the top of the leaning tower of Pisa. To this end, he could have used his own heart beats, which has an approximate resolution from 0.8 to 1.2 seconds.

It was only in the nineteenth century, that mankind developed techniques, e.g., snapshot photography, chronophotography, and stroboscopy, that allowed measurements with time resolution in the subsecond scale. These new developments quickly arose the curiosity of physicists and chemists, and one of the many fundamental questions raised by the scientific community was the relevant time scales in chemical reactions.

In a chemical reaction, a molecule is brought out of equilibrium by an

external influence, e.g., excitation via electron scattering or photoionization. Subsequently, the atoms and electrons of the system are redistributed and evolve towards the reaction products. The first estimations on the duration of chemical reactions were done in 1935 by Polanyi and Evans [1], and also independently by Eyring [2]. They derived an explicit expression for the pre-factor of the following formula proposed by Arrhenius [3], which describes the change in the reaction rate with temperature

$$k = \frac{\mathbf{k}T}{h} K = \frac{\mathbf{k}T}{h} e^{-\Delta G_a/\mathbf{R}T} \quad (1.1)$$

where \mathbf{k} , \mathbf{R} and h are the Boltzmann's, gas and Planck's constant respectively, and ΔG_a is the Gibbs energy of activation of the reaction. At room temperature $h/\mathbf{k}T \approx 166$ femtoseconds ($= 10^{-15}$ s). Indeed, it was later confirmed that most of the chemical reactions occurs in a picosecond time-scale (10^{-12} s).

Even faster is the vibrational motion of the atoms that dictates the dynamics of a chemical reaction. As this motion is governed by the laws of quantum mechanics, its characteristic time-scales can be estimated by evaluating

$$T = h/\Delta E, \quad (1.2)$$

where ΔE is the energy difference between the eigenvalues of the vibrational Hamiltonian. Since for most of the molecules $\Delta E \approx 1$ meV, the typical time-scale of vibrational motion is in the range of 10 to 100 femtoseconds.

Beyond the femtosecond regime, we reach the time scale of electronic motion in a chemical reaction. As further discussed in chapter 7, the distribution of the electronic cloud plays a key role in chemical reactions, as it determines the potential that drives the vibrational motion of the atoms. The energy separation between different electronic states ranges from one to tens of eV, corresponding then, according to Eq.1.2, to time-scales in the attosecond regime (atto= 10^{-15}). Indeed, the Bohr model for the hydrogen atom estimates that, measured in atomic units, the translation period of an electron around a proton is

$$\Delta t = 2\pi n^3, \quad (1.3)$$

where n is the principal quantum number. Thus, for an 1- s orbital, the period of the electronic motion is about 144 attoseconds, only a small fraction of the period of a 800nm laser pulse ($T = c/800\text{nm} \approx 2.5$ fs), the experimental workhorse of most ultrafast experiments on atomic and molecular dynamics.

So far, we have discussed the time scales of the motion of the atoms and electrons in a chemical reaction, but we have not yet mentioned how one could possibly measure these ultrafast events. This is a challenging task, since even nowadays the fastest electronic switches have a time-response in the order of nanoseconds, i.e., at least two orders of magnitude slower than the total duration of a typical chemical reaction.

The breakthrough that revolutionized chronology, allowing the measurement of events beyond the nanoscale, was the rapid advance of laser light technology, right after the invention of the laser in the late 50s [4]. In 1966 De Maria and co-workers reported the generation of picosecond pulses using mode-locking techniques [5]. Later on in 1974, Shank and Ippen reported the generation of femtosecond pulses using dye lasers [6]. In the late 80's pulses as short as 8 fs were achieved in Bell Labs [7, 8], the shortest event produced and controlled by mankind until 2001, when subfemtosecond light pulses were measured for the first time [9].

What about measuring the attosecond electron dynamics in a chemical reaction? Fortunately, femtosecond lasers have addressed this issue via a rather unexpected process. Since the late 70's, experiments where atoms and molecules in the gas phase were exposed to an intense IR femtosecond laser pulse reported the generation of extremely high harmonics (sometimes hundreds of times the fundamental frequency), which could not be explained by conventional non-linear optics [10, 11, 12, 13]. A simple Fourier transform shows that the cycle of the radiation emitted by these unusual high harmonics has the duration of hundreds of attoseconds, paving the way for the generation of light pulses with the duration of 100's of attoseconds [9]. Just as the motion of stars enabled the Egyptians to count the seasons of the year, and the heartbeats of Galileo gave him enough precision to determine the laws of kinematics, femtosecond laser pulses have proved to be suitable for directly measuring vibrational motion in chemical reactions, and also, fortuitously, electron dynamics.

1.2 Femtosecond spectroscopy

Shortly after the first reports on the generation of laser pulses with a duration in the femtosecond regime, Ahmed Zewail and co-workers pioneered the application of femtosecond lasers to monitor the vibrational motion in chemical reactions via pump-probe experiments. In a pump-probe experiment, a

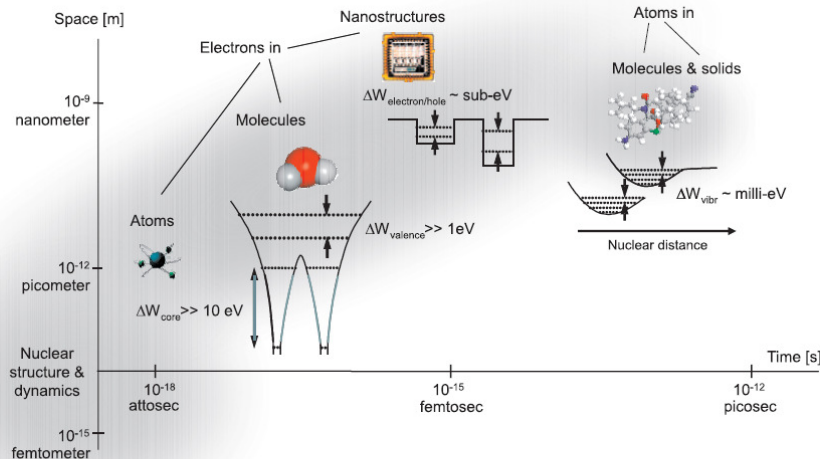


Figure 1.1: Time and space scales ranging from the vibrational to the electronic motion of for molecules. Taken from [14]

femtosecond laser pulse is split into two different optical paths. The pulse going through the short optical path is used to pump the molecule from the initial ground to an excited state at $t = 0$, creating a wavepacket consisting of a coherent superposition of the energetically accessible electronic and vibrational eigenstates of the molecule. As the chemical reactions evolves towards its products, the femtosecond pulse going through the long optical path probes the subproducts of the reaction via a variety of process (e.g., laser induced fluorescence, multiphoton ionization or photoionization), depending on the particular characteristics of the system under investigation. By varying the time-delay between pump and probe pulses, one can then monitor the progress of the chemical reaction.

The first demonstration of a femtosecond pump-probe experiment was performed by Scherer and co-workers [15], who investigated the transient dynamics of



After exciting the system with a 308nm femtosecond pulse, they probed the quantity of CN at different times of the reaction via laser induced fluorescence.

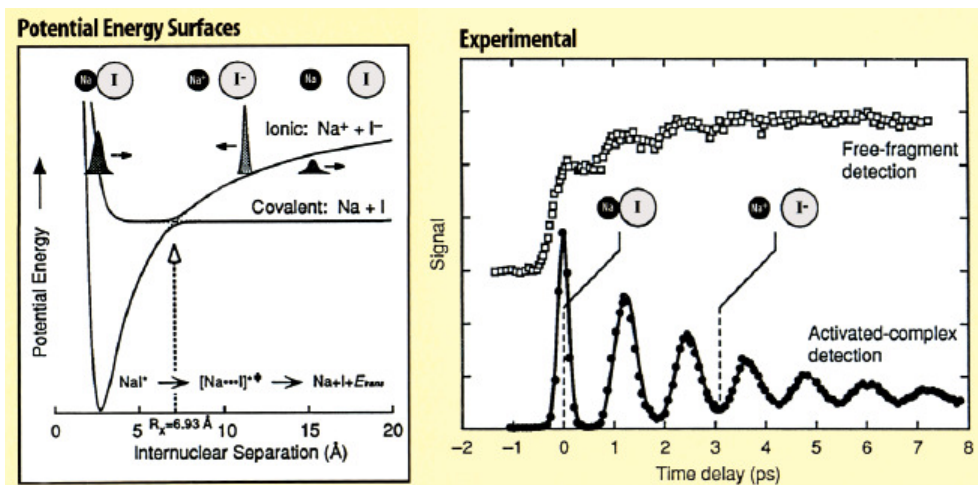


Figure 1.2: Ionic and covalent energy surfaces from NaI (left), and the experimental measurement of the dissociation of NaI into $\text{Na}^+ + \text{I}^-$ (right) with time for a femtosecond pump-probe experiment. Adapted from [16]

In a subsequent work, Rose and co-workers [17] analyzed the photochemistry of the NaI molecule. In this experiment, the reaction is started by creating a wavepacket via photoexcitation of NaI from the ground covalent to the first excited ionic surface, which has a well shape and an avoided crossing with the covalent surface at a Na-I distance of 6.93 \AA . The wavepacket then starts to oscillate on the ionic surface (see Fig.1.2). Whenever the wavepacket approaches the avoided crossing, part of it migrates to the covalent surface and evolves towards dissociation. By probing the quantity of NaI molecules at different time-delays between pump and probe pulse, Rose and co-workers monitored the rate at which the wavepacket is transferred from the ionic to the covalent surface.

These two pioneering works on ICN and NaI demonstrated the power of femtosecond spectroscopy. Since then, pump-probe experiments have become a well established tool applied for studying a wide variety of systems and processes such as the dynamics of bond breaking [18, 19, 20], isomerization reactions [21, 22, 23], valence structure isomerization [24, 25], reactive intermediates [26], intramolecular electron transfer and folding reactions [27, 28] and tautomerization reactions [29], among others (for a more complete list of applications see [30, 16, 31, 32]). Ahmed Zewail received the 1999 Nobel prize in chemistry for his pioneering work in femtochemistry.

1.2.1 Time-resolved photoelectron spectroscopy

The first pump-probe experiments relied either on multiphoton ionization or laser induced fluorescence as a probe of the wavepacket dynamics [30]. Both of these techniques, require that the wavelength of the probe pulse is matched to a given transition of the monitored reaction product. Consequently, in the early days of femtochemistry experimentalists were restricted to accessing a limited range of the reaction coordinates.

In this context, J. M. Smith and co-workers proposed to use photoelectron spectroscopy as a probe of the reaction dynamics [33, 34] (referred from now on as TRPES: time-resolved photoelectron spectroscopy). There are important advantages in using such a technique: (i) photoionization is always an allowed process, thus it can be used to probe a large region of the reaction coordinates, depending on the frequency-tunability of the probe pulse, (ii) no prior knowledge on the spectroscopy of the molecule is necessary in the probing step, (iii) an XUV photoionizing light can be theoretically treated as a perturbation, in contrast to high intensity multiphoton ionization, and (iv) measuring the photoelectron angular distribution for the ionization of valence electrons can give insights on the chemically active electronic orbitals. Maximum information from photoionization can be obtained by measuring the photoelectron and photoion in coincidence, allowing in some cases the evaluation of the photoelectron angular distributions in the molecular frame (see further details in Chapter 6).

For many years, the advances in the resolution of TRPES experiments were backed by the development of femtosecond laser light technology. In 1994, Nisoli and co-workers demonstrated that optical parametric amplification (OPA) could generate tunable radiation in a wavelength from 1200 to 2600nm [35]. In 1997, Wilhelm and co-workers have successfully generated tunable radiation from 480 to 750nm using nonlinear OPAs (NOPA) [36]. Both of these techniques can deliver femtosecond pulses ranging from 50 to 100 fs, that are short enough to time resolve most of the TRPES experiments.

1.3 XUV sources

Even though using femtosecond laser light as a probe in TRPES experiments has revealed in great detail the transient of many chemical reactions (see [34] for an extensive list of applications), the new broad band free electron laser

(FEL) and high harmonic generation (HHG) sources deliver radiation that allow experimentalists to probe chemical reactions via TRPES in the full reaction coordinates with unprecedented resolution.

The new dedicated FEL facilities can deliver coherent polarized radiation with a bandwidth between 0.1nm to 100nm, and pulse duration below 100fs. This opened up an astonishing number of new opportunities in TRPES [37, 38, 39, 40] and other interesting applications, such as: (i) low wavelength photons can be used for inner shell or core ionization of atoms and molecules, a process that is commonly followed by Coulomb explosion, thus allowing direct measurement of the time dependent structural dynamics of the system [41, 42, 43]; (ii) upon inner or core shell ionization, the outgoing electron can diffract with the atoms of the molecule, providing real time information on the molecular geometry [44, 45, 46]; (iii) the high photon flux in FEL can be used for the investigation multiphoton-ionization processes [47, 48, 49, 50, 51]; (iv) the VUV radiation from FEL is intense enough for ionizing ultradilute samples, giving insight on the interaction between high energy photons with cold atoms and molecules [52, 53, 54]; (v) the angstrom wavelength of the FEL sources can be used for the time-resolved imaging of large biological molecules via elastic photon scattering together with diffractive and coherent imaging techniques [55, 56]; and (vi) inner shell ionization via FEL can be combined with IR pulses that can drive the continuum electron back to the atomic or molecular target. In this case, recombination with deep valence shell will result in an emission of attosecond light in the KeV regime [57, 58].

HHG can also provide a broad band polarized coherent light in the XUV regime, and under certain conditions can reach pulse durations in the order of 100s of attoseconds. In contrast to the dedicated multi-billion euros FEL facilities, HHG is a table-top XUV source, widely available in many laboratories. There are several successful applications of high harmonic light as a pump or a probe in TRPES [59, 60, 61, 62]. Note that the short duration of the pulses generated by HHG can also give access to attosecond electronic dynamics as will be shown later in section 1.4.

In the next two sections, we discuss in further details the radiation obtained from free-electron lasers and HHGs sources.

1.3.1 Free-electron Lasers (FEL)

The history of free electron lasers starts at 1898, when Alfred Lienard predicted that the transverse acceleration of electrons results in the emission synchrotron radiation [63]. Only 50 years later when the first cyclotrons facilities were ready for operation, experimentalists were able to observe for the first time the emission of an extremely bright incoherent synchrotron radiation with a large bandwidth, upon transverse acceleration of electrons towards the relativistic limit using magnetic undulators. Synchrotron radiation was in fact a severe drawback for the first generation of cyclotrons, since it consumed a huge amount of energy, thus limiting the energy available for the acceleration of the electrons. In fact, to avoid these energy losses, since the mid 60's cyclotron facilities started to accelerate protons instead of electrons.

Twenty years after the first observation of synchrotron light, scientists started to explore the unique properties of this radiation for investigating the electronic structure of atoms, molecules and solids [64]. The first dedicated synchrotron radiation facility, TANTALUS in the University of Wisconsin-Madison, was ready for operation in 1968 and served the scientific community for almost 20 years. Since then, over a 100 synchrotron facilities have been constructed all over the world ¹. Despite the great utility of synchrotron light, it was only after 1994 with the 3rd generation of synchrotron facilities that most of the technical challenges were surpassed and synchrotron light became a popular tool for the scientific community [65]. In the early 2000s, new designs of synchrotron facilities were proposed, promising the emission of coherent radiation based on the self-amplified spontaneous emission (SASE) lasing principle [66]. Moreover, the brilliance (units of photons/s/mm²/mrad²/0.1%bandwidth) of these new light sources would surpass the 3rd generation of synchrotron sources by a factor of 10⁹. This new generation of synchrotron facilities are often simply referred to as free-electron lasers (FEL).

There are currently three FEL facilities in operation: FLASH in Hamburg since 2005, LCLS in Stanford since 2009, and SACLA in Harima, Japan since 2012. FLASH delivers radiation from 44nm to 5nm with a peak brilliance of 10²⁸. The LCLS and SACLA can reach to wavelengths in the Ångstrom regime, with a peak brilliance of 10³³. FEL sources also have a pulse duration below 100fs, reaching down to 7fs in LCLS, but a repetition rate of only

¹complete list at https://en.wikipedia.org/wiki/List_of_synchrotron_radiation_facilities

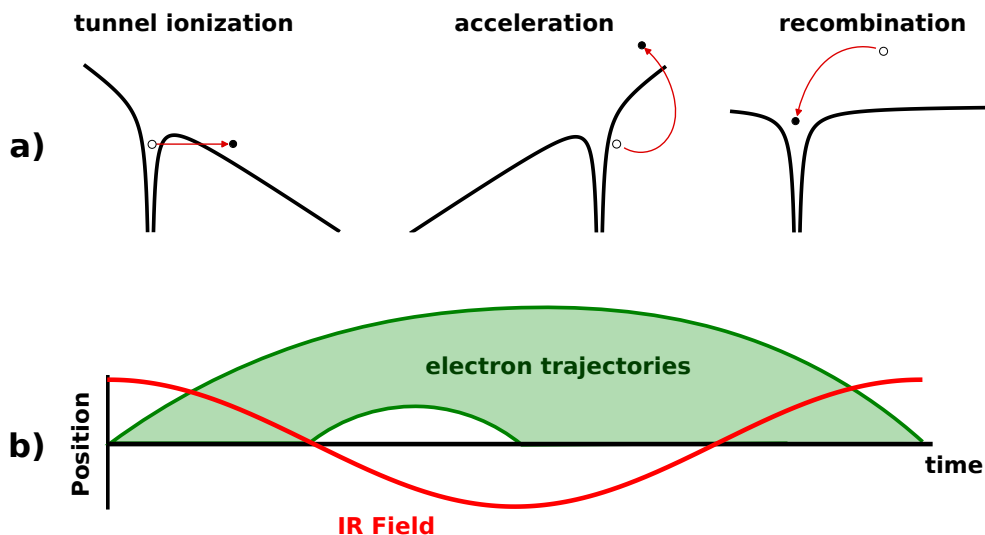


Figure 1.3: The semiclassical three step model. a) Tunnel ionization, acceleration and recombination in the presence of a strong IR-field. b) Trajectories of the continuum electron in units of the laser cycle.

120Hz (3^{rd} generation synchrotron have repetition rates of 1MHz). This issue is addressed by the new european XFEL facility in Hamburg, which is planned to operate at repetition rates of 27kHz in the sub-angstrom regime and is scheduled to be opened for the scientific community in 2017.

1.3.2 High Harmonic Generation (HHG)

In the first application of ruby lasers in non-linear optics in 1961, Franken and co-workers demonstrated the generation of the second harmonics by sending a high intensity ruby laser light into a quartz crystal [67]. This effect was later explained by Kleinman as the simultaneous absorption of two photons with the same fundamental frequency (f_0) and a subsequent de-excitation to the initial ground state, generating then a third photon with frequency $2f_0$ [68]. The same principle is valid for the generation of higher order harmonics, i.e., for the generation of the third harmonics 3 photons must be absorbed, for the fourth harmonic 4 photons, etc. Note however that a high laser intensity is needed in order to produce high order harmonics, since the efficiency of the up-frequency conversion process is suppressed as

the the number of simultaneously absorbed photons increase [69].

Since the late 1970's, experimentalists have observed the generation of double digit harmonics after the exposure of atomic or molecular gases to an intense femtosecond IR laser field [10, 11, 12, 13]. In addition, the experimental data has shown that the harmonic amplitude decreased for low order harmonics, but then after a certain frequency f_t , becomes nearly constant, followed by a sharp cut-off at a frequency f_c . This unique behavior intrigued the atomic and molecular physics community, since no one expected the simultaneous absorption of so many photons. In fact, the high order harmonics generated by these experiments would correspond to the absorption of more photons than necessary for the ionization of the target atom or molecule (for a 800nm laser light and an atom or molecule with an ionization potential of 15eV, the continuum is reached already by the 10th harmonic), in contrast to the expectation that after the molecule is ionized, the free electron should stop absorbing photons [70].

In 1993 P. Corkum proposed the following three-step mechanisms for the generation of high harmonics [71]: (i) the electron tunnel through the laser distorted coulomb field, (ii) is driven by the laser field in the continuum, and (iii) returns and recombines to the parent ion with a maximum kinetic energy of $3.17U_p + I_p$, where I_p is the ionization potential and $U_p = F^2/4\omega^2$ is the ponderomotive energy of the oscillating electron with F and ω being the electric field strength and frequency of the laser respectively. The three step model is remarkably simple and is derived from the classical Newtonian equations of motion. Later on, a full quantum theory developed independently by M. Lewenstein *et. al.* [72] and W. Becker *et. al.* [73], has shown that the exact cut-off formula is $3.17U_p + 1.32I_p$.

We will now consider the HHG process for ionization occurring in the first quarter of the IR laser cycle shown in Fig.1.3. The classical three step model predicts that the recombination window starts at $t = T/4$ (T is the laser period) and can extend up to several laser cycles. Since electron trajectories that travel in the continuum for longer than a laser cycle are very poorly phase matched [71], the strong signal in HHG occurs for recombination times roughly in the interval $T/2 < t < T$ revealing the subcycle duration of the HHG process. As the HHG is coherent, the summation of the light emitted from each of the target atom or molecule adds up constructively to generate a strong harmonic light (for more details about phase matching see, e.g., [69]).

In many of the HHG experiments the driving IR laser pulse has a dura-

tion of tens of femtoseconds, thus, one observes the formation of a train of attosecond pulse that is the sum of all attosecond bursts produced at different half-cycles of the laser. Experimentalists have pursued the generation of a single attosecond pulse, which could be used in a new generation of attosecond pump attosecond probe experiments. Even though it was long predicted that the cycle duration of the high harmonic light should be in the order of 100s of attoseconds, it was only in the early 2000s that techniques such as RABBITT[74, 75, 76], FROG-CRAB [77, 78, 79], LAPIN[80] and attosecond streaking [81, 82, 83, 84, 85, 86, 87] were developed for characterizing attosecond pulses. Since then, single attosecond bursts with durations down to about 60as have been reported [9, 88].

Even though attosecond science has in the past 20 years overwhelmingly advanced, the generation of intense isolated attosecond pulses still remains a great technical challenge. This hinders the possibility of performing attosecond-pump attosecond-probe experiments, which could reveal in great detail the attosecond electron dynamics of atoms and molecules [89].

1.4 Attosecond electron dynamics

Attosecond pump attosecond probe experiments are seen as the holy grail of attosecond science. However, the current single XUV/VUV attosecond pulse sources still can not produce radiation with the required intensity to compensate for two important factors that arises in the XUV/VUV region of the spectra: the heavy losses involved in pump-probe setups, and the generally low cross sections for single and multiphoton process in this spectral region. Nevertheless, there are other experimental methods granting access to the attosecond electron dynamics of atoms and molecules, such as high harmonic spectroscopy, attosecond streaking and the attoclock.

The HHG process is in fact a genuine pump-probe experiment, where the ionization initiates the dynamics of the system, which is later probed by the recombining electron. If all the information regarding the strong field processes (i.e., ionization, propagation of the electron in the continuum and recombination) can be disentangled from the observed harmonic light, one can then gain access to the dynamics of the target atom or molecule with attosecond resolution. The time-delay between ionization and recombination can be modified by varying the wavelength of the driving IR pulse. Several experiments have demonstrated the power of high harmonic spectroscopy to

investigate different aspects of the attosecond electron dynamics in atoms and molecules [14]. For example, Itatani and co-workers imaged the ground state orbital of N_2 by measuring the HHG spectrum while rotating the molecule relative to the polarization of the driving laser field, allowing for tomographic-like reconstruction of the orbital [90]. Another well known example is the dynamical minima observed in the high harmonic spectra of CO_2 , which varies with the intensity of the driving laser field and can be mapped onto the hole dynamics of the molecule [91] (see further discussion of this experiment in chapter 9).

Streaking experiments combine an IR field and an isolated attosecond pulse. The main idea of this technique is to first photoionize the target system with an isolated attosecond pulse, and subsequently accelerate the continuum electron with the IR field. By varying the delay between the two pulses, one is then able to measure the so called streaking trace, which maps different times of photoionization to the photoelectron energy. As the acceleration of the electron depends on the phase of the IR pulse instead of its envelope, subfemtosecond information on the dynamics of the target atom or molecule (e.g., time delays in photoemission from different molecular orbitals and the time scales of strong field ionization [92]) can be extracted from the streaking trace.

Another interesting application of the streaking principle is the attoclock. In this case, ionization is via tunneling by a circularly polarized IR field. After liberation from the target, the ionized electron starts to perform circular motion driven by the polarization of the IR pulse. After the pulse is over, the angle at which the the continuum electron reaches the detector can be mapped onto the time at which the electron was liberated, thus giving the potential to look inside the ionization process on the sub laser-cycle time-scale [93, 94, 95, 96].

1.5 Theoretical methods in ionization

The various ionization mechanisms (tunnel, multiphoton or single photon ionization) resulting from the interaction of an IR or VUV/XUV radiation with atoms or molecules are classified according to the intensity and wavelength of the incident radiation [97, 98, 99]. There are different theories and levels of approximations for treating each of the ionization mechanisms listed.

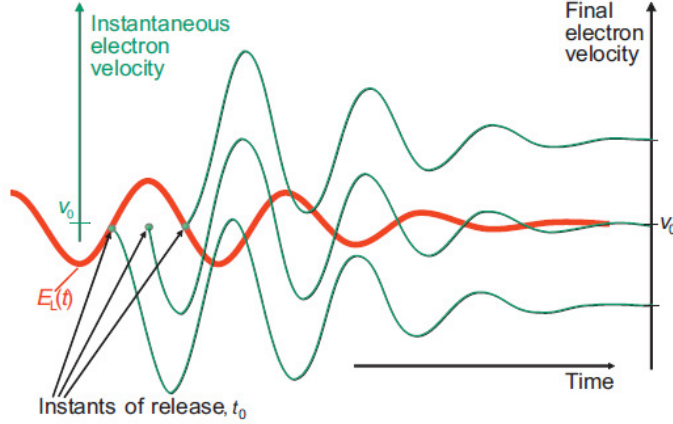


Figure 1.4: Principle of streaking: electrons that are ejected at different initial time, t_0 , obtain different accelerations from the IR field, thus different final velocity. Taken from [14].

In this thesis, we investigate ionization via the single photoionization process



where A_i and A_j^+ are the initial and final state of the target atom or molecule respectively. Single photoionization is the leading mechanism for ionization of atoms and molecules using low intensity XUV sources, such as HHG light, and attenuated synchrotron sources. Note that in the XUV regime, the wavelength of the XUV radiation is still 2 orders of magnitude larger than the typical interatomic distance in molecules, thus the dipole approximation is valid. Moreover, ionization via a low intensity XUV field can be described by time-independent first order perturbation theory. The photoelectron angular and energy resolved distribution is then found by using the Fermi's golden rule[100]

$$I \propto |\langle \Psi_f^{(-)N} | \mathbf{d} \cdot \hat{\epsilon} | \Phi^N \rangle|^2 \quad (1.5)$$

where $\Psi_f^{(-)N}$ and Φ^N are the scattering and neutral bound states respectively.

In contrast to bound state systems that can be solved using well established quantum chemistry methods, low photon-energy photoionization calculations involve the coupling of several target states with a discretized continuum basis set that represents the continuum electron. Inspired by quantum chemistry methods, the description of the continuum electron in

photoionization have for long relied on either Slater basis (for photoionization from atoms), or Gaussian basis (for photoionization from molecules) [101]. However, for intermediate to large distances from the scattering center, Slater and Gaussian basis functions have little resemblance to the oscillatory behavior that characterizes the wavefunction of the discretized continuum. Consequently, a large Gaussian or Slater basis set is necessary, thus increasing the computational demand from such a calculation. Another difficulty in low energy photoionization calculations is the inclusion of correlation in the scattering wavefunction. A popular approach is to write the scattering wavefunction as a single Slater determinant [102] and use Density Function theory (DFT) potentials to simulate the effects of electronic correlation [103, 104] (see chapter 3). Another possibility is to expand the wavefunction of the system in a basis including several configuration state functions (see chapter 3), that tends to completeness, so electronic correlation could be included *ab initio* to the scattering wavefunction [105, 106]. The last approach is particularly important for calculating photoionization leaving the ion in high excited states, a condition where DFT faces many difficulties.

The calculations in this thesis were performed with the UKRmol package, an implementation of the R-Matrix method for treating the collision of electrons with atoms and molecules. The necessary adaptations for calculating photoionization observables from the UKRmol package is a key aspect of this thesis, which is carefully outlined in chapter 5. The UKRmol package was built on the SWEDEN quantum chemistry codes, allowing us to use robust methods such as CI, CASSCF and MCSCF methods for describing electronic correlation. The continuum basis is given in terms of gaussians generated with a non-linear orthogonalization procedure [107].

1.6 Outline of the thesis

From chapters 2 to 5 we present the basic concepts and theoretical background relevant to photoionization of atoms and molecules. In chapter 2 we discuss the principles of electron-scattering theory, presenting the relevant observables such as the electron scattering cross sections, the K-, S- and T-matrices. We also show in this chapter the R-Matrix method for solving the electron scattering problem with a simple spherical potential. In chapter 3 we briefly overview the quantum chemical methods used to solve the bound multielectron problem, with an emphasis on the methods explored in

this thesis (CI, MRCI, MCSCF and static-exchange). In chapter 4 we derive an explicit expression for the photoelectron angular distributions, cross section and asymmetry parameters. In chapter 5, we present the R-Matrix method for electron-scattering with atoms and molecules, and the UKRmol codes. We show in this chapter the basic routines of the UKRmol codes, as well as the recently developed code for adapting the package to calculate photoionization.

From chapter 6 to 9 we benchmark and explore the limits of the new codes for calculating photoionization with the the UKRmol code suite in several aspects. In chapter 6 we perform photoionization calculations from the ground state of N_2 , CO_2 and NO_2 . We present in this chapter orientation averaged results for all molecules, as well as the photoelectron angular distribution for CO_2 and the photoionization dipoles for NO_2 . In chapter 7 we calculate the photoionization of NO_2 from the neutral and first excited state of the molecule for various geometric configurations of the nuclei. These results are important for the evaluation of photoelectron/high harmonic spectroscopy of NO_2 , and to the best of our knowledge these are the first *ab initio* calculation of polyatomic molecules in a geometric grid with electronic correlation included in both neutral and ionic states. In chapter 8 we calculate the photoionization of H_2 and He, and evaluate the effect of a weak external static field in photoionization. As a benchmark we investigate the effect of the field on the autoionizing resonances converging to the first excited state of H_2 and He. These calculations are relevant for experiments where a short XUV pulse ionizes the system in the presence of a mid infrared laser field. In chapter 9 we present the high harmonic spectra of CO_2 . Our results reproduces with great accuracy the experimental results, and show the importance of including inter-channel dynamics during the high harmonic generation process. Additionally in chapter 9, we show how the short emission window of the recombination step in HHG smoothes the photorecombination dipoles. Finally in chapter 10, we present the conclusions and the new opportunities that could be explored in the future.

Chapter 2

Basic Scattering theory

Consider the collision of a stable electron beam with a gas phase atomic or molecular target. The beam is assumed to have a very narrow peaked velocity, so dispersion effects during the propagation can be neglected. The gas density is assumed to be low enough that, upon detection, the scattered electron does not interact with any other atom or molecule. There are two basic types of collisions: elastic and inelastic. In elastic collisions the kinetic energy of the electron is conserved. In inelastic collisions part of the kinetic energy of the incoming electron is converted into internal energy of the target, possibly opening up the channels for electronic excitation, ionization, and, in the case of molecular targets, fragmentation etc.

In this chapter, we will discuss the foundations of non-relativistic time-independent scattering theory. All equations are given in atomic units. In section 1 we present the basic concepts of scattering for the simple case of a structureless target represented by a spherically symmetric potential. The same potential is also used in section 2 for the formulation of the R-Matrix theory. Multichannel scattering is introduced in section 3 in the context of electron scattering, and finally in section 4, we briefly discuss resonant processes in scattering.

2.1 Single channel scattering theory: short range potentials

Consider the wavefunction of an electron (ψ), dictated by the non-relativistic time independent Schrödinger equation

$$\left[-\frac{\nabla^2}{2} + V(\mathbf{r}) \right] \psi(\mathbf{r}) = E\psi(\mathbf{r}), \quad (2.1)$$

where E is the total energy of the system and V is a spherically symmetric potential, which satisfies the following boundary conditions: $V(r) > r^{-2}$ at the origin, and $V(r) < r^{-1}$ for $r \rightarrow \infty$. The latter condition guarantees that $V(r)$ is a *short range potential*, thus, in the asymptotic limit the electron is described by the free Schrödinger equation (see [108] for a rigorous derivation of this statement).

For an incident electron in the $\hat{\mathbf{z}}$ direction scattered at an angle $\hat{\mathbf{k}} = (\theta, \phi)$, ψ can be written at the asymptotic limit as the sum of a plane and a spherical wave

$$\psi(\mathbf{r}) \underset{r \rightarrow \infty}{\approx} e^{ikz} + f(\hat{\mathbf{k}}) \frac{e^{ikr}}{r}, \quad (2.2)$$

where $|k| = \sqrt{2E}$ is the wavenumber of the scattered electron, and $f(\hat{\mathbf{k}})$ is the scattering amplitude, which carries all the information regarding the interaction between the electron and the short range potential.

A particularly useful parameter that can be directly measured in electron scattering experiments is the electron scattering *differential cross section*, i.e., the electron flux over a solid angle in a distance sufficiently far away from the scattering center. At such a distance the effect of the short range potential is negligible, thus the electron can be considered to be asymptotically free. The differential cross section is related to the scattering amplitude by

$$\frac{d\sigma}{d\hat{\mathbf{k}}} = |f(\hat{\mathbf{k}})|^2. \quad (2.3)$$

In atomic units, the differential cross sections has units of Barn (a_0^2) per steradian. If Eq.2.3 is integrated over the solid angle, we obtain the *total cross section* (σ_{tot}).

It is convenient to write ψ in terms of the following *partial wave expansion* (i.e., in an angular momentum basis for the scattering electron) [108]

$$\psi = \sum_l B_l(k) r^{-1} \eta_l(r) P_l(\cos \theta), \quad (2.4)$$

where P_l are Legendre polynomials and $B_l(k)$ are energy dependent coefficients. Substituting Eq.2.4 in Eq.2.1, we obtain the reduced radial Schrödinger equation

$$\left[-\frac{d^2}{dr^2} + \frac{l(l+1)}{r^2} + 2V(r) \right] \eta_l(r) = k^2 \eta_l(r), \quad (2.5)$$

which satisfies the following boundary conditions

$$\eta_l(r) \underset{r \rightarrow 0}{\approx} nr^{l+1}, \quad (2.6)$$

$$\eta_l(r) \underset{r \rightarrow \infty}{\approx} N[s_l(kr) + \tan \delta_l(k)c_l(kr)]. \quad (2.7)$$

$\delta_l(k)$ is the *partial wave phase shift* (defined up to the addition of an arbitrary multiple of π) that carries the information regarding the interaction between the outgoing electron with the short range potential. N is a normalization constant taken to be 1 in Eq.2.7, and $K_l(k) = \tan \delta_l(k)$ is the so called *K-Matrix*. s_l and c_l are solutions of free reduced radial Schrödinger equation given by

$$s_l(kr) = krj_l(kr) \underset{r \rightarrow \infty}{\approx} \sin(kr - l\pi/2) \quad (2.8)$$

$$c_l(kr) = -krn_l(kr) \underset{r \rightarrow \infty}{\approx} \cos(kr - l\pi/2), \quad (2.9)$$

where j_l and n_l are spherical Bessel and Neumann functions respectively.

If, in Eq.2.7, we define $N = -2i \cos \delta_l(k) \exp[i\delta_l(k)]$, we obtain that

$$\eta_l(r) \underset{r \rightarrow \infty}{\approx} e^{-i(kr-l\pi/2)} - S_l(k)e^{i(kr-l\pi/2)}, \quad (2.10)$$

with $S_l(k) = \exp[2i\delta_l(k)]$ being the *S-Matrix*. In the absence of the potential, it is easy to see from Eq.2.14 that $S_l = 1$ and $\psi(\mathbf{r}) = e^{ikz}$. This reflects the nature of the S-Matrix that for $V(r) \neq 0$, transforms the incident free electron e^{ikz} into an incident+scattered state. It is also convenient to define the *T-Matrix* as

$$T_l(k) = \frac{2iK_l(k)}{1 - iK_l(k)} = S_l(k) - 1. \quad (2.11)$$

Expanding e^{ikz} in an angular momentum basis

$$e^{ikz} = \sum_{l=0}^{\infty} (2l+1)j_l(kr)P_l(\cos \theta), \quad (2.12)$$

and comparing the coefficients of e^{-ikr} from Eq.2.2 and Eq.2.4 using Eq.2.12, Eq.2.7, Eq.2.8 and Eq.2.9, we find that

$$B_l(k) = \frac{2l+1}{k} i^l \cos \delta_l(k) e^{i\delta_l(k)}. \quad (2.13)$$

Substituting Eq.2.13 in Eq.2.4, we obtain that the scattering amplitude and the partial wave phase shifts are related by

$$f(\hat{\mathbf{k}}) = \frac{1}{2ik} \sum_{l=0}^{\infty} (2l+1) [\exp[2i\delta_l(k)] - 1] P_l(\cos \theta). \quad (2.14)$$

For short range potentials and low electron energies Eq.2.14 converges quickly, not requiring the inclusion of a large number of angular momentum. Integrating Eq.2.14 over the solid angles, we find that the total cross section for such a system is

$$\sigma_{tot} = \frac{4\pi}{k^2} \sum_{l=0}^{\infty} (2l+1) \sin^2(\delta_l(k)) \quad (2.15)$$

2.2 Single channel scattering theory: the Coulomb potential

Consider the Schrödinger equation of an electron interacting with a Coulomb potential

$$\left(-\frac{\nabla^2}{2} + \frac{Z_1 Z_2}{\mathbf{r}} \right) \psi_c(\mathbf{r}) = E \psi_c(\mathbf{r}), \quad (2.16)$$

where Z_1 is the electronic charge of the electron and Z_2 is the electronic charge of the scattering center.

The physical acceptable solution of Eq.2.16 for an incident electron in the $\hat{\mathbf{z}}$ -direction scattered at an angle $\hat{\mathbf{k}} = (\theta, \phi)$ is given by

$$\psi_c(\mathbf{r}) = e^{-\frac{1}{2}\pi\beta + ikz} \Gamma(1+i\beta) {}_1F_1(-i\beta; 1; ik\zeta), \quad (2.17)$$

where $\beta = Z/2k$, $\zeta = r - z$, Γ is the Gamma function and

$${}_1F_1(a; b; z) = W_1(a; b; z) + W_2(a; b; z) \quad (2.18)$$

where

$$W_1(a; b; z) \underset{|z| \rightarrow \infty}{\approx} \frac{\Gamma(b)}{\Gamma(a)} (-z)^{-a} v(a; a-b+1; -z), \quad -\pi < \arg(-z) < \pi \quad (2.19)$$

and

$$W_2(a; b; z) \underset{|z| \rightarrow \infty}{\approx} \frac{\Gamma(b)}{\Gamma(a)} e^z z^{a-b} v(1-a; b-a; z), \quad -\pi < \arg(z) < \pi \quad (2.20)$$

with

$$v(\alpha; \beta; z) \underset{|z| \rightarrow \infty}{\approx} 1 + \frac{\alpha\beta}{z} + \frac{\alpha(\alpha+1)\beta(\beta+1)}{2!z^2} + \dots \quad (2.21)$$

Substituting the explicit form of ${}_1F_1$ into Eq.2.17 and considering only the zeroth order expansion of v , we obtain that

$$\psi_c(\mathbf{r}) \underset{|z| \rightarrow \infty}{\approx} e^{-\frac{1}{2}\pi\beta + ikz} \Gamma(1+i\beta) \left(\frac{(-ik\zeta)^{i\beta}}{\Gamma(1+i\beta)} + \frac{(ik\zeta)^{-i\beta-1}}{\Gamma(-i\beta)} e^{ik\zeta} \right). \quad (2.22)$$

Using $a^b = e^{b \ln a}$, Eq.2.22 becomes

$$\psi_c(\mathbf{r}) = e^{ikz} \Gamma(1+i\beta) \left(\frac{e^{i\beta \ln k\zeta}}{\Gamma(1+i\beta)} + \frac{e^{-i\beta \ln k\zeta}}{ik\zeta \Gamma(-i\beta)} e^{ik\zeta} \right) \quad (2.23)$$

$$= e^{ikz + i\beta \ln k\zeta} + e^{ikr - i\beta \ln k\zeta} \frac{\Gamma(1+i\beta)}{ik\zeta \Gamma(-i\beta)}. \quad (2.24)$$

Since $\zeta = 2r \sin^2(\theta/2)$ and $\Gamma(1+i\beta)/\Gamma(-i\beta) = i\beta e^{\ln(2\sigma_0)}$, where $\sigma_0 = \arg[\Gamma(1+i\beta)]$, $\psi_c(\mathbf{r})$ can be finally written as

$$\psi_c(\mathbf{r}) \underset{\zeta \rightarrow \infty}{=} e^{ikz + i\beta \ln(k\zeta)} + \frac{f_c(\hat{\mathbf{k}})}{r} e^{ikr - i\beta \ln(2kr)}. \quad (2.25)$$

with the scattering amplitude for the Coulomb potential given by

$$f_c(\hat{\mathbf{k}}) = -\frac{\beta}{2k \sin^2(\theta/2)} e^{2i(\sigma_0 - \beta \ln \sin \frac{\theta}{2})}. \quad (2.26)$$

Eq.2.25 is analogous to Eq.2.2, except for a logarithm phase factor affecting the free plane and spherical waves. Since this phase factor diverges for $r \rightarrow \infty$, even in the asymptotic limit the electron can not be considered as a free particle. Moreover, the total cross section for scattering with a Coulomb potential diverges, since $f_c \rightarrow \infty$ at $\theta = 0$.

In practical electron-molecule scattering problems, the Coulomb potential is often accompanied by a short range potential (V_s). This short range potential accounts for the interaction between the continuum and bound electrons

of the system and satisfy the boundary conditions already detailed in the last section. The Schrödinger equation of this system is given by

$$\left(-\frac{\nabla^2}{2} + V_s(\mathbf{r}) + \frac{Z_1 Z_2}{\mathbf{r}} \right) \psi_s(\mathbf{r}) = E \psi_s(\mathbf{r}). \quad (2.27)$$

Expanding ψ_s in an angular momentum basis

$$\psi_s = \sum_l B_{l,c}(k) r^{-1} \eta_{l,c}(r) P_l(\cos \theta), \quad (2.28)$$

and substituting it in Eq.2.27, we obtain the following reduced radial Schrödinger equation

$$\left(-\frac{d^2}{dr^2} + \frac{l(l+1)}{r^2} + 2V_s(r) + \frac{2Z_1 Z_2}{r} - k^2 \right) \eta_{l,c}(r) = 0, \quad (2.29)$$

where $\eta_{l,c}$ is the radial part of the wavefunction. In analogy to Eq.2.7, the asymptotic solutions of Eq.2.29 can be written as

$$\eta_{l,c}(r) \underset{r \rightarrow \infty}{\approx} [F_l(\beta, kr) + \tan \delta_l(k) G_l(\beta, kr)], \quad (2.30)$$

where $\tan \delta_l(k)$ is the scattering phase due to the short range potential (in the presence of the Coulomb potential), and F_l and G_l are regular and irregular solutions of Eq.2.29 given by

$$\begin{aligned} F_l(\beta, kr) &= C_l(\beta) e^{ikr} (kr)_1^{l+1} F_1(l+1+i\beta; 2l+2; -2ikr) \\ &\underset{r \rightarrow \infty}{\approx} \sin\left(kr - \frac{l\pi}{2} - \beta \ln(2kr) + \sigma_l\right), \end{aligned} \quad (2.31)$$

$$\begin{aligned} G_l(\beta, kr) &= iC_l(\beta) e^{ikr} (kr)^{l+1} [W_1(l+1+i\beta; 2l+2; -2ikr) \\ &\quad - W_2(l+1+i\beta; 2l+2; -2ikr)] \\ &\underset{r \rightarrow \infty}{\approx} \cos\left(kr - \frac{l\pi}{2} - \beta \ln(2kr) + \sigma_l\right) \end{aligned} \quad (2.32)$$

with

$$C_l(\beta) = \frac{2^l e^{-\frac{\pi\beta}{2}} |\Gamma(l+1+i\beta)|}{\Gamma(2l+2)}, \quad (2.33)$$

and $\sigma_l = \arg[\Gamma(l+1+i\beta)]$ being the so called *Coulomb phase*.

Comparing the coefficients of the ingoing waves from Eq.2.28 and Eq.2.25 at the asymptotic limit, we find that

$$B_{l,c} = k^{-1}(2l+1)i^l \cos \delta_l(k) e^{i[\sigma_l + \delta_l(k)]}. \quad (2.34)$$

Substituting Eq.2.34 into Eq.2.28 gives

$$\psi_s(\mathbf{r}) \underset{r \rightarrow \infty}{\approx} \psi_c(\mathbf{r}) + \sum_{l=0}^{\infty} \frac{(2l+1)i^l e^{2i\sigma_l}}{2kr} [e^{2i\delta_l(k)} - 1] H_l^+(\beta, kr) \quad (2.35)$$

with

$$H_l^+(\beta, kr) e^{i\sigma_l} [F_l(\beta, kr) + iG_l(\beta, kr)] \underset{r \rightarrow \infty}{\approx} \frac{1}{i} e^{-ikr + i\pi/2 + \beta \ln 2kr} \quad (2.36)$$

Finally, it is easy to show that Eq.2.34 can be written as

$$\psi_s(\mathbf{r}) \underset{r \rightarrow \infty}{=} e^{ikz + i\beta \ln(k\zeta)} + (f_s(\hat{\mathbf{k}}) + f_c(\hat{\mathbf{k}})) \frac{e^{ikr - i\beta \ln(2kr)}}{r}. \quad (2.37)$$

where

$$f_s(\hat{\mathbf{k}}) = \frac{1}{2ik} \sum_{l=0}^{\infty} (2l+1) e^{2i\sigma_l} (e^{2i\delta_l(k)} - 1) P_l(\cos(\theta)). \quad (2.38)$$

The differential cross section is then given as the interference between the Coulomb and short range potential scattering amplitudes

$$\frac{d\sigma}{d\hat{\mathbf{k}}} = |f_s + f_c|^2 = f_s^2 + f_c^2 + 2\mathcal{R}e(f_s f_c^*). \quad (2.39)$$

2.3 The R-Matrix theory

The R-matrix approach consists in solving the scattering problem by partitioning the configurational space into two or more regions. Different levels of approximation at each of the regions can be applied to determine the wavefunction of the system. Information on the radial part of the inner region wavefunction is then transferred to the other regions via the R-Matrix, which will be derived below in this section. In electron scattering with atoms and molecules for example, the inner most region ($r < r_a$) contains all the electrons of the system. Solutions to this region employ methods borrowed from quantum chemistry (see more details about quantum chemistry in chapter

3). The outer regions ($r > r_a$) is occupied exclusively by the continuum electron, with the effect of the bound electrons given in terms of a multipole expansion. Different methods are then used for propagating the R-Matrix from r_a to r_p , where the R-Matrix is matched to the asymptotic expansion of the system, and the scattering observables can be extracted.

For simplicity, we consider here the same spherical symmetry potential defined in section 2.1. We introduce the \mathbf{D}_l operator as

$$\mathbf{D}_l \eta_{l,i}(r) = \left[-\frac{d^2}{dr^2} + \frac{l(l+1)}{r^2} + 2V(r) - k^2 \right] \eta_{l,i}(r) = 0, \quad (2.40)$$

with $\eta_{l,i}$ being the radial part of the wavefunction of the system. In the inner most region ($r < r_a$) of the configurational space it is easy to show that

$$\int_0^{r_a} (w \mathbf{D}_l v - v \mathbf{D}_l w) dr = \int_0^{r_a} w \frac{d^2 v}{dr^2} dr - \int_0^{r_a} v \frac{d^2 w}{dr^2} dr = \left(w \frac{dv}{dr} - v \frac{dw}{dr} \right)_{r=r_a} \quad (2.41)$$

where w and v are two arbitrary square integrable functions confined to $r < r_a$ that are zero at the origin. Eq.2.41 shows that \mathbf{D}_l is not Hermitian in a finite region in space, unless w and v obey the homogeneous boundary conditions

$$\frac{r_a}{w(r_a)_l} \frac{dw(r_a)_l}{dr} = b_0. \quad (2.42)$$

A possible way to overcome this problem was introduced by Bloch and consists of rewriting Eq.2.40 as [109]

$$(\mathbf{D}_l - \mathcal{L}(r_a, b_0)) \eta_l(r) = -\mathcal{L}(r_a, b_0) \eta_l(r), \quad (2.43)$$

with $\mathcal{L}(r_a, b_0) = \delta(r - r_a) \left(\frac{d}{dr} - \frac{b_0}{r} \right)_{r=r_a}$ being the Bloch operator. Note that $\mathbf{D}_l - \mathcal{L}(r_a, b_0)$ defined over an L^2 basis is always Hermitian, independently of the boundary conditions imposed at $r = r_a$.

Inverting Eq.2.43, we get the formal solution for Eq.2.41

$$\eta_l(r) = -(\mathbf{D}_l - \mathcal{L}(r_a, b_0))^{-1} \mathcal{L}(r_a, b_0) \eta_l(r). \quad (2.44)$$

Introducing a basis $\xi_{j,l}$, which diagonalizes $\mathbf{D}_l - \mathcal{L}(r_a, b_0)$ such that

$$\int_0^{r_a} \xi_{i,l}(r) (\mathbf{D}_l - \mathcal{L}(r_a, b_0)) \xi_{j,l}(r) dr = (E - E_j) \delta_{ij}, \quad (2.45)$$

we can write the inverse of $\mathbf{D}_l - \mathcal{L}(r_a, b_0)$ in the spectral representation as

$$-(\mathbf{D}_l - \mathcal{L}(r_a, b_0))^{-1} = \frac{1}{2} \sum_i \frac{\xi_{i,l}(r)\xi_{i,l}(r')}{E_i - E}. \quad (2.46)$$

Eq.2.43 then becomes

$$\begin{aligned} \eta_l(r_a) &= \frac{1}{2r_a} \sum_i \frac{\xi_{i,l}(r_a)\xi_{i,l}(r_a)}{E - E_i} \left(r_a \frac{d\eta_l(r)}{dr} - \frac{b_0\eta_l(r)}{r} \right)_{r=r_a} \\ &= R_l(E, r_a) \left(r_a \frac{d\eta_l(r)}{dr} - \frac{b_0\eta_l(r)}{r} \right)_{r=r_a}, \end{aligned} \quad (2.47)$$

where $R_l(E, r_a)$ is the so called R-Matrix, and the spectrum of E_i values are referred as the poles of the R-Matrix. Note that the R-Matrix depends only parametrically on the energy of the scattering particle, thus, in order to find the R-Matrix one needs to diagonalize $\mathbf{D}_l - \mathcal{L}(r_a, b_0)$ only once for an L^2 basis capable of representing the η_l over a certain energy range.

Matching Eq.2.47 to the asymptotic boundary conditions of η_l for the case of scattering by a short range potential (see Eq.2.7), we find the following relation between the K and the R-Matrix

$$K_l(E) = \frac{-s_l + R_l(E, r_a) \left(kr_a s'_l(kr_a) - b_0 s_l(kr_a) \right)}{c_l - R_l(E, r_a) \left(kr_a c'_l(kr_a) - b_0 c_l(kr_a) \right)}. \quad (2.48)$$

In case of electron-ion scattering, s_l and c_l in Eq.2.48 are replaced by regular and irregular Coulomb functions (Eq.2.31 and Eq.2.32).

In order to reduce the size of the inner region calculation, so L^2 methods can converge more quickly, it is important to position the R-matrix boundary as close as possible to the scattering center. The R-Matrix radius could then be propagated from r_a to r_p (see [100] for a detailed explanation of several propagation methods), where the R-Matrix is matched to the asymptotic solutions of the system.

2.3.1 Approximate R-Matrix methods

In most of the practical scattering problems, the solutions of the system can only be found numerically. The R-Matrix approach allows us to truncate

the inner region and discretize the continuum eigensolutions, thus, the radial solutions of the Schrödinger equation in the inner region can be written in terms of a L^2 basis. By diagonalizing the inner region in such a basis, one obtains the poles and boundary amplitudes of the inner region solutions, which are then used to build up an approximate R-matrix.

There are several choices of basis for representing the continuum. The homogeneous boundary condition method consists of using an orthonormal basis ($\eta_{l,i}^0$) defined as the eigenfunctions of

$$\left[-\frac{d^2}{dr^2} + \frac{l(l+1)}{r^2} + 2V_0(r) - k_{0i}^2 \right] \eta_{l,i}^0(r) = 0, \text{ for } 0 < r \leq r_a \quad (2.49)$$

and satisfying the boundary conditions

$$\eta_{l,i}^0(0) = 0, \quad (2.50)$$

$$\frac{d\eta_{l,i}^0(r_a)}{dr} = \frac{\eta_{l,i}^0(r_a)}{r_a} b_0. \quad (2.51)$$

The potential V_0 needs to be simple enough so that the solutions of Eq.2.49 can be easily evaluated. On the other hand V_0 should be as close to V as possible, so the main features of the system are reproduced by the $\eta_{l,i}^0$ basis. The radial part of the total wavefunction, for a given l , is then written as

$$\eta_{l,j}^n(r) = \sum_{i=1}^n \eta_{l,i}^0 c_{ij}^n \quad (2.52)$$

where the c_{ij}^n coefficients are found by diagonalizing $\mathbf{D}_l - \mathcal{L}(r_a, b_0)$ in the $\eta_{l,i}^n$ basis, so that

$$\int_0^{r_a} \eta_{l,i}^n(r) (\mathbf{D}_l - \mathcal{L}(r_a, b_0)) \eta_{l,j}^n(r) dr = (E - E_j^n) \delta_{ij}. \quad (2.53)$$

The approximate R-Matrix can then be written as

$$R_l^{n,hbc}(E, r_a) = \frac{1}{2a_0} \sum_{j=1}^n \frac{[\eta_{l,j}^n(r_a)]^2}{E_j^n - E}. \quad (2.54)$$

The convergence of $R_l^{n,hbc}(E, r_a) \rightarrow R_l(E, r_a)$ depends on two factors: (i) on the rapidity of the convergence of $\eta_{l,j}^n(r_a)$ to the actual boundary amplitudes and of E_j^n to the poles of $R_l(E, r_a)$, and (ii) on the rapidity of the

convergence of $R_l^{n,hbc}(E, r_a)$ to $R_l(E, r_a)$ as $n \rightarrow \infty$. The second factor is the most critical, since generally only a limited number of poles are included in $R_l^{n,hbc}(E, r_a)$. In this case, high lying poles that are not included in Eq.2.54 are crucial for a fast convergence of $R_l^n(E)$, thus further corrections to Eq.2.54 and possibly to the wavefunction of the system may become necessary [110, 100].

Another very powerful method to determine the approximate R-Matrix of a system, is to use a robust linear independent basis set

$$\phi_{l,i}(r), i = 1, \dots, n, 0 \leq r \leq r_a, \quad (2.55)$$

which satisfy arbitrary boundary conditions at r_a and approach completeness as $n \rightarrow \infty$. We define then the following linear combination

$$\eta_{l,j}^{n,abc}(r) = \sum_{i=1}^n \phi_{l,i}(r) c_{ij}, i = 1, \dots, n, 0 \leq r \leq r_a, \quad (2.56)$$

where the c_{ij} coefficients are found by diagonalizing $\mathbf{D}_l - \mathcal{L}(r_a, b_0)$ (see Eq.2.45) and the R-Matrix is given by

$$R_l^{n,abc}(E, r_a) = \frac{1}{2a_0} \sum_{i=1}^n \frac{[\eta_{l,i}^{n,abc}(r_a)]^2}{E_i^n - E}. \quad (2.57)$$

As the $\phi_{l,i}$ basis tends to completeness, arbitrary boundary condition methods can generate very precise poles and boundary amplitudes for Eq.2.57. However, since the basis must be always truncated, high lying R-Matrix poles are generally not precisely reproduced by arbitrary condition methods. Note that these high lying poles should still be included in $R_l^{n,abc}$, since they provide a good first approximation of the effects of the actual high lying poles on R_l .

2.4 Multichannel Scattering

So far we have only considered elastic scattering. However, in a more general framework part of the electron kinetic energy can be converted into internal energy of the target opening up the inelastic channels of the process. Let's take for example the collision of an electron with a hydrogen atom. We

assume the three possible outcomes of the collision,

$$e^- + H \rightarrow \begin{cases} e^- + H \text{ (elastic)} \\ e^- + H^* \text{ (excitation)} \\ e^- + e^- + p^+ \text{ (fragmentation)} \end{cases}$$

with the energy order of the final states being $E(H) < E(H^*) < E(e^- + p^+)$. The three different states after the collision are referred to as the *out channels*. The states prior to the collision are referred to as the *in channels*. A given channel is only open if the kinetic energy of the free electron is larger than the difference between the energy of the final and initial states of the molecule. Energetically inaccessible channels are labelled as closed.

The multichannel scattering wavefunctions can be written in terms of a target state expansion

$$\Psi_k(E) = \mathcal{A} \sum_j^f \Phi_j(\mathbf{x}_1, \dots, \mathbf{x}_N) \eta_{jk}(\mathbf{x}_{N+1}) \quad (2.58)$$

where \mathbf{x}_m are the space-spin coordinates of the m^{th} electron, Φ_j are the eigenfunctions of the target Hamiltonian, η_j are the continuum orbitals, that obey the asymptotic conditions of the problem, and \mathcal{A} is an antisymmetrization operator that acts in the spatial and spin coordinates, ensuring that the scattering wavefunction is antisymmetrized. The index j goes over the discrete and continuum target eigenstates. If the rearrangement channels are open, the infinite sum in the target state expansion should implicitly account for the case where one or more target coordinates goes to infinity and the incoming electron becomes bound, such as in electron-detachment of molecules.

In several computer programs the close coupling expansion employed in the evaluation of the scattering wavefunction uses continuum orbitals that are orthogonalized in relation to the target molecular orbitals. In this case, Eq.2.58 misses the contribution to the scattering wavefunction related to a non-zero overlap between scattered electron and the target orbitals. Therefore, it is necessary to redefine the target state expansion as

$$\Psi_k(E) = \mathcal{A} \sum_j^f \Phi_j(\mathbf{x}_1, \dots, \mathbf{x}_N) \eta_{jk}(\mathbf{x}_{N+1}) + \sum_p \chi_p^{(N+1)}(\mathbf{x}_1, \dots, \mathbf{x}_{N+1}), \quad (2.59)$$

where $\chi_p^{(N+1)}$ are L^2 configurations, which account for the case where the incident electron is trapped by some high excited molecular orbitals.

Since it is computationally not possible to include an infinite number of target states in Eq.2.58 or Eq.2.59, usually only the open and weakly closed channels are used in the target state expansion. The truncation of the target state expansion is known as the *close coupling approximation*.

2.4.1 Derivation of the close coupling equations

In this thesis, we are interested in finding the solutions of the multielectronic Hamiltonian

$$\mathbf{H}^{N+1} = - \sum_i^{N+1} \frac{\nabla_i^2}{2} - \sum_i^{N+1} \sum_j^{N_{nuc}} \frac{Z_j}{r_{ij}} + \sum_{i>j}^{N+1} \frac{1}{r_{ij}} \quad (2.60)$$

where $N+1$ is the number of bound and continuum electrons, N_{nuc} is the number of nuclei of the molecule, and $r_{ij} = |\mathbf{r}_i - \mathbf{r}_j|$. The first summation accounts for the kinetic energy of the electrons, the second for the electron-nuclei interaction, and the third for the electron-electron interaction.

We define the channel functions $\tilde{\Phi}_i^\Gamma$, by spin coupling the target states and the continuum electron

$$\tilde{\Phi}_i^\Gamma(\mathbf{x}_1, \dots, \mathbf{x}_N; \sigma_{N+1}) = \sum_{M_{S_i} m_i} (S_i M_{S_i} \frac{1}{2} m_i | S M S) \Phi_i(\mathbf{x}_1, \dots, \mathbf{x}_N) \chi_{\frac{1}{2} m_i}(\sigma_{N+1}), \quad (2.61)$$

where $(\dots | \dots)$ are the Clebsch Gordan coefficients, $\chi_{\frac{1}{2} m_i}(\sigma_{N+1})$ is the spin function of the continuum electron, S, M_S is the total spin and spin component, S_i, M_{S_i} is the spin and spin component of the target states, and Γ are the conserved quantum numbers.

Applying the multielectron Hamiltonian to Eq.2.59 and projecting it on the channel functions we can write

$$\langle r_{N+1}^{-1} \tilde{\Phi}_i^\Gamma(\mathbf{x}_1, \dots, \mathbf{x}_N; \sigma_{N+1}) | \mathbf{H}^{N+1} - E | \Psi_k(E) \rangle' = 0, \quad (2.62)$$

where the prime indicates that the integral is taken over all electron coordinates except the radial coordinate of the $N+1$ -electro.

Decomposing the multielectron Hamiltonian as

$$\mathbf{H}^{N+1} = \mathbf{H}^N - \frac{\nabla_{N+1}^2}{2} - \frac{Z}{r_{N+1}} + \sum_{i=1}^N \frac{1}{r_{iN+1}}, \quad (2.63)$$

we have from Eq.2.62 that

$$\begin{aligned} \left(\nabla^2 + 2\frac{Z-N}{r} + k_i^2 \right) F_{ik}(r) &= 2 \sum_{i'=1}^n V_{ii'}(r) F_{i'k}(r) \\ &+ 2 \sum_{i'=1}^n \int \left[W_{ii'}(r, r') + X_{ii'}(r, r') \right] F_{i'k}(r) dr', \end{aligned} \quad (2.64)$$

where

$$k_i^2 = 2(E - E_i) \quad (2.65)$$

$$\langle r_{N+1}^{-1} \tilde{\Phi}_i^\Gamma(\mathbf{x}_1, \dots, \mathbf{x}_N; \sigma_{N+1}) | \mathbf{H}^N - E | r_{N+1}^{-1} \tilde{\Phi}_i^\Gamma(\mathbf{x}_1, \dots, \mathbf{x}_N; \sigma_{N+1}) \rangle = E_i, \quad (2.66)$$

and $F_{i'k}$ is the radial component of $\eta_{i'k}(r_{N+1})$.

The left hand side of the Eq.2.64 as well as the local potential $V_{ii'}(r)$ arises from the direct term of the close coupling expansion. The local $V_{ii'}(r)$, the non-local exchange $W_{ii'}(r, r')$ and the non-local correlation $X_{ii'}(r, r')$ potentials are given respectively by

$$\begin{aligned} V_{ii'}(r_{N+1}) &= \langle r_{N+1}^{-1} \tilde{\Phi}_i^\Gamma(\mathbf{x}_1, \dots, \mathbf{x}_N; \sigma_{N+1}) | \sum_{k=1}^N \frac{1}{r_{kN+1}} - \\ &\frac{N}{r_{N+1}} | r_{N+1}^{-1} \tilde{\Phi}_{i'}^\Gamma(\mathbf{x}_1, \dots, \mathbf{x}_N; \sigma_{N+1}) \rangle', \end{aligned} \quad (2.67)$$

$$W_{ii'}(r, r') = -N \langle r_{N+1}^{-1} \tilde{\Phi}_i^\Gamma(\mathbf{x}_1, \dots, \mathbf{x}_N; \sigma_{N+1}) | \frac{1}{r_{NN+1}} | r_{N+1}^{-1} \tilde{\Phi}_{i'}^\Gamma(\mathbf{x}_1, \dots, \mathbf{x}_N; \sigma_{N+1}) \rangle'', \quad (2.68)$$

$$X_{ii'}(r_N, r_{N+1}) = - \sum_{i=1}^m U_{ip}(r_N, r_{N+1}) \frac{1}{\epsilon_p - E} U_{i'p}(r_N, r_N), \quad (2.69)$$

$$U_{ip}(r_N) = \langle r_{N+1}^{-1} \tilde{\Phi}_i^\Gamma(\mathbf{x}_1, \dots, \mathbf{x}_N; \sigma_{N+1}) | \mathbf{H}^{N+1} - E | \chi_p^{(N+1)} \rangle. \quad (2.70)$$

where the single prime indicates that the integration is performed over all electronic coordinates except r_{N+1} , and the double prime indicates that the integral is performed over all electronic coordinates, except r_N, r_{N+1}

At the asymptotic limit, the channel function decays quickly. Consequently, since the asymptotic behavior of $X_{ii'}(r, r')$ and $W_{ii'}(r, r')$ for $r \rightarrow \infty, r' \rightarrow \infty$ is dominated by the asymptotic behavior of the target states,

both non local potential vanishes and the close coupling equations simplify to

$$\left(\frac{d^2}{dr^2} - \frac{l_i(l_i + 1)}{r^2} + 2\frac{Z - N}{r} + k_i^2\right)F_{ij}(r) = 2\sum_{i'=1}^n V_{ii'}(r)F_{ij}(r). \quad (2.71)$$

An asymptotic form for the $V_{ii'}(r)$ is derived in Appendix A.

2.5 Resonances

Resonances are quasibound states embedded in the continuum. Mathematically, isolated resonances manifests as a sudden π phase jump of the phase shift [111], which due to Eq.2.15 results in a sudden change of the total scattering cross section. Close to the resonance, the phase shift can be decomposed in a resonant and a non resonant part

$$\delta = \delta_{res} + \delta_{bg}. \quad (2.72)$$

with δ_{bg} being nearly constant in the resonant region. The central position (E_r) and width (Γ) of a resonance is related to the phase shift by the Breit-Wigner formula [112]

$$\delta = -\arctan \frac{\Gamma}{2(E - E_r)} + \delta_{bg}. \quad (2.73)$$

The abruptness of the π phase jump in δ_{res} is determined by the resonance width Γ .

In the case of scattering with a short range potential, by substituting Eq.2.73 in Eq.2.15, we find that close to a resonance the total cross section can be written as

$$\sigma_{tot} = \frac{4\pi}{k^2}(2l + 1)\frac{(\varepsilon + q)^2}{1 + \varepsilon^2}\sin^2(\delta_{bg}(k)), \quad (2.74)$$

with $q = -\cot(\delta_{bg}(k))$, and $\varepsilon = 2(E - E_r)/\Gamma$. The shape of the resonance is dictated by the non-resonant part of the phase shift, e.g, in the case of s-wave scattering ($l=0$) if $\delta_{bg} = 0$ the resonance is observed in the scattering cross section as a peak, on the other hand, if $\delta_{bg} = \pi/2$ the resonance is observed in the cross section as a valley (see Fig.2.1).

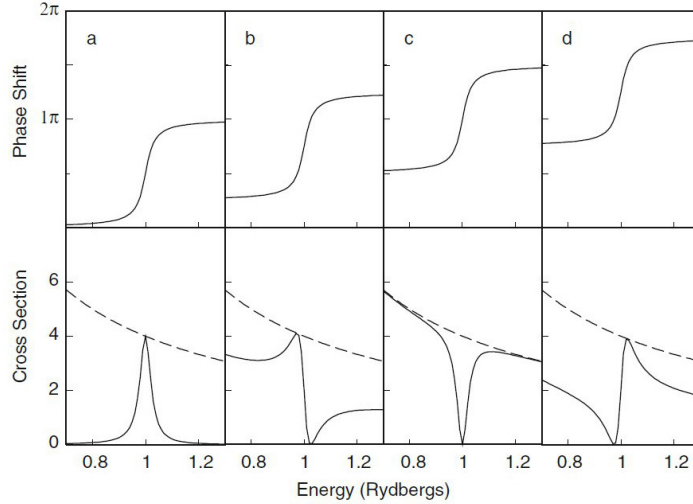


Figure 2.1: Total phase shift (top) and cross sections (bottom) for s-wave scattering, $\Gamma = 0.05$ and $k_r^2 = 2E_r = 1$. Four different values of δ_{bg} are taken: 0 (a), $\pi/4$ (b), $\pi/2$ (c) and $3\pi/4$ (d). Taken from [100]

In a more intuitive physical picture, resonances can be interpreted as temporary trapping of the continuum electron in a quasi-bound state of the system. In collisions of electrons with atoms and frozen nuclei molecules there are two types of resonances: shape-resonances and core-excited resonances.

Shape resonances, which in general have a large energy width, arises due to the trapping of the continuum electron in a potential well created by two competing factors: the centrifugal force from the angular momentum of the continuum electron, and the attractive polarization potential of the target atom or molecule [113]. In this case it is clearly not possible to have shape resonances in the $l = 0$ partial wave.

Core excited resonances arise from the simultaneous excitation of the target and the trapping of the incoming electron, forming a Rydberg-like state. The target is then left in an excited state, referred as *parent excited state*. There are then two possibilities: the Rydberg-like state decay to the parent excited state, if this state is energetically open, forming a core-excited shape resonance; or the Rydberg-like state decay to a molecular state below the parent excited state, forming a Feshbach resonance [106].

Chapter 3

Principles of quantum chemistry

It is evident from the close coupling expansion presented in the previous chapter, that in multichannel scattering it is necessary to have a reliable description of the bound states of the target atom or molecule. Therefore we will for the moment forget about the scattering process, and dedicate this chapter for presenting some of the numerical methods used to solve the bound state problem.

Electrons are much lighter and faster than the atomic nuclei, thus, it is reasonable to assume that the electronic cloud instantaneously rearranges after geometrical variations of the nuclei. Therefore the so called *Born Oppenheimer approximation* can be used to separate the electronic and nuclear part of the wavefunction of the molecular Hamiltonian. The *electronic Hamiltonian* is then given by

$$\mathbf{H}^N = - \sum_i^N \frac{\nabla_i^2}{2} - \sum_i^N \sum_j^{N_{nuc}} \frac{Z_j}{r_{ij}} + \sum_{i>j}^N \frac{1}{r_{ij}} \quad (3.1)$$

where N is the number of bound and continuum electrons, N_{nuc} is the number of atomic nuclei of the molecule, and $r_{ij} = |\mathbf{r}_i - \mathbf{r}_j|$. The first summation accounts for the kinetic energy of the electrons, the second corresponds to the electron-nuclei interaction, and the third accounts for the electron-electron interaction. When two or more electronic states belonging to the same point symmetry group are energetically close to each other, the Born Oppenheimer approximation fails, as different electronic and nuclear eigenfunctions of the

molecule becomes non-adiabatically coupled. In Chapter 7 we explore the spectroscopy of NO_2 in situations where the non-adiabatic couplings are non negligible.

Finding the wavefunction of the electronic Hamiltonian for atoms or molecules with more than one electron is a formidable task for basically two reasons: (i) the high dimensionality of the system, and (ii) the singularities in the Hamiltonian that arises from the electron-electron interaction term. In this chapter, we present the numerical methods used in this thesis for determining the electronic wavefunction of atoms and molecules. In section 3.1 we briefly discuss some general concepts for the calculation of the electronic structure of atoms and molecules. In section 3.2, we present the Hartree Fock method for solving the bound state problem, which neglects electronic correlation, but can still be a good first approximation to the problem. In section 3.3 and 3.4 we present the configuration interaction (CI), the multireference configuration interaction (MRCI) and the multiconfigurational self consistent field (MCSCF) methods which can in principle solve the bound state problem with a high degree of accuracy.

3.1 Basic concepts in electronic structure calculations

We express the electronic eigenfunctions of \mathbf{H}^N as

$$\Psi(\mathbf{x}_1, \dots, \mathbf{x}_N) = \sum_i c_i \Phi(\mathbf{x}_1, \dots, \mathbf{x}_N), \quad (3.2)$$

with \mathbf{x} being the spin spatial electronic coordinate. The Φ basis is factorized in terms of the orthonormalized spin-orbitals (ϕ_z) of the atom or molecule

$$\Phi(\mathbf{x}_1, \dots, \mathbf{x}_N) = (N!)^{-1/2} \left| \phi_a(\mathbf{x}_1) \phi_b(\mathbf{x}_2) \dots \phi_z(\mathbf{x}_N) \right|, \quad (3.3)$$

where we have introduced the Slater determinant notation [102], which ensure that Φ , and consequently Ψ , are always antisymmetric. As the spin-orbit basis tends to completeness, Eq.3.2 approaches the exact electronic eigenfunctions of the atom or molecule.

We treat the electron-electron repulsion in an averaged way, i.e., the j^{th} electron moves in a static field produced by the other N-1 electrons and

the nuclei. Therefore the eigenfunction of \mathbf{H}^N can be separated into N independent *Hartree Fock* equations for the spin-orbitals [101]

$$f_k \phi_k(\mathbf{x}_k) = \left[h_k + \sum_u [J_u(\mathbf{x}_k) - K_u(\mathbf{x}_k)] \right] \phi_k(\mathbf{x}_k) = \epsilon_k \phi_k(\mathbf{x}_k). \quad (3.4)$$

with ϵ being the spin-orbital energies, f_k the so called Fock operator and

$$h_k = -\frac{\nabla_k^2}{2} - \sum_j^{N_{nuc}} \frac{Z_j}{r_{kj}}. \quad (3.5)$$

The summation in Eq.3.4 goes over all the occupied orbitals, and

$$J_u(\mathbf{x}_k) \phi_k(\mathbf{x}_k) = \left[\int \phi_u^*(\mathbf{x}_p) r_{pk}^{-1} \phi_u(\mathbf{x}_p) d\mathbf{x}_p \right] \phi_k(\mathbf{x}_k), \quad (3.6)$$

$$K_u(\mathbf{x}_k) \phi_k(\mathbf{x}_k) = \left[\int \phi_u^*(\mathbf{x}_p) r_{pk}^{-1} \phi_k(\mathbf{x}_p) d\mathbf{x}_p \right] \phi_u(\mathbf{x}_k), \quad (3.7)$$

are the Coulomb and exchange operators respectively. Note that in order to compute Eq.3.4, due to the Coulomb and exchange operator, we need to know beforehand the explicit expression for all other spin-orbitals. For this reason, we must start with a trial set of spin-orbitals and construct the Fock operator. After diagonalizing the Fock operator we obtain a new set of spin-orbitals, which are used once again to construct the Fock operator. The iterations are performed until the variational wavefunction reaches, within a convergence criterion, a minimum energy. This iterative process is known as the *self consistent field* approach. If the minimum is global, the variational principle states that the wavefunction obtained should be the best solution for the basis set used [102].

3.1.1 Spin-orbital basis set

Ideally, one would use a complete basis set for representing the spin-orbitals exactly. As this is of course computationally not feasible, it is always necessary to truncate the size of the basis set. There are three important factors that should be taken into account for choosing a basis set: (i) the basis should be small, so the number of integrals to be evaluated can be reduced, (ii) the basis functions should reproduce reasonably well the main features of

the spin-orbitals, and (iii) the mathematical expression of the basis function should be simple enough so that the 1- and 2-electron integrals can be easily evaluated.

For a basis, $\theta_k(\mathbf{r})$, consisting of M elements it is possible to compute the following M spatial wavefunctions

$$\psi_a = \sum_k^M c_{ak} \theta_k(\mathbf{r}). \quad (3.8)$$

Slater type functions are the most common choice for atomic systems, since this basis well reproduces the cusp at the atomic nuclei that characterizes the nuclei-electron repulsion. In this thesis, since we are mostly interested in molecular systems, we use Gaussian-type orbital basis given by

$$\theta_{ijk}(\mathbf{r}_m - \mathbf{r}_c) = C(x_m - x_c)^i (y_m - y_c)^j (z_m - z_c)^k e^{-\alpha|\mathbf{r}_m - \mathbf{r}_c|^2} \quad (3.9)$$

where α is a positive exponent and C is a normalization coefficient. (x_c, y_c, z_c) and (x_m, y_m, z_m) are the cartesian coordinates of the centre of the Gaussian and the m^{th} electron respectively. The type of the orbitals generated by the gaussian basis set is dictated by the sum of the positive integers i, j, k . S-type orbitals have $i = j = k = 0$, p-type orbitals have $i + j + k = 1$, d-type orbitals have $i + j + k = 2$, etc. The power of the Gaussian type orbitals for molecular system comes from the *Gaussian product Theorem*, which states that the product of two Gaussians centered at different atoms can be decomposed in to a single sum of Gaussians centered at a point in-between the atoms [114]. It is also usual to have a set of contracted Gaussians to better represent the basis set close to the atomic nuclei, where the Gaussian basis functions have a bell shape instead of the expected cusp [101]. A list of atomic Gaussian basis set optimized for representing different atomic and molecular properties can be found in [115].

3.1.2 The Roothaan equations

Applying the Fock operator to Eq.3.8 we obtain for the spatial wavefunction ψ_a

$$f_k \sum_{j=1}^M c_{ja} \theta_j(\mathbf{r}_k) = \epsilon_a \sum_{j=1}^M c_{ja} \theta_j(\mathbf{r}_k). \quad (3.10)$$

Multiplying both sides of the equation above by $\theta_i^*(\mathbf{r}_k)$ and integrating over \mathbf{r}_k we obtain the *Roothaan equation*

$$\sum_{j=1}^M c_{ja} \int \theta_i^*(\mathbf{r}_k) f_k \theta_j(\mathbf{r}_k) d\mathbf{r}_k = \epsilon_i \sum_{j=1}^M c_{ja} \int \theta_i^*(\mathbf{r}_k) \theta_j(\mathbf{r}_k) d\mathbf{r}_k. \quad (3.11)$$

Introducing the overlap matrix, $S_{ij} = \int \theta_i^*(\mathbf{r}_k) \theta_j(\mathbf{r}_k) d\mathbf{r}_k$, and the Fock matrix, $F_{ij} = \int \theta_i^*(\mathbf{r}_k) f_k \theta_j(\mathbf{r}_k) d\mathbf{r}_k$, Eq.3.11 becomes

$$\sum_{j=1}^M F_{ij} c_{ja} = \epsilon_a \sum_{j=1}^M S_{ij} c_{ja}. \quad (3.12)$$

We can of course generalize Eq.3.12 to all the possible M spatial wavefunction that can be constructed from the basis set θ . In a matrix form, the set of equations resulting from such a generalization is written as

$$\mathbf{F}\mathbf{c} = \mathbf{S}\mathbf{c}\epsilon. \quad (3.13)$$

The computation of the \mathbf{c} coefficients require the prior knowledge of the Fock matrix. Consequently, it is necessary to adopt a self consistent procedure to solve the Roothaan equation, as discussed in section 3.1.

The elements of the Fock matrix are given by

$$\begin{aligned} F_{ij} = h_{ij} + 2 \sum_{ulm} c_{lu}^* c \int \theta_i^*(\mathbf{r}_1) \theta_l^*(\mathbf{r}_2) \frac{1}{r_{12}} \theta_m(\mathbf{r}_2) \theta_j(\mathbf{r}_1) d\mathbf{r}_1 d\mathbf{r}_2 \\ - \sum_{ulm} c_{lu}^* c_{mu} \int \theta_i^*(\mathbf{r}_1) \theta_l^*(\mathbf{r}_2) \frac{1}{r_{12}} \theta_j(\mathbf{r}_2) \theta_m^*(\mathbf{r}_1) d\mathbf{r}_1 d\mathbf{r}_2. \end{aligned} \quad (3.14)$$

In the equation above $h_{ij} = \int \theta_i(\mathbf{r}_1) h_1 \theta_j^*(\mathbf{r}_1) d\mathbf{r}_1$ are known as one-electron integrals, since their evaluation requires an integration only over the r_1 coordinate. The other two terms in Eq.3.14 depend on the integration over the r_1 and r_2 coordinates, thus they are referred to as 2-electron integrals.

Introducing the notation

$$(ab|cd) = \int \theta_a^*(\mathbf{r}_1) \theta_b^*(\mathbf{r}_1) \frac{1}{r_{12}} \theta_c(\mathbf{r}_2) \theta_d(\mathbf{r}_2) d\mathbf{r}_1 d\mathbf{r}_2, \quad (3.15)$$

Eq.3.14 becomes

$$F_{ij} = h_{ij} + \sum_{ulm} P_{lm} [(ij|lm) - \frac{1}{2}(im|lj)], \quad (3.16)$$

where we have defined the density matrix as

$$P_{lm} = 2 \sum_{ulm} c_{lu}^* c_{mu}. \quad (3.17)$$

During the SCF procedure, the 1- and 2-electron integrals must be computed only once, as they are not modified at each iteration of a self consistent field procedure. On the other hand, the density matrix, which depends on c_{lu} and c_{mu} , must be evaluated at each iteration step. The main bottleneck of evaluating the Roothaan equations is the huge number of 2-electrons integrals that must be calculated, which scales as M^4 . Group theory can help in alleviating the number of integrals that must be computed, since many of them are identically zero [116].

3.1.3 Configuration state functions

Solving the Roothaan equations, we obtain M spatial wavefunctions, thus a total of $2M$ spinorbitals. By distributing N electron among the $2M$ spinorbitals one creates a list of Slater determinants, which scales quickly with N and M . Configuration state functions (CSF) are symmetry adapted linear combination of Slater determinants, built in such a way that the quantum numbers of the electronic wavefunction are conserved. The construction of the CSFs relies heavily on group theory, in order to decrease the computational costs of the calculation [116].

3.2 Hartree-Fock method

The Hartree-Fock method consists in representing the electronic wavefunction of an atomic or molecular system with a single Slater determinant. The mean field approximation is implied, in the sense that the electronic repulsion term in the electronic Hamiltonian is considered only in an average way, thus, electronic correlation for electrons with different spin is neglected [102].

Even though restrictive, the Hartree-Fock method has two important advantages:

- Compared to the methods that will be presented in the following sections, the Hartree-Fock method is computationally cheap.

- The mean field approximation allow us to simplify the n -electronic Hamiltonian into an n -independent particle model.

Complications arise for systems with an unpaired electron (open shell). In this case, the HF approach does not take into consideration the full exchange term, resulting in an overestimation of the electronic energy [101]. A way to improve the HF calculation in this case, is to lift the condition that a molecular orbital is described by the same spatial orbital for different values of spin, which is the so called unrestricted Hartree-Fock approach (UHF). The UHF approach leads to orbital energies lower than the usual HF, but also yields in optimized wavefunctions that are not eigenvalues of S^2 , requiring then the use of complicated projection methods to compensate for this inaccuracy [102].

Another critical point of the HF approximation, is that it clearly fails in situations where several electronic states, thus several Slater determinants, are energetically close together such as close to the dissociation limit, or for highly excited states. Under these conditions, the use of a single Slater determinant for describing the wavefunction is a too strong constraint and more robust methods are necessary for correctly describing electronic correlation.

3.3 Configuration interaction

Due to the non-separability of the Coulomb interaction in the electronic Hamiltonian, a more accurate representation of the wavefunction of an atomic or molecular system requires the use of not only a single Slater determinant, but a linear combination of them. We introduce then the following expansion for representing the wavefunction of an electronic state ψ_s

$$\psi_s = \Phi_0 + \sum_j \tilde{C}_{j,s} \Phi_j + \sum_{jk} \tilde{C}_{jk,s} \Phi_{jk,s} + \dots, \quad (3.18)$$

with Φ_0 being the Hartree Fock determinant and the subsequent determinants being built by promoting electrons from occupied spinorbitals in Φ_0 to highly energetic unoccupied spinorbitals. The first summation accounts for the excitation from a single electron from Φ_0 , the second for the excitation of two electrons, etc. For conciseness, we do not show the dependency of the Configuration state functions (CSFs) on the $N+1$ spin spatial coordinates. The spin-orbitals are usually obtained from a previous HF calculation and

held fixed in a CI procedure. If all possible excitations, within a given spin-orbital basis, are used in the CI expansion, the calculation is called a *full CI*. To simplify the following calculations, we write Eq.3.18 simply as

$$\psi_s = \sum_L C_{L,s} \Phi_{L,s}. \quad (3.19)$$

To determine the $C_{L,s}$ coefficients it is necessary to solve, through a variational procedure, the following set of equations

$$\sum_{J=1}^L H_{IJ} C_{Js} = E_s \sum_{J=1}^L S_{IJ} C_{Js}, \quad (3.20)$$

where $S_{IJ} = \int \Phi_I^* \Phi_J^* d\mathbf{x}_1 \dots d\mathbf{x}_N$ and $H_{IJ} = \int \Phi_I^* H \Phi_J^* d\mathbf{x}_1 \dots d\mathbf{x}_N$. Eq.3.20 can be written in the following matrix form, where all electronic states ψ_s are solved simultaneously

$$\mathbf{HC} = E\mathbf{SC}. \quad (3.21)$$

The inclusion of several CSFs in the CI expansion makes the calculation more stable when the energy of different electronic configurations of an atom or molecule are close together, a situation where the Hartree-Fock approach struggles.

The bottleneck of the CI method is the diagonalization of the Hamiltonian matrix, which scales to the cube of the number of CSFs included. Even with the help of group symmetry, the size of the Hamiltonian matrix still quickly becomes prohibitively high for large systems, making a full CI calculation very demanding. Thus, it is customary to truncate the number of excitations allowed in the CI expansion generating what is called CI with single excitation (CIS), single and double excitations (CISD) and so on.

3.4 Multiconfigurational and multireference methods

In contrast to HF, which optimizes only the basis functions, and CI calculations, which optimizes exclusively the CSF coefficients, the multiconfigurational self consistent field (MCSCF) approach relies on the optimization of both simultaneously. MCSCF is particularly powerful in situations where the molecular orbitals from HF calculations are of poor quality, such as close

to the dissociation limit of molecules, at conical intersections, and avoided crossings, or for calculations involving highly excited molecular states. Complete active space self consistent field (CASSCF) is a powerful implementation of MCSCF, in which the orbitals are divided into three sets: an *inactive* set consisting of the low energy doubly occupied spin-orbitals, a *virtual* set consisting of the high energetic orbitals that are never occupied by any determinant, and an *active* set, which are the orbitals energetically in between the inactive and the virtual sets. The CSFs are then constructed by distributing the active electrons among the active orbitals.

Multireference configuration interaction (MRCI) is very similar to CI calculations, the difference being that the CSFs are not only generated from a single reference ground state electronic configuration, but also from a certain number of other determinants. The nomenclature of MRCI calculations follows the one already outlined for CI, i.e., MRCIS for single excitations from the reference CSFs, MRCISD for single and double excitations from the reference CSFs, so on and so forth.

Even though MRCI and MCSCF calculations are capable of generating high quality representation of the ground and excited state wavefunction of atomic and molecular systems, both these methods are computationally very demanding. In MCSCF calculations with a large number of electron one must carefully choose the active space, or even use restricted schemes such as the RASSCF (restricted active space self consistent field (SCF), see further details in [101]) for reducing the dimension of the Hamiltonian of the system. In MRCI dealing with a large number of electrons, one must carefully choose the reference determinant and the degrees of excitations allowed, in order to reduce the computational costs of the calculations.

Chapter 4

Photoionization of molecules

The recent advances in synchrotron sources, and the flexibility afforded by table top femtosecond lasers in producing XUV pulses via high harmonic generation (HHG), have established the photoionization process as one of the most widely used and powerful tools for studying structural and spectral properties of molecules [117]. In photoionization, the interaction of electromagnetic radiation with a given target molecule results in the ejection of one or more photoelectrons. As in this thesis we investigate only photoionization initiated by a low intensity XUV/VUV radiation, we restrict our discussion to the case where a single photoelectron is ejected from the target system.

In the early stages of molecular photoionization experiments it was neither possible to predict nor to enforce the orientation of molecules. Experimentalists were then restricted to investigate structural and spectral properties of the system only by orientationally averaged photoelectron angular distributions (PAD) [118, 119, 120, 121]. Recently, the substantial improvement of molecular alignment and orientation techniques [122] allowed experimentalists to extend the range of applications of PAD: to image the molecular geometry [123, 124, 125] and molecular orbitals [126]; as a probe of molecular chirality [127] and rotational wavepackets [128], etc (see [117] for an extensive list of applications).

As will be shown below in this chapter, the PAD can be expanded in terms of spherical harmonics

$$I_{ij}(\mathbf{k}) \propto \sum_{LM} A_{LM} Y_{LM}(\hat{\mathbf{k}}), \quad (4.1)$$

where \mathbf{k} is the photoelectron momentum and the indices in I_{ij} refer to the

photoionization of a neutral molecule initially in the i state, leaving the residual cation in a j state. A_{LM} are coefficients that depend on the photoionization process and the molecular properties [100]. Generally, Eq.4.1 converges very fast and only a small number of L and M are necessary to describe the PAD [117]. Fully determining the A_{LM} coefficients completely characterizes the photoionization process. In the so called complete experiments, the A_{LM} coefficients are measured by photoionizing an oriented molecule with different schemes of laser polarization [129]. So far, it has only been possible to perform complete experiments for some simple molecules [130, 131], due to the limitations of the molecular orientation techniques. Eq.4.1 is also important in the interpretation of calculations and experiments, since sensitive molecular properties can be probed by analyzing the interference between different terms in Eq.4.1 [132, 133].

In the following sections we discuss the theoretical and experimental aspects of PAD: in section 1 we derive an explicit expression for Eq.4.1 and define the relevant observables; in section 2 we briefly present the experimental aspects of a PAD with particular attention to the alignment and orientation techniques used to at least partially retrieve the PAD in the molecular frame.

4.1 Differential cross sections and asymmetry parameters

Consider the ejection of an electron with momentum \mathbf{k}_f after the interaction of a polarized XUV light with a neutral molecule in the $\Phi_i^{(N+1)}$ state. There are two relevant frames of reference in this process: the laboratory (LF) and the molecular (MF) frames. To connect the molecular frame to the lab frame, we introduce the Euler angles α, β, γ and the associated Wigner rotation matrices (see, for example [134]), $\mathbf{D}^l(\alpha, \beta, \gamma)$, which connects both frames of reference. In the laboratory frame the z axis is usually defined as the polarization direction for linearly polarized light, or the direction of propagation for circularly and elliptically polarized light. If not stated to the contrary, primed (unprimed) variables indicate laboratory (molecular) frame.

We will start the derivations in the molecular frame. Using Fermi's golden rule and normalizing in relation to the photon flux, the PAD in the molecular

frame is given by

$$\frac{d\sigma_{fi}}{d\mathbf{k}_f} = 4\alpha\omega(\pi a_0)^2 |\mathbf{d}_{fi}|^2 \quad (4.2)$$

where α is the fine structure constant, ω is the photon energy, a_0 the Bohr radius, and \mathbf{d}_{fi} is the dipole for a transition from the bound initial state ($\Phi_i^{(N+1)}$) to the $1-e^-$ continuum wavefunction ($\Psi_f^{(-)(N+1)}$)

$$\mathbf{d}_{fi} = \langle \Phi_i^{(N+1)} | \mathbf{d}_\mu | \Psi_f^{(-)(N+1)} \rangle. \quad (4.3)$$

In Eq.4.3 \mathbf{d}_μ represents the dipole operator in the length gauge, which in a spherical harmonics basis is written as

$$\mathbf{d}_\mu = \left(\frac{4\pi}{3} \right)^{1/2} \sum_{n=1}^{N+1} \sum_{m_\gamma} r_n D_{\mu m_\gamma}^{1*}(\alpha, \beta, \gamma) Y_{1m_\gamma}(\hat{\mathbf{r}}_n), \quad (4.4)$$

with μ indicating if the light is linearly ($\mu = 0$), right circularly ($\mu = -1$) or left circularly ($\mu = 1$) polarized, and α, β, γ define the orientation of the molecule in the lab frame.

If the initial state spin is unpolarized and the final state spins are not measured, one must average the PAD over the initial and sum over the final spin components

$$\left(\frac{d\sigma_{fi}}{d\mathbf{k}_f} \right)_{\text{spin avg.}} = \frac{4\alpha\omega(\pi a_0)^2}{2S+1} \sum_{M_S M_{S_f} m_f} |\mathbf{d}_{fi}|^2. \quad (4.5)$$

Similarly, if the molecule belongs to a degenerate point group, it may be necessary to average over the initial state degeneracy and sum over the final state degeneracy.

We will now concentrate on finding an explicit expression for the scattering state, which in the asymptotic limit can be written as

$$\Psi_f^{(-)(N+1)}(\hat{\mathbf{k}}) \underset{r \rightarrow \infty}{\approx} \Psi_f^{\text{inc}}(\hat{\mathbf{k}}) + \Psi_f^{\text{ing}}(\hat{\mathbf{k}}) \quad (4.6)$$

with Ψ_f^{inc} being a Coulomb-modified plane wave incident in direction $\hat{\mathbf{k}}$, and Ψ_f^{ing} satisfies ingoing wave boundary conditions at $r \rightarrow \infty$ [135].

At the asymptotic limit, exchange can be neglected and Ψ^{inc} can be written as

$$\Psi_f^{\text{inc}} = \left[\frac{k_f}{(2\pi)^3} \right]^{1/2} \Phi_f^{(N)}(\mathbf{x}_1, \dots, \mathbf{x}_N) \chi_{\frac{1}{2}m_f}(\sigma_{N+1}) \psi_f^-(\mathbf{r}_{N+1}), \quad (4.7)$$

where $\Phi_f^{(N)}$ are target states, $\chi_{\frac{1}{2}m_f}$ is the spin function of the scattered electron, and ψ_f^- is the Coulomb wavefunction of the scattered electron in the f^{th} channel. In a partial wave basis ψ_f^- becomes

$$\psi_f^- = \sum_{l_f} (2l_f + 1) i^{l_f} \frac{e^{-i\sigma_{l_f}}}{k_f r} F_{l_f}(k_f r) P_{l_f}(\cos \theta). \quad (4.8)$$

where the normalization constant, $e^{-i\sigma_{l_f}}$, allows us to write the asymptotic radial solutions, F_{l_f} , in terms of ingoing waves.

Using the spherical harmonics addition theorem

$$P_{l_f}[\cos(\theta = \Omega_{N+1} - \Omega_k)] = \frac{4\pi}{2l_f + 1} \sum_{m_{l_f}} Y_{l_f m_{l_f}}(\Omega_{N+1}) Y_{l_f m_{l_f}}^*(\Omega_k), \quad (4.9)$$

we have that

$$\begin{aligned} \Psi_f^{inc} &= \sum_{l_f m_{l_f}} i^{l_f} \Phi_f^{(N)}(\mathbf{x}_1, \dots, \mathbf{x}_N) \chi_{\frac{1}{2}m_f}(\sigma_{N+1}) e^{-i\sigma_{l_f}} \\ &\quad \times Y_{l_f m_{l_f}}^*(\Omega_k) Y_{l_f m_{l_f}}(\Omega_{N+1}) r_{N+1}^{-1} \eta_f^0(k_f r_{N+1}), \end{aligned} \quad (4.10)$$

with

$$\eta_f^0(k_f r) = \frac{i}{(2\pi k_f)^{1/2}} F_{l_f}(k_f r) \underset{r \rightarrow \infty}{\approx} \frac{i}{(2\pi k_f)^{1/2}} \left[e^{-i\theta_f(r)} - e^{i\theta_f(r)} \right], \quad (4.11)$$

where $\theta_f(r) = k_f r - \frac{l_f}{2}\pi - \beta_f \ln 2k_f r + \sigma_{l_f}$, with $\beta_f = -(Z - N)/k_f$ and $\sigma_{l_f} = \arg \Gamma(l_f + 1 + i\beta_f)$. Spin coupling the target states and continuum electron while enforcing total spin (S) and spin component (M_S) yields

$$\tilde{\Phi}_f^{SM_S}(\mathbf{r}_1, \dots, \mathbf{r}_N; \sigma_{N+1}) = \sum_{M_{S_f} m_f} (S_f M_{S_f} \frac{1}{2} m_f | S M_S) \Phi_f^{(N)}(\mathbf{r}_1, \dots, \mathbf{r}_N) \chi_{\frac{1}{2}m_f}(\sigma_{N+1}) \quad (4.12)$$

where $(S_j M_{S_j} \frac{1}{2} m_j | S M_S)$ are the Clebsch Gordan coefficients. Substituting Eq.4.12 in Eq.4.10, we finally find that the wavefunction is given by (for a scattered electron with spin component m_f , a target states with spin S_f and spin component M_{S_f} , and total spin S, M_S)

$$\begin{aligned} \Psi_f^{inc} &= \sum_{S_{l_f} m_{l_f}} i^{l_f} \tilde{\Phi}_f^{SM_S}(\mathbf{x}_1, \dots, \mathbf{x}_N; \sigma_{N+1}) (S_f M_{S_f} \frac{1}{2} m_f | S M_S) e^{-i\sigma_{l_f}} \\ &\quad \times Y_{l_f m_{l_f}}^*(\Omega_k) Y_{l_f m_{l_f}}(\Omega_{N+1}) r_{N+1}^{-1} \eta_f^0(r_{N+1}). \end{aligned} \quad (4.13)$$

Substituting Eq.4.13 in Eq.4.6 and including the contribution from all possible in-channels from Ψ_f^{ing} , we have that

$$\begin{aligned} \Psi_f^{(-)(N+1)} &= \sum_{Sl_fm_l_f} \sum_{jl_jm_l_j} i^{l_f} \tilde{\Phi}_f^{SM_S}(\mathbf{x}_1, \dots, \mathbf{x}_N; \sigma_{N+1}) (S_f M_{S_f} \frac{1}{2} m_f | SM_S) e^{-i\sigma_{l_f}} \\ &\times Y_{l_fm_l_f}^*(\Omega_k) Y_{l_jm_l_j}(\Omega_{N+1}) r_{N+1}^{-1} \eta_{fj}^{(-)}(r_{N+1}), \end{aligned} \quad (4.14)$$

where $\eta_{fj}^{(-)}$ is the radial component of the continuum electron wavefunction (for simplicity we consider $j = jl_jm_l_j$ and $f = l_fm_l_f$) satisfying ingoing wave boundary conditions

$$\eta_{fj}^{(-)}(r) \underset{r \rightarrow \infty}{=} \begin{cases} \frac{i}{(2\pi k_j)^{1/2}} [e^{i\theta_j(r)} \delta_{fj} - S_{fj}^\dagger e^{-i\theta_j(r)}], & \text{for } k \geq 0 \\ e^{-\theta_j(r)}, & \text{for } k < 0 \end{cases}$$

where $\theta_j(r) = k_j r - \frac{l_j}{2}\pi - \beta_j \ln 2k_j r + \sigma_{l_j}$ and S_{jf}^\dagger is the Hermitian conjugate of the S-Matrix.

For convenience, we define

$$\begin{aligned} \Psi_{fl_fm_l_f}^{(-)(N+1)} &= \sum_{jl_jm_l_j} i^{l_j} e^{-i\sigma_{l_j}} Y_{l_jm_l_j}^*(\hat{\mathbf{k}}_j) \tilde{\Phi}_j^{SM_S}(\mathbf{r}_1, \dots, \mathbf{r}_N; \sigma_{N+1}) \\ &\times r_{N+1}^{-1} \eta_{fj}^{(-)}(r_{N+1}) Y_{l_fm_l_f}(\Omega_{N+1}). \end{aligned} \quad (4.15)$$

Substituting now Eq.4.14 and Eq.4.4 in Eq.4.3 we have that

$$\mathbf{d}_{fi} = \sum_{l_fm_l_f} \sum_{m_\gamma} i^{l_f} e^{-i\sigma_{l_f}} Y_{l_fm_l_f}^*(\mathbf{k}_f) (S_f M_{S_f} \frac{1}{2} m_f | SM_S) D_{\mu m_\gamma}^{1*} \mathbf{d}_{fl_fm_l_f i, m_\gamma}(\mathbf{k}_f), \quad (4.16)$$

where we defined the partial wave dipoles as

$$\mathbf{d}_{fl_fm_l_f i, m_\gamma}(\mathbf{k}_f) = \left[\frac{4\pi}{3} \right]^{1/2} \langle \Psi_{fl_fm_l_f}^{(N+1)(-)}(\mathbf{k}_f) | \sum_{n=1}^{N+1} r_n Y_{1m_\gamma}(\hat{\mathbf{r}}_n) | \Phi_i^{N+1} \rangle, \quad (4.17)$$

It is useful to define the coupling rules for spherical harmonics

$$\begin{aligned} Y_{l_fm_l_f}(\hat{\mathbf{k}}_f) Y_{\tilde{l}_f m_{\tilde{l}_f}}^*(\hat{\mathbf{k}}_f) &= (-1)^{m_{\tilde{l}_f}} \left[\frac{(2l_f+1)(2\tilde{l}_f+1)}{4\pi} \right]^{1/2} \sum_{K_l} (2K_l+1)^{-1/2} \\ &\times (l_fm_l_f \tilde{l}_f - m_{\tilde{l}_f} | K_l M_l) (l_f 0 \tilde{l}_f 0 | K_l 0) Y_{K_l M_l}(\mathbf{k}_f) \end{aligned} \quad (4.18)$$

where $M_l = m_{l_f} - m_{\tilde{l}_f}$ and K_l is given by the angular momentum addition rules. We also define coupling rules for the Wigner matrices as

$$D_{\mu m_\gamma}^{1*}(\alpha, \beta, \gamma) D_{\mu \tilde{m}_\gamma}^1(\alpha, \beta, \gamma) = (-1)^{\mu - m_\gamma} \sum_{K_\gamma} (1 - \mu 1 \mu | K_\gamma 0) \\ \times (1 - m_\gamma 1 \tilde{m}_\gamma | K_\gamma M_\gamma) D_{0 \tilde{M}_\gamma}^{K_\gamma}(\alpha, \beta, \gamma) \quad (4.19)$$

where $M_\gamma = \tilde{m}_\gamma - m_\gamma$ and K_γ is found also by the angular momentum addition rules.

Substituting Eq.4.16 in Eq.4.5 and using Eq.4.18 and Eq.4.19, we obtain in the molecular frame

$$\left(\frac{d\sigma_{fi}}{d\mathbf{k}_f} \right)_{\text{spin avg.}} = 4\pi^2 \alpha a_0^2 \omega \sum_{K_l \tilde{M}_l} \sum_{l_f \tilde{l}_f} i^{\tilde{l}_f - l_f} e^{\sigma_{l_f} - \sigma_{\tilde{l}_f}} \left[\frac{(2l_f + 1)(2\tilde{l}_f + 1)}{4\pi(2K_l + 1)} \right]^{1/2} \\ \times \sum_{m_{l_f} m_{\tilde{l}_f} m_\gamma \tilde{m}_\gamma} (-1)^{\mu - m_\gamma + m_{\tilde{l}_f}} \mathbf{d}_{f l_f m_{l_f} i, m_\gamma}(\mathbf{k}_f) \mathbf{d}_{f \tilde{l}_f m_{\tilde{l}_f} i, \tilde{m}_\gamma}^*(\mathbf{k}_f) \sum_{K_\gamma} (1 - m_\gamma 1 \tilde{m}_\gamma | K_l M_l) \\ \times (l_f m_{l_f} \tilde{l}_f - m_{\tilde{l}_f} | K_l M_l) (1 - \mu 1 \mu | K_\gamma 0) (l_f 0 \tilde{l}_f 0 | K_l 0) D_{0 \tilde{M}_\gamma}^{K_\gamma}(\alpha, \beta, \gamma) Y_{K_l \tilde{M}_l}(\hat{\mathbf{k}}_f). \quad (4.20)$$

Transforming the photoelectrons from molecular to lab frame we finally find that

$$\left(\frac{d\sigma_{fi}}{d\mathbf{k}'_f} \right)_{\text{spin avg.}} = \sum_{K_l \tilde{M}_l} A'_{K_l \tilde{M}_l} Y_{K_l \tilde{M}_l}(\hat{\mathbf{k}}'_f), \quad (4.21)$$

with the $A'_{K_l \tilde{M}_l}$ coefficients given by

$$A_{K_l \tilde{M}_l} = 4\pi^2 \alpha a_0^2 \omega \sum_{l_f \tilde{l}_f} i^{\tilde{l}_f - l_f} e^{\sigma_{l_f} - \sigma_{\tilde{l}_f}} \left[\frac{(2l_f + 1)(2\tilde{l}_f + 1)}{4\pi} \right]^{1/2} \sum_{\substack{m_{l_f} m_{\tilde{l}_f} \\ m_\gamma \tilde{m}_\gamma}} (-1)^{\mu - m_\gamma + m_{\tilde{l}_f}} \\ \times \mathbf{d}_{f l_f m_{l_f} i, m_\gamma}(\mathbf{k}_f) \mathbf{d}_{f \tilde{l}_f m_{\tilde{l}_f} i, \tilde{m}_\gamma}^*(\mathbf{k}_f) \sum_{K_\gamma} (2K_l + 1)^{-1/2} (1 - \mu 1 \mu | K_\gamma 0) \\ \times (1 - m_\gamma 1 \tilde{m}_\gamma | K_l M_l) (K_l \tilde{M}_l K_\gamma 0 | K \tilde{M}_l) (l_f m_{l_f} \tilde{l}_f - m_{\tilde{l}_f} | K_l M_l) (l_f 0 \tilde{l}_f 0 | K_l 0) \\ \times (K_l M_l K_\gamma M_\gamma | K M) D_{\tilde{M}_l M}^K(\alpha, \beta, \gamma). \quad (4.22)$$

Averaging the PAD over the molecular orientations, and assuming that the light field is polarized along the z direction, Eq.4.21 becomes

$$\frac{d\sigma_{fi}}{d\mathbf{k}'_f} = \sum_K A_K P_K(\cos \theta'_f), \quad (4.23)$$

with the A_K coefficients given by

$$A_K = 4\pi^2 \alpha a_0^2 \omega \sum_{\substack{l_f \tilde{l}_f \\ j_t m_\alpha}} (2j_t + 1)^{-1} i^{l'_f - l_f} e^{i(\sigma_{l_f} - i\sigma_{\tilde{l}_f})} \frac{2j_t + 1}{4\pi} \mathcal{D}_{fl_f j_t m_\alpha} \mathcal{D}_{f\tilde{l}_f j_t m_\alpha}^* \times [(2l_f + 1)(2\tilde{l}_f + 1)]^{1/2} (-1)^{j_t} \times (1010|K0)(l_f 0 \tilde{l}_f 0|K0) \begin{Bmatrix} 1 & 1 & K \\ l_f & \tilde{l}_f & j_t \end{Bmatrix} \quad (4.24)$$

where in brackets we have the Wigner 6-j symbol, and the dipoles $\mathcal{D}_{j\tilde{l}_j j_t m_\alpha}$ are defined in terms of the momentum transfer, j_t , introduced by Fano and Dill [136]

$$\mathcal{D}_{fl_f j_t m_\alpha} = \sum_{m_\gamma m_{l_f}} (-1)^{m_\gamma} (1 - m_\gamma l_f m_{l_f} | j_t m_{l_f} - m_\gamma) \mathbf{d}_{fl_f m_{l_f} i, m_\gamma}(\mathbf{k}_f), \quad (4.25)$$

with $m_{l_f} - m_\gamma = m_\alpha$ being fixed. Since only terms with $K = 0, 2$ have a non-zero contribution to the angular distribution, Eq.4.23 simplifies to

$$\overline{\left(\frac{d\sigma_{fi}}{d\mathbf{k}'_f} \right)}_{\text{spin avg.}} = \frac{\sigma_{fi}}{4\pi} (1 + \beta P_2(\cos \theta'_f)), \quad (4.26)$$

where σ_{fi} is the partial photoionization cross-section

$$\sigma_{fi} = \int \frac{d\sigma_{fi}}{d\hat{\mathbf{k}}'_f} d\hat{\mathbf{k}}'_f \quad (4.27)$$

and β is the asymmetry parameter (do not confuse this β with β_f)

$$\beta = \frac{A_2}{A_0}. \quad (4.28)$$

If the photon field is unpolarized, the same procedure derived above can be repeated for two linear fields polarized at right angles, yielding the following expression for the orientationally averaged PAD

$$\overline{\left(\frac{d\sigma_{fi}}{d\mathbf{k}'_f} \right)}_{\text{unpol}} = \frac{\sigma_{fi}}{4\pi} \left(1 - \frac{1}{2} \beta P_2(\cos \theta'_f) \right). \quad (4.29)$$

4.2 Experiments

In addition to the advances in the generation of XUV pulses in synchrotron facilities and HHG sources, two other developments were important for improving the quality of the information extracted from photoionization experiments. The first was the advance of imaging techniques, which now uses position sensitive microchannel plate detectors together with electrostatic optics for improving the acquisition of photoelectrons [137], greatly enhance the extent and precision of information obtained from photoionization experiments. The second key experimental development was the improvement of molecular alignment and orientation techniques [122, 138], which have allowed experimentalists in some cases to measure MFPAD and perform complete photoionization experiments for molecules [130, 131, 139].

There are currently three major methods which can either fully or partially recover the PAD in the molecular frame: photoelectron photoion coincidence (PEPICO) measurements [140, 141, 142], the adiabatic alignment and orientation technique [143, 144, 145, 146], and the field free alignment technique [147, 148, 149, 150]. The adiabatic alignment techniques involve external fields, which must be weak enough to not dramatically change the properties of the molecule prior or during the ionization step [122]. In the field-free alignment technique, an external field is used solely to induce molecular rotations leading to transient field-free alignment. Hence the main concern in this case is the possibility of vibrational excitation prior to ionization. fields during photo-ionization. On the other hand, PEPICO has the advantage of not requiring any external field prior to ionization, therefore not perturbing the molecule, and hence the characteristics of the MFPAD. In the following sections, we briefly discuss each of these three techniques and describe their advantages and disadvantages.

4.2.1 PEPICO

In this technique, the coincidence measurement of photoions and photoelectrons are used for inferring the recoil frame (RF) of the molecule with the help of the recoil frame approximation, which states that the direction of the fragment coincides with the direction of the breaking bond [151]. For this reason, PEPICO is only applicable for dissociative photoionization, which is usually the dominant process for the core ionization of molecules [152]. For linear molecules, the RFPAD coincides with the MFPAD (Fig.4.1a). For nonlinear

molecules, if photoionization is followed by only two fragments, there is an uncertainty on the orientation of the molecule in relation to rotations around the bond breaking axis (Fig.4.1c). If on the other hand the photoionization of the nonlinear molecule results in more than two fragments, the emission angle of the photoelectron is uniquely determined (Fig.4.1d). In addition, if the lifetime of the residual cation is longer than the rotational period of the molecule, the molecule rotates during dissociation and both RF and MF are lost (Fig.4.1b). Even though complete photoionization experiments of linear molecules using PEPICO have been performed [130, 131, 139], this technique still faces very challenging technical issues. Firstly, the detection of more than two fragments at each photoionization event in coincidence is a formidable technical challenge. Secondly, PEPICO requires less than one photoionization event per detection cycle making the application of this technique using the current low repetition rate FEL sources unpractical, (the X-FEL in Hamburg for example has a maximum repetition rate of 120Hz) [138].

4.2.2 Adiabatic alignment and orientation

In this technique a long elliptically polarized laser pulse (sometimes as long as tens of nanoseconds[122]) is used to orient a molecule adiabatically. The idea of adiabatic alignment and orientation is to align the axis of largest and second largest polarizability of the molecule with the respective major and minor axis of the elliptically polarized field. More precise orientation can be obtained for polar molecules by using a static electric field directed along the major axis of the laser pulse polarization in order to pre-align the molecule [143].

An important advantage of this technique in relation PEPICO, is that it does not require the fragmentation of the molecule after photoionization. There are however two important caveats: the alignment and orientation deteriorates for molecules with low polarizability, and external fields affect both the motion of the photoelectron, and the properties of the molecule if the fields are too strong[145, 146].

4.2.3 Field free alignment

The field free alignment technique uses a laser pulse with a duration much smaller than the rotational period of the molecule to impulsively align the

	$t=-\infty$	$t=0$	$t_1>0$	$t_2>t_1$	MFPAD
a)					✓
b)					✗
c)					✗
d)					✓

Figure 4.1: This figure illustrates the situations where the PEPICO technique is applicable for fully recovering the MFPAD. The molecule is photoionized at $t = 0$ and starts to dissociate at $t = t_1$.

molecule, creating a rotational wavepacket [147, 148]. After the laser pulse is over, the rotational wavepacket dephases and rephases, leading to periodic alignment revivals, generally on a picosecond timescale. As well as having a short duration, it is important that the pulse is not resonant with the molecular vibronic levels, and that the field has a moderate intensity in order to not ionize the molecule. One important advantage of this technique, is that it is applicable to molecules with a negligible permanent dipole [149, 150]. On the other hand, it is still a challenge to obtain a high degree of alignment with this technique for non-linear polyatomic molecules, for all axes of the polarizability tensor[147, 150].

Chapter 5

Molecular R-Matrix theory and the UKRmol package

The R-Matrix theory is a general method for investigating the scattering states of a system, irrespective of the nature of the particles involved in the process. The basic theory was developed by Wigner and Eisenbud in the 1940s, in the context of nuclear scattering [153, 154, 155]. Subsequently, the theory was adapted for studying electron scattering from atoms and molecules [156]. The power of the R-Matrix method lies in the generality of its basic approach: the partitioning of space into different regions, informed by the physics of the system, allowing the appropriate level of approximation and optimal numerical (or analytic) technique to be chosen in each. The usual division in electron-(photon)-molecule scattering is into an inner, outer and asymptotic region. The inner region is the most complex to treat, as the full multielectron nature of the process must be taken into account. In the outer region the continuum electron is sufficiently far from the bound electrons, so exchange can be neglected, and interactions with the target are mediated by a long range multipole potential. In the asymptotic region, the scattering wavefunction is well represented by an expansion of analytic functions, which are determined by asymptotic scattering theory.

In this chapter, we discuss the theoretical foundations of the molecular R-Matrix theory for electron-scattering and the photoionization of molecules. We also present the implementation of the R-Matrix theory in the UKRmol code suite. The UKRmol codes are freely available in the CCP collaborative

programming platform ^{1 2}.

This chapter is organized as follows: in section 5.1.1 we show how the scattering states are constructed in terms of a close coupling expansion. In section 5.1 we present the molecular R-Matrix theory and in section 5.2 we discuss the UKRmol codes used for treating electron-molecule scattering, as well as the recently developed UKRmol+. In section 5.3 and 5.4 we detail respectively the theoretical and numerical aspect (in the context of the UKRmol codes) for the calculation of photoionization with the R-Matrix method.

5.1 Molecular R-Matrix theory

5.1.1 Scattering states

Within the Born Oppenheimer approximation, which considers that the electrons are much faster than the nuclei, the $N + 1$ electron Hamiltonian of an atomic or molecular system is given by

$$\mathbf{H}^{N+1} = - \sum_i^{N+1} \left(\frac{\nabla^2}{2} + \sum_j^{nuclei} \frac{Z_j Z_i}{r_{ij}} \right) + \sum_{i>j}^{N+1} \frac{1}{r_{ij}} \frac{Z_j}{R_{ij}}, \quad (5.1)$$

where we have on the right hand side the electron kinetic energy operator, the electron-nuclear, the electron-electron and the nuclei-nuclei interaction respectively.

In the inner most region of the R-Matrix ($r \leq r_a$), the wavefunction of the system is written as

$$\Psi_f(E) = \sum_k A_{kf}(E) \psi_k^{(N+1)\Gamma}, \quad (5.2)$$

with $A_{kf}(E)$ being energy dependent expansion coefficients, and $\psi_k^{(N+1)\Gamma}$ are given in terms of the close coupling expansion

$$\begin{aligned} \psi_k^{(N+1)\Gamma} = & \mathcal{A} \sum_{i=1}^{n_c} \sum_{j=1}^{n_{cont}} a_{kij} \tilde{\Phi}_i^\Gamma(\mathbf{x}_1, \dots, \mathbf{x}_N; \sigma_{N+1}) \eta_{ij}(r_{N+1}) \\ & + \sum_p b_{kp} \chi_p^{(N+1)}(\mathbf{x}_1, \dots, \mathbf{x}_{N+1}), \end{aligned} \quad (5.3)$$

¹<https://ccpforge.cse.rl.ac.uk/gf/project/ukrmol-in/>

²<https://ccpforge.cse.rl.ac.uk/gf/project/ukrmol-out/>

where n_c is the number of channels, n_{cont} the number of continuum basis functions used in the expansion and Γ denotes the conserved quantities in the scattering process. In case of linear molecule for example, the conserved parameters are

$$\Gamma = \alpha S M_s \Lambda, \quad (5.4)$$

with S and M_s being the total spin and its projection in some preferred direction, Λ is the total orbital angular momentum of the electron-molecule projected in the molecular axis and α is any other conserved quantum number, e.g., the parity of the system if the linear molecule is symmetric with respect to the center of mass. η_{ij} are the radial part of the continuum orbitals orthogonalized with respect to the target states, \mathcal{A} is the antisymmetrisation operator, b_{kp} and a_{kij} are coefficients normally determined by a variational procedure.

In the second summation, $\chi_p^{(N+1)}$ are the so called L^2 configurations, which accounts for non-exchange electron correlation, polarization and help in converging the partial wave expansion by allowing the continuum electron to enter high angular momentum states close to the nuclei. They are formed by allowing the scattering electron to occupy target molecular orbitals. The reason they need to be explicitly added is because the one electron continuum functions representing the scattering electron is usually orthogonalised to the target molecular orbitals. Restricting the scattering electron to the continuum orbitals would now neglect an important part of the basis for the space, which prior to orthogonalisation corresponded to non-zero overlap between continuum and target.

We define $\tilde{\Phi}_i^\Gamma$, the channel functions, by spin coupling the target states and the continuum electron

$$\tilde{\Phi}_i^\Gamma(\mathbf{x}_1, \dots, \mathbf{x}_N; \sigma_{N+1}) = \sum_{M_{S_i} m_i} (S_i M_{S_i} \frac{1}{2} m_i | S M_S) \Phi_i^{(N)\Gamma}(\mathbf{x}_1, \dots, \mathbf{x}_N) \chi_{\frac{1}{2} m_i}(\sigma_{N+1}), \quad (5.5)$$

where $(\dots | \dots)$ are the Clebsch Gordan coefficients, $\chi_{\frac{1}{2} m_i}(\sigma_{N+1})$ is the spin function of the continuum electron, S, M_S are the total spin and spin component, S_i, M_{S_i} are the spin and spin component of the target states, and Γ are the conserved quantum numbers.

The close coupling expansion leads to exact results, if and only if, it is built on a basis that fully spans the Hilbert space of the system. As this is of course not computationally feasible, we must rely on several degrees of

approximation to describe the scattering wavefunctions, the most common being:

- The static exchange (SE) or Hartree Fock (HF) approximation: a single target state, represented by a single Slater determinant is considered in the close coupling expansion, thus no target correlation is considered, and the target molecule is not allowed to polarize. Autoionizing resonances are of course not described by SE models, since they emerge from excitations of the target states.
- The static exchange plus polarization (SEP) approximation: only a single target state, represented by a single Slater determinant is considered. The number of L^2 configurations of the close coupling expansion is considerably increased, by allowing excitations from the ground molecular configuration to the virtual orbitals, i.e., letting the molecule polarize in the presence of the incoming electron.
- The close coupling (CC) approximation: target states with open or weakly closed channels are included in the close coupling expansion (see chapter 1 for further details on the CC approximation). The L^2 configurations include polarization effects in the scattering wavefunction. In CC approximation of the scattering wavefunction, correlation is considered in both target and scattering wavefunctions.

5.1.2 Inner region

The power of the molecular R-Matrix theory, comes from partitioning the configuration space into an inner and outer region. The inner region must be large enough to contain all bound states of the target system, i.e., only the continuum orbitals have a non-zero amplitude on the R-Matrix boundary. Restriction to a finite space allows for discretization of the continuum and the use of basis set methods borrowed from quantum chemistry. Diagonalizing the inner region Hamiltonian can be a very demanding process, as the addition of a set of orbitals to represent the continuum greatly increases the size of the Hamiltonian, and in contrast to bound state electronic structure calculations, all (or a large subset) of the eigenvectors are required. Moreover, the partitioning of the configuration space at $r = r_a$ makes \mathbf{H}^{N+1} non-Hermitian, a difficulty that can be surpassed by introducing the Bloch operator on the

multielectron Hamiltonian [109] (see further details in Chapter 2)

$$[\mathbf{H}^{N+1} + \mathcal{L}^{N+1}(b_0) - E]\Psi_f^\Gamma(E) = \mathcal{L}^{N+1}(b_0)\Psi_f^\Gamma(E), \quad (5.6)$$

$$\mathcal{L}^{N+1}(b_0) = \frac{1}{2} \sum_{i=1}^{N+1} \delta(r_i - r_a) \left[\frac{d}{dr_i} + \frac{b_0}{r_i} \right]. \quad (5.7)$$

where b_0 is an arbitrary constant set to zero in the UKRmol package. $\Psi_f^\Gamma(E)$ are the scattering functions defined by Eq.5.2, with the a_{kij} and the b_{kp} determined by diagonalizing the Hermitian operator $H^{N+1} + \mathcal{L}^{N+1}$.

Rearranging Eq.5.6, we find that the scattering wavefunctions satisfy

$$|\Psi_f^\Gamma(E)\rangle = \frac{\mathcal{L}^{N+1}(b_0)|\Psi_f^\Gamma(E)\rangle}{\mathbf{H}^{N+1} + \mathcal{L}^{N+1}(b_0) - E}. \quad (5.8)$$

Expanding the Green function of $(H^{N+1} + \mathcal{L}^{N+1}(b_0) - E)^{-1}$ in the basis of $\psi_k^{(N+1)}$, since $\psi_k^{(N+1)}$ are eigenvectors of $H^{N+1} + \mathcal{L}^{N+1}(b_0)$, Eq. 5.8 becomes

$$|\Psi_f^\Gamma(E)\rangle = \sum_f \frac{1}{E_k - E} |\psi_k^{(N+1)\Gamma}\rangle \langle \psi_k^{(N+1)\Gamma} | \mathcal{L}^{N+1}(b_0) | \Psi_f^\Gamma(E)\rangle. \quad (5.9)$$

Projecting Eq. 5.9 on the channel functions $\tilde{\Phi}_i^\Gamma$, we find that at the boundary $r = r_a$ the radial part of the scattering electron satisfies

$$\eta_{fi}(r_a) = \sum_{i'} R_{ii'}(E, r_a) \left(r_a \frac{d\eta_{fi'}}{dr_{i'}} + b_0 \eta_{fi'} \right) \Big|_{r=r_a}, \quad (5.10)$$

with $R_{ii'}(E, r_a)$ being the R-matrix

$$R_{ii'}(E, r_a) = \frac{1}{2r_a} \sum_k \frac{\xi_{ik}(r_a)\xi_{i'k}(r_a)}{E_k - E}, \quad (5.11)$$

and the boundary amplitudes $\xi_{ij}(r_a)$ are given by

$$\xi_{ik}(r_a) = \langle r_{N+1}^{-1} \tilde{\Phi}_i^\Gamma | \psi_k^{(N+1)\Gamma} \rangle \Big|_{r_a}. \quad (5.12)$$

The primes in Eq. 5.12 indicate that the integration was taken over all electronic coordinates, except r_{N+1} . An advantageous consequence of this approach is that the energy dependent part of the scattering wavefunction at the boundary is contained exclusively in the R-Matrix (Eq. 5.11). Computationally, such a property is welcome, since it means that the complicated multi-electronic inner region need to be solved only once for a set of continuum orbitals spanning a given energy range.

5.1.3 Outer and Asymptotic region

Following the assumption that only the continuum electron reaches the R-Matrix boundary, solving the outer region becomes a simpler problem, since electronic exchange can be neglected. Moreover, for $r > r_a$ only long range multipole potentials have a non-vanishing amplitude. Thus, in the outer region the wavefunction is given by the following close coupling equation

$$\Psi_k(E) = \sum_i \tilde{\Phi}_i^\Gamma(\mathbf{x}_1, \dots, \mathbf{x}_N; \sigma_{N+1}) r_{N+1}^{-1} S_{l_i}^{m_i}(\Omega_{N+1}) F_{ik}(r_{N+1}), \quad (5.13)$$

where the summation goes over the partial wave channels. η_{ik} is the radial part of the continuum electron spin coupled to the ionic states, and $S_{l_i}^{m_i}(\Omega_{N+1})$ are real spherical harmonics representing the angular part of the continuum electron.

Following the derivations in section 2.4.1, we obtain the following Schrödinger equations for the one-electron system

$$\left[-\frac{d^2}{dr^2} + \frac{l_i(l_i + 1)}{r^2} - \frac{2Z}{r} - k_i^2 \right] F_{ik}(r) = 2 \sum_{i'} V_{ii'} F_{i'k}(r), \quad (5.14)$$

$$\langle r_{N+1}^{-1} \tilde{\Phi}_i^\Gamma | \mathbf{H}^N | r_{N+1}^{-1} \tilde{\Phi}_i^\Gamma \rangle = E_i^N. \quad (5.15)$$

It is not unusual that the $V_{ii'}$ potential decays slowly and is not negligible at the R-Matrix radius r_a . Thus at r_a the continuum electron is still not asymptotically free.

There are several ways of treating this issue. One method, is to numerically propagate the R-Matrix from r_a up to a radius r_p where the potential $V_{ii'}$ is weak. The propagation is mediated by the one-electron Schrödinger equation that dictates the wavefunction of the continuum electron in the outer region. On the other hand, the asymptotic solutions of the system are back propagated from the asymptotic limit to $r = r_p$ via an asymptotic expansion method [157]. At r_p the eigenfunctions of the inner region can be constructed from the R-Matrix. At the matching radius r_p we have that

$$\mathbf{F}(r_p) = k^{-1/2} \left[\mathbf{s}(kr_p) + \mathbf{c}(kr_p) \mathbf{N} \right], \quad (5.16)$$

where $s_{ij}(kr_p)$ and $c(kr_p)$ are the regular and irregular back propagated asymptotic solutions of the system, and

$$\mathbf{N} = \begin{pmatrix} \mathbf{K} \\ \mathbf{L} \end{pmatrix}$$

\mathbf{K} is the usual K-Matrix and \mathbf{L} multiplies the exponentially decaying irregular asymptotic solutions of the system, i.e., the closed channels. All relevant observables in electron scattering are extracted from the K-Matrix. On the other hand, in photoionization the explicit form of the scattering wavefunction needs to be evaluated and one needs the full N matrix.

Setting b_0 to zero, the relation between the R-Matrix and the eigenfunctions \mathbf{F} is given by

$$\mathbf{F} = \mathbf{R}(E, r_a)\mathbf{F}'. \quad (5.17)$$

Taking the derivative of Eq.5.16 and substituting it in Eq.5.17 we obtain the following relation between the \mathbf{N} and the R-Matrix

$$\mathbf{R}(E, r_a) = \frac{\mathbf{s}(kr_a) + \mathbf{s}(kr_a)\mathbf{N}}{\mathbf{s}'(kr_a) + \mathbf{c}'(kr_a)\mathbf{N}}. \quad (5.18)$$

5.2 The UKRmol package

Calculations with the UKRmol package are divided in three basic stages: target preparation, inner region calculation and outer region calculation. In the target preparation, we specify the atomic basis set and degree of complexity (HF, CI or MRCI models) employed in the description of the target states, which will be later used in the close coupling expansion (Eq.5.3). The most important output in the target preparation step is the calculation of the target energies and target properties, which are used in the subsequent outer region calculation for setting up the multipole potential in Eq.5.14. In the inner region calculation there are two important tasks: (i) the generation of the continuum orbitals, so we can construct the close coupling expansion used for representing the scattering states; and (ii) the diagonalization of $N+1$ electron system, in order to determine the eigenvalues and eigenfunctions of the inner region. Finally, the outer region calculations gathers the information from the target preparation and inner region calculations, constructs the R-Matrix using the inner region eigenvalues and eigenfunctions, and calculates the scattering observables at the radius where solutions coming from the inner region and the asymptotic limit are matched.

Below, we will explain in more detail all of these three steps. The flow charts in Fig.5.1, Fig.5.2 and Fig.5.3 are used for a better visualization of how the UKRmol calculations are performed.

5.2.1 Target preparation

The first step in the calculation is to generate the molecular orbitals. The molecular geometry and atomic basis set are read by SWMOL3, which calculates the 1- and 2-electron integrals. Subsequently the integrals are ordered by the module SWORD. With all integrals in hand, we can proceed to the generation of the molecular orbitals. In older versions of the codes the user was restricted to generating the target orbitals with a Hartree Fock method via the module SWSCF. Currently, one can use the MOLPRO quantum chemistry package in order to generate molecular orbitals with sophisticated quantum chemistry methods, such as MCSCF, SA-MCSCF, etc. The module MPOUTRD reads the MOLPRO molecular orbitals in to the R-Matrix codes. SWEDMOS is then used to orthogonalize the molecular orbitals, and SWTRMO performs the transformations of the 1-2 electron integrals from the atomic to the molecular basis. The CSF for a set of target states belonging to a given irreducible representation and spin are generated from the specifications of the frozen and active orbitals given by the user with the module CONGEN. Subsequently, SCATCI reads the CSFs and integral information in order to construct and diagonalize the target Hamiltonian for each irreducible representation and target spin. Finally, DENPROP constructs the density matrix for all target states specified by the user and calculates the molecular properties such as the dipole and quadrupole moments, which are necessary for the evaluation of the multipole potential in the outer region.

5.2.2 Inner region

The generation of a good continuum orbital basis is critical for the inner region calculations. In the UKRmol codes the continuum is discretized and a set of continuum orbitals are obtained with the modules NUMCBAS and GTOBAS [107], which solve Eq.5.14, with a model potential V_0 , neglecting the correlation and exchange potentials, and subject to the homogeneous boundary conditions

$$\eta_{ij}(0) = 0 \quad \text{for } l \neq 0, \quad (5.19)$$

$$\frac{1}{\eta_{ij}(r_a)} \left[\frac{d\eta_{ij}(r_a)}{dr} \right] = 0, \quad (5.20)$$

where r_a is the R-matrix radius. In order to facilitate the evaluation of the 1- and 2- electron integrals, the continuum orbitals are also given in terms

of gaussian-type functions centered in the molecular center of mass

$$\eta_{ij}(r_{N+1}) = \frac{1}{r_{N+1}} \sum_{j=1}^{n_{cont}} c_{ij} \exp(-\alpha_{ij}r^2). \quad (5.21)$$

Gaussian type orbitals (GTO) struggles to reproduce fast oscillations at large distances from the target molecule. Currently, this problem is being addressed by an extension of the UKRmol codes to support B-splines continuum basis functions.

After the generation of the continuum orbitals, the integrals and their tail i.e., for the integration limits $r_a < r < \infty$, are calculated with SWMOL3 and GAUSTAIL respectively. Since the inner region is confined by the R-Matrix sphere, the module SWORD is used to subtract the tail of the integrals from the output of SWMOL3. Similar to the target preparation step, SWEDMOS orthogonalizes the orbitals, and discards all continuum orbitals that do not satisfy a given orthogonalization threshold (usually 10^{-7} in the UKRmol codes). SWEDMOS also calculates the boundary amplitude of the orthogonal continuum orbitals on the R-Matrix boundary for subsequent use in the outer region. SWRTO then transforms the integrals from the primitive GTO to the target+continuum molecular basis. Finally CONGEN is used again to generate the scattering models that are discussed in detail below, and SCATCI constructs and diagonalizes the target+continuum Hamiltonian matrix, obtaining then the inner region eigenvalues and CI vectors.

5.2.3 Outer region

The outer region stage is considerably simpler than the target preparation and inner region calculation steps. The interface between outer region and the previous computations is done by the module SWINTERF, which constructs the R-Matrix from the boundary amplitudes, the inner region eigenvalues and CI vectors. SWINTERF also reads the target states dipoles and quadrupoles, and compute the multipole potential necessary for propagating the R-Matrix in the outer region (see Eq.5.14). RSOLVE performs the propagation until a radius r_p where the multipole potential is negligible, and matches the numerical R-Matrix with Bessel (Coulomb) functions for scattering with neutral (ionic) targets, obtaining the K-Matrix, as shown in Eq.5.16. The eigenphase sums are calculated by the module EIGENP, by

diagonalizing the K-Matrix

$$\theta = \sum_i \arctan(K_{ii}), \quad (5.22)$$

where the sum is over the open channels. The resonances which are observed as a π jump in the eigenphase sum, can be characterized by the module RESON. Finally the module TMATRXX calculates the T-Matrix from the K-Matrix as shown in Chapter 1, and the module IXSEC outputs the cross section for each irreducible representation of the scattering states.

There are other modules in the outer region of the UKRmol codes that have not been used in this thesis. For example the module POLYDCS calculates differential electron scattering cross section. TIMEDEL provides an alternative analysis of the resonances found in the eigenphase sum, based on a time delay analysis, and BORNCROSS calculates the Born corrections of the inelastic scattering.

5.2.4 The UKRmol+ codes

UKRmol+ is a modern version of the UKRmol package, which removes many of the structural and organizational problems of the old codes. This functionality of the new integral codes considerably simplifies the amount of input that needs to be generated manually. Molecular orbitals, gaussian basis set and molecular geometry are now read from a Molden format, which can be for example generate by MOLPRO. In the new UKRmol+, the SWEDEN based integral modules (SWMOL3,SWEDMOS,SWORD,SWTRMO,GAUSTAIL) have been replaced with an interface to a new, object-oriented, integral library. The new module SCATCLINTEGRALS uses the library's object to generate, in parallel, all the required molecular integrals and stores them in the disk. The interface of the UKRmol+ then allows to access these integrals by all programs of the suite. The performance and capabilities of the new integral codes significantly surpass those of the SWEDEN based codes, enabling of more complex molecules.[158, 159, 160]

5.3 Photoionization with the R-Matrix method

To calculate transition dipoles and photoionization/recombination observables we need the expansion coefficients for the initial and final states in the inner region and transition dipoles between the inner region states. In contrast, only the expansion coefficients in terms of the asymptotic solutions are required to obtain scattering observables.

Following the derivations in chapter 4, the photoelectron angular distribution is given by

$$\frac{d\sigma_{fi}}{d\Omega'_k} = 4\alpha\omega(\pi a_0)^2 |\langle \Psi_f^{(\pm)(N+1)\Gamma} | \mathbf{d} \cdot \hat{\mathbf{e}} | \Phi_i^{(N+1)\Gamma} \rangle|^2, \quad (5.23)$$

where α is the fine structure constant, ω is the photon energy, a_0 the Bohr radius and $\hat{\mathbf{e}}$ the polarization of the incident radiation. In analogy to chapter 4 primed and unprimed variables denote laboratory and molecular frame respectively. The explicit expression of the scattering and bound wavefunctions are respectively written as

$$\Psi_f^{(\pm)(N+1)\Gamma} = \sum_k A_{fk}^{(\pm)} \psi_k^{(N+1)\Gamma}, \quad (5.24)$$

$$\Phi_i^{(N+1)\Gamma} = \sum_k B_{ik'} \psi_{k'}^{(N+1)\Gamma}. \quad (5.25)$$

Primes indicate laboratory frame quantities, plus or minus in the superscripts denotes that the wavefunction satisfy outgoing boundary conditions (for photorecombination) and incoming (for photoionization) boundary conditions, appropriate for photon processes [135]

$$\mathbf{F}^{\pm} = \sqrt{\frac{2}{\pi}} \mathbf{F} [\mathbf{1} \mp i\mathbf{K}]^{-1}, \quad (5.26)$$

where \mathbf{K} is the open-open block of the K-Matrix. Substituting Eq.5.24 and Eq.5.25 in Eq.5.23 we obtain

$$\frac{d\sigma_{fi}}{d\Omega'_k} \propto |\mathbf{d} \cdot \hat{\mathbf{e}}|^2, \quad (5.27)$$

where the laser field is polarized in the $\hat{\epsilon}$ direction and

$$\begin{aligned} \mathbf{d}_{fi}(\mathbf{k}_f) &= \sum_{kk'} \sum_{l_f m_f} i^{-l_f} e^{i\sigma_{l_f}} Y_{l_f m_f}(\hat{\mathbf{k}}_f) (S_f M_{S_f \frac{1}{2}} m_{s_f} | S M_S) \\ &\times A_{fl_i m_f k}^*(E) \langle \psi_k^{(N+1)} | \mathbf{d} | \psi_{k'}^{(N+1)} \rangle B_{ik'}, \end{aligned} \quad (5.28)$$

here $\sigma_{l_f} = \arg \Gamma(l_f + 1 + i\eta_f)$ is the Coulomb phase, with $\eta_f = -\frac{Z-(N-1)}{k_f}$, where $Z - (N - 1)$ is the residual charge on the ion. The Clebsch-Gordan coefficient is due to spin coupling of the continuum electron and the ion. The partial wave dipole is defined as follows

$$\mathbf{d}_{fl_f m_f i}(E) = \sum_{kk'} A_{fl_f m_f k}^*(E) \langle \psi_k^{(N+1)} | \mathbf{d} | \psi_{k'}^{(N+1)} \rangle B_{ik'} \quad (5.29)$$

Since the UKRmol codes work in a real spherical harmonics basis, we need to transform the real calculated dipoles $\mathbf{d}_{fl_f m_f i}^{(\text{Re})}(E)$ to the complex spherical harmonics basis via

$$\mathbf{d}_{fl_f m_f i}(E) = \sum_{m'_f} \mathbf{C}^{1\dagger} \mathbf{d}_{fl_f m'_f i}^{(\text{Re})}(E) C_{m'_f m_f}^{l_f}, \quad (5.30)$$

where $C_{m'_f m_f}^{l_f}$ comes from the following relation between real and spherical harmonics (written below in the vector form) [161],

$$\mathbf{S}_{l_f} = \mathbf{C}^{l_f} \mathbf{Y}_{l_f}. \quad (5.31)$$

To connect to the lab frame observables, we introduce Euler angles α, β, γ , which define the rotation of molecule from the lab frame, and the associated Wigner rotation matrices (see, for example [134]), $\mathbf{D}^l(\alpha, \beta, \gamma)$. In the lab frame eq. 5.29 becomes,

$$\begin{aligned} \mathbf{d}'_{fi}(\mathbf{k}'_f) &= \sum_{l_f m'_f m_f} i^{-l_f} e^{i\sigma_{l_f}} Y_{l_f m'_f}(\hat{\mathbf{k}}'_f) (S_f M_{S_f \frac{1}{2}} m_{s_f} | S M_S) \\ &D_{m'_f m_f}^{l_f} \mathbf{d}_{fl_f m_f i}(E) \mathbf{D}^{1\dagger}, \end{aligned} \quad (5.32)$$

where the primed variables indicate lab frame quantities. Below, we will detail how to get the expansion coefficients of the scattering states, the bound states and the dipole between the inner region eigenfunctions for calculating the photoionization observables.

5.3.1 Expansion coefficients

Eq. (5.24) allows us to write the radial wavefunction in terms of the expansion coefficients and boundary amplitudes as follows,

$$\mathbf{F}^\pm = \mathbf{w}\mathbf{A}^\pm, \quad (5.33)$$

remembering that the R-matrix relates the radial function and its derivative we can write

$$\mathbf{w}\mathbf{A}^\pm = \mathbf{R}\mathbf{F}'^\pm \quad (5.34)$$

$$= \frac{1}{2}\mathbf{w}[\mathbf{E}_k - E]^{-1}\mathbf{w}^T\mathbf{F}'^\pm \quad (5.35)$$

from which it is easy to see that

$$\mathbf{A}^\pm = \frac{1}{2}[\mathbf{E}_k - E]^{-1}\mathbf{w}^T\mathbf{F}'^\pm \quad (5.36)$$

or alternatively

$$\mathbf{A}^\pm = \frac{1}{2}[\mathbf{E}_k - E]^{-1}\mathbf{w}^T\mathbf{R}^{-1}\mathbf{F}^\pm. \quad (5.37)$$

5.3.2 Bound states and inner region dipoles

Bound states required to describe the initial(/final) state for photoionization(/recombination) can be produced in several ways: they can be constructed using standard quantum chemistry techniques, with the proviso that the same set of orbitals must be used as was used for the target calculation; they can be constructed from the inner region wavefunctions by considering all channels to be closed, using the outer region module BOUND [162]; lastly, it can be a good approximation to take the lowest energy inner region wavefunction of the appropriate symmetry to represent the ground state of the neutral molecule [163].

5.3.3 Calculating the dipoles

All one electron properties can be calculated from the one-electron transition density matrix,

$$\begin{aligned} \rho_{kl}^N = N \int & \psi_k^{(N)}(x_1, \dots, x_N, x_{N+1}) \\ & \times \psi_l^{(N)}(x_1, \dots, x_N, x_{N+1}) dx_1 \dots dx_N, \end{aligned} \quad (5.38)$$

and constructing it is half the battle. In this section we see how to take advantage of the structure of the inner region basis to simplify its calculation. Inserting eq. (5.3) into eq. (5.38) we get

$$\begin{aligned}
\rho_{kl}^N &= N \int \sum_{im} \sum_{jn} a_{kim} a'_{ljn} \mathcal{A}[\Phi_i^{(N)} \eta_m] \mathcal{A}[\Phi_j^{(N)} \eta_n] dx_1 \dots dx_N \\
&+ N \int \sum_{im} \sum_q a_{kim} b'_{lq} \mathcal{A}[\Phi_i^{(N)} \eta_m] \chi_q^{(N+1)} dx_1 \dots dx_N \\
&+ N \int \sum_p \sum_{jn} b_{kp} a'_{ljn} \chi_p^{(N+1)} \mathcal{A}[\Phi_j^{(N)} \eta_n] dx_1 \dots dx_N \\
&+ N \int \sum_p \sum_q b_{kp} b'_{lq} \chi_p^{(N+1)} \chi_q^{(N+1)} dx_1 \dots dx_N, \tag{5.39}
\end{aligned}$$

which we can write in matrix form as

$$\boldsymbol{\rho}^N = \begin{bmatrix} \mathbf{a} & \mathbf{b} \end{bmatrix} \begin{bmatrix} \boldsymbol{\varrho}^{\text{C-C}} & \boldsymbol{\varrho}^{\text{C-L}^2} \\ \boldsymbol{\varrho}^{\text{L}^2\text{-C}} & \boldsymbol{\varrho}^{\text{L}^2\text{-L}^2} \end{bmatrix} \begin{bmatrix} \mathbf{a}' \\ \mathbf{b}' \end{bmatrix}. \tag{5.40}$$

We look first at the diagonal blocks of the matrix $\boldsymbol{\varrho}$. The $\text{L}^2 - \text{L}^2$ block has elements,

$$\varrho_{pq}^{\text{L}^2\text{-L}^2} = N \int \chi_p^{(N+1)} \chi_q^{(N+1)} dx_1 \dots dx_N, \tag{5.41}$$

which have L^2 functions for both initial and final state, and can be evaluated using Slater's rules. The $\text{C} - \text{C}$ block,

$$\varrho_{imjn}^{\text{C-C}} = N \int \mathcal{A}[\Phi_i^{(N)} \eta_m] \mathcal{A}[\Phi_j^{(N)} \eta_n] dx_1 \dots dx_N, \tag{5.42}$$

in which both initial and final states contain continuum orbitals, can be reduced, using the orthonormality of bound and continuum orbitals, and of bound states, to

$$\varrho_{imjn}^{\text{C-C}} = \delta_{ij} \eta_m \eta_n + \delta_{mn} \rho_{ij}^N \tag{5.43}$$

where ρ_{ij}^N is the transition density matrix for the target molecule.

Now considering the off diagonal blocks,

$$\begin{aligned}\varrho_{imq}^{\text{C-L}^2} &= N \int \mathcal{A}[\Phi_i^{(N)} \eta_m] \chi_q^{(N+1)} dx_1 \dots dx_N \\ \varrho_{pjn}^{\text{L}^2\text{-C}} &= N \int \chi_p^{(N+1)} \mathcal{A}[\Phi_j^{(N)} \eta_m] dx_1 \dots dx_N,\end{aligned}\quad (5.44)$$

which become

$$\begin{aligned}\varrho_{imq}^{\text{C-L}^2} &= \eta_m D_{iq}^X \\ \varrho_{pjn}^{\text{L}^2\text{-C}} &= D_{pj}^X \eta_m,\end{aligned}\quad (5.45)$$

where $D_{iq}^X = \sqrt{N} \int \Phi_i^{(N)} \chi_q^{(N+1)} dx_1 \dots dx_N$. To evaluate D_{iq}^X we need to first expand the target states in their CSF basis, $\Phi_i^{(N)} = \sum_r c_{ir} \chi_r^{(N)}$.

$$\begin{aligned}D_{iq}^X &= \sqrt{N} \int \sum_r c_{ir} \chi_r^{(N)} \chi_q^{(N+1)} dx_1 \dots dx_N \\ &= \sum_r c_{ir} D_{rq}^{\text{XX}},\end{aligned}\quad (5.46)$$

where $D_{rq}^{\text{XX}} = \sqrt{N} \int \chi_r^{(N)} \chi_q^{(N+1)} dx_1 \dots dx_N$. This is straightforward to calculate in principle by checking if the set of target orbitals in $\chi_r^{(N)}$ is a subset of the orbitals in $\chi_q^{(N+1)}$. In practice however, due to the manner in which the contracted basis is initially created, it is simpler to use Slater's rules on the integral $(N+1) \int \chi_r^{(N)} \eta_m \chi_q^{(N+1)} dx_1 \dots dx_N = \eta_m D_{rq}^{\text{XX}}$

Transition moments

Once $\boldsymbol{\varrho}$ has been constructed we can construct the moments matrix, \mathcal{M} , as follows,

$$\mathcal{M} = \int \mu \boldsymbol{\varrho} d\mathbf{x}, \quad (5.47)$$

where μ is the transition moment operator (dipole, quadrupole etc) The final step in calculating the transition moments between the inner region basis functions, \mathbf{M} , is then simply to multiply in the coefficient matrices.

$$\mathbf{M} = \begin{bmatrix} \mathbf{a} & \mathbf{b} \end{bmatrix} \mathcal{M} \begin{bmatrix} \mathbf{a}' \\ \mathbf{b}' \end{bmatrix}. \quad (5.48)$$

5.4 Photoionization with the UKRmol package

In order to adapt the UKRmol codes to calculate photoionization observables, we have developed the new module CDENPROP for the calculation of the inner region dipoles. In the outer region we calculate the wavefunction coefficients using either Eq.5.36 or Eq.5.37 and the partial wave dipoles using Eq.5.29, which required adaptations to the module RSOLVE. Finally we developed the new module DIPELM, which uses the partial wave dipoles to calculate all photoionization observables. Below, we explain the functionality of the new codes. A detailed explanation of the input for both programs can be found in the code repository^{1 2}.

5.4.1 CDENPROP

CDENPROP resides primarily in the inner region stage, the red rectangle in Fig.5.2 shows a schematic of the various inner region codes with the most important inputs and outputs. The shaded rectangle indicates steps required to produce inner region dipoles, including the new module CDENPROP that implements the theory of the preceding section. CDENPROP takes as input, target states and transition dipoles from the target calculation, dipole integrals between both bound and continuum orbitals restricted to the inner region, inner regions wavefunctions (the $(N + 1)$ CI vectors in Fig.5.2) and, optionally, bound states produced by the outer region code BOUND. It outputs the inner region dipoles and Dyson orbitals. We note that CDENPROP is also capable of calculating transition dipoles between the target states.

CDENPROP borrows routines from the existing UKRmol code, DENPROP, for the application of Slater's rules. Aside from the construction of the density matrix, there is another key difference between the two codes. DENPROP constructs the density matrix for each state pair, reducing the density matrix in symbolic form to a small set of orbitals pairs and corresponding coefficients, and then picks up the relevant dipole integrals, a procedure that is memory efficient but scales like $\mathcal{O}(n^4)$ with the basis set size, n , this is ameliorated by the sparseness of the density matrix when each basis function is a single Slater determinant, and by the fact that, generally,

¹<https://ccpforge.cse.rl.ac.uk/gf/project/ukrmol-in/>

²<https://ccpforge.cse.rl.ac.uk/gf/project/ukrmol-out/>

during a target run, only a small subset of the target states are required. Neither of these conditions hold in the inner region, where the contracted basis leads to the $C - L^2$ blocks being non-sparse and where dipoles between all the inner region wavefunctions may be required. The procedure DENPROP uses rapidly becomes unfeasible as the basis set size increases. The technique outlined in the previous section picks up the dipole integrals first, and then multiplies in the state coefficients, giving a scaling of $\mathcal{O}(n^3)$ and only requiring a single pickup of the dipole integrals, but pays a penalty in increased memory requirements. We use sparse matrix routines throughout the code where appropriate. It is important to note that the memory requirements are of the same order as the Hamiltonian construction and diagonalization code SCATCI [164] and so memory issues tend to show up, and are addressed, at this stage, prior to reaching CDENPROP.

5.4.2 DIPELM

The module DIPELM reads the partial wave dipoles from the adapted RSOLVE, and creates the angular grid for defining the real spherical harmonics and the Wigner rotation Matrices. Subsequently, DIPELM performs the necessary frame transformations and calculates the LFPAD in an angular grid using Eq.4.21. DIPELM outputs not only oriented observables, but also orientationally averaged partial photoionization cross section (simply by averaging Eq.4.21 over different molecular orientations) and asymmetry parameters (using Eq.4.23).

An extra feature in DIPELM, is the possibility of smoothing the partial wave dipoles, in order to remove narrow peaked autoionizing resonances. This makes the comparison of the calculations to experimental data easier, if the latter does not have enough energy resolution to observe the autoionizing resonances.

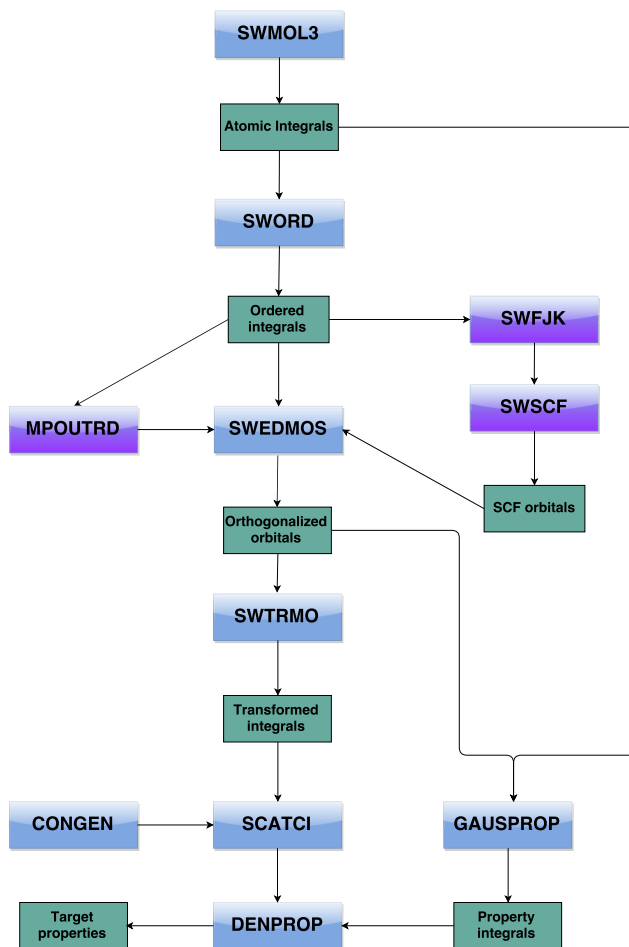


Figure 5.1: Flow chart of the target calculation in the UKRmol package.

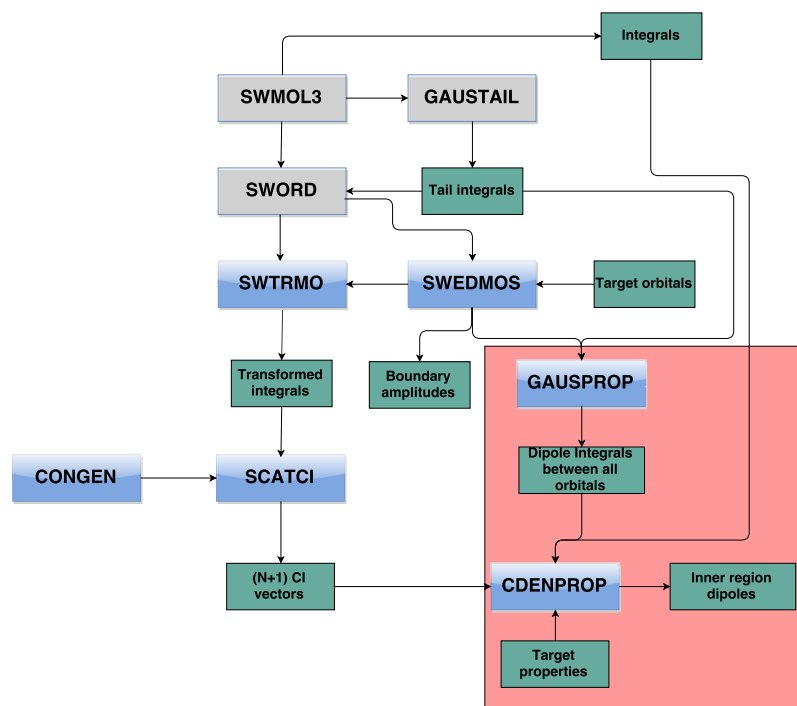


Figure 5.2: Flow chart of the inner-region modules in the UKRmol package.

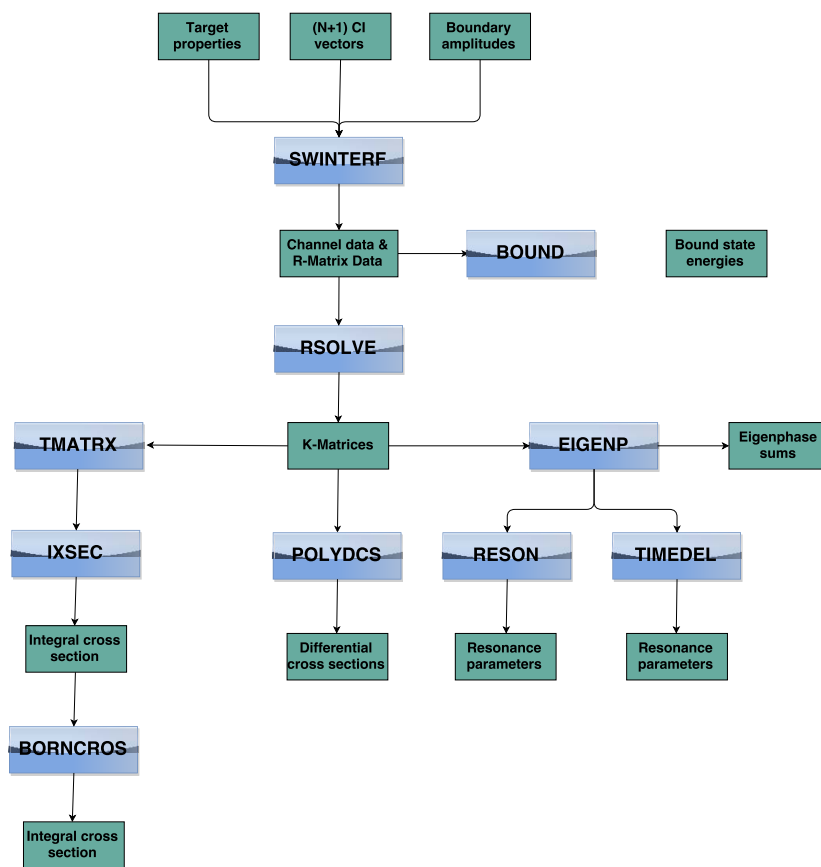


Figure 5.3: Flow chart of the outer-region modules in the UKRmol package.

Chapter 6

Photoionization of molecules in the equilibrium geometry

In this chapter we calculate the one-photoionization from the ground state of N_2 , CO_2 and NO_2 in their respective equilibrium geometry using the UKRmol package and the new modules, detailed in Chapter 5, developed by us for this purpose. There is an extensive list of calculations and experiments investigating the photoionization of these molecules, which allow us to benchmark the recently developed modules that adapt the UKRmol package to treat photoionization. The calculations presented here were also applied to several other physical processes:

- The calculations of N_2 were used in the recent work of Medisauskas *et al.* [165], where they demonstrate how the phase of the ionic states acquired in photoionization affects the dissociative photoionization of N_2 ;
- In chapter 9 we evaluate the high harmonic spectra of CO_2 using photorecombination matrix elements from the calculation on CO_2 performed in this chapter. The PAD obtained here are also compared to the experimental data of Rouzee *et al.* [126];
- The photoionization calculation from NO_2 in its equilibrium geometry are extended in chapter 7 to a dense grid of nuclear geometries, which is relevant for time resolved photoelectron spectroscopy and high harmonic spectroscopy calculations.

The CO₂ calculations were performed with the UKRmol package. The N₂ and NO₂ calculations were performed with the UKRmol+, with the latter using quadruple precision, allowing us to extend the range of photon energy up to 90eV.

As detailed in Chapter 5, there are three important steps for calculating the photoionization of molecules with the UKRmol/UKRmol+ package: the construction of molecular orbitals that ensure a good description of both continuum and bound wavefunctions, the construction of target state wave functions of sufficient quality, and finally the generation of the continuum orbitals and the continuum states. The procedures adopted in each of these steps are presented here.

6.1 Photoionization of N₂

Nitrogen is a key component of the Earth’s atmosphere and many plasmas. There are also several high quality experimental studies available [166, 167, 168] against which we can compare our results. In the ground neutral state N₂ has an internuclear distance of 2.048Å and a dominant electronic configuration given by

$$(1\sigma_g, 1\sigma_u)^4(2 - 3\sigma_g)^4(2\sigma_u)^2(1\pi_u)^4,$$

with the $(1\sigma_g, 1\sigma_u)$ orbitals being the molecular core. The valence space extends up to the $3\sigma_g, 3\sigma_u, 1\pi_u, 1\pi_g$ orbitals. N₂ has an ionization potential of 15.6eV[169], which is relatively high compared to other molecules.

6.1.1 Molecular orbitals and target states

We used a 6 – 311G** atomic basis and generated the molecular orbitals with a SA-CASSCF procedure using MOLPRO [170]. The ground neutral and the first 28 ionic states were included in the averaging. In the spirit of the Frozen Hartree Fock approximation, we used a weight of 100 on the neutral state.

The target model (model1) was obtained with a full valence CI calculation. The calculations were performed in the D_{2h} point symmetry group, the highest symmetry of the UKRmol codes for linear molecules. In Table 6.1 we show the vertical excitation energies for the first 2 ionic states. The energy of the ground ionic state was taken as reference.

Cationic states		
Model/Experiment	$A^2\Pi_u$	$B^2\Sigma_u^+$
model 1	1.93	3.25
Experiment [171]	1.50	3.17

Table 6.1: Vertical excitation energies (eV) for the first two excited states of N_2^+ . Values are given in relation to the first ionization potential of N_2 (15.6eV [169])

6.1.2 Inner and outer region

Since we are primarily interested in photon energies below 40eV, we used a Gaussian type continuum orbitals generated by the programs GTOBAS and NUMCBAS [107], spanning an energy range up to 90eV and with $l \leq 4$. The R-Matrix boundary (r_a) was set at 10 atomic units from the scattering center, and we included 250 target states in the close coupling expansion so we could accurately reproduce the polarization of the system.

At r_a the R-Matrix was matched to Coulomb functions. Propagating the R-Matrix to a larger radius only had an effect on the position and width of the autoionizing resonances of the molecule, which is beyond the scope of our calculations (see [172] for an accurate description of many autoionizing resonances of the N_2 molecule for several internuclear distances).

6.1.3 Partial photoionization cross sections and asymmetry parameters

In Fig.6.1 we show the partial photoionization cross sections and asymmetry parameters for the residual cation in the $X^2\Sigma_g^+$, $A^2\Pi$ and $B^2\Sigma_u^+$ state. The first ionization potential was set to 15.6eV [169]. We compare our results to the experimental data from Plummer *et. al.* [167], Marr *et. al.*[166] and Samson *et. al.* [168], and the theoretical work of Tashiro¹ [163]. We note that the partial photoionization cross section with the residual cation in the $X^2\Sigma_g^+$ ($A^2\Pi$) state obtained in our calculations slightly overestimates (underestimates) the experimental data, especially for photon energies above

¹In fact, Tashiro has also used the UKRmol package in his calculations, but his codes were never shared in the UKRmol repository

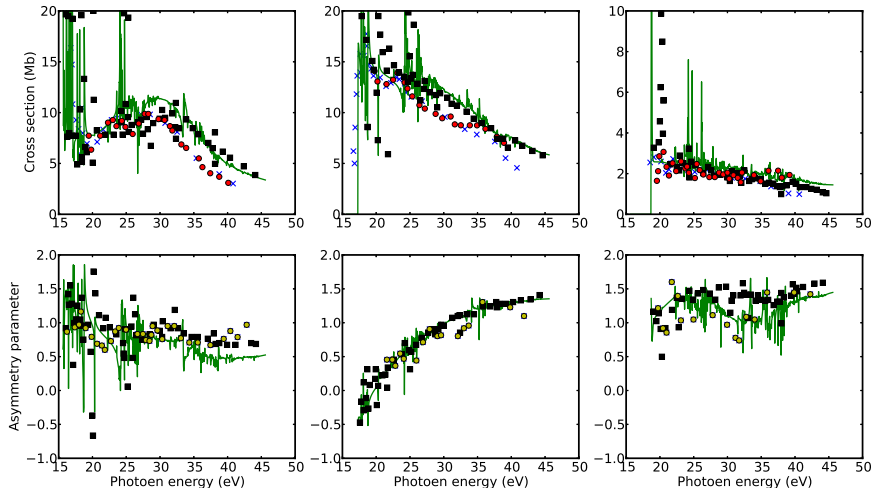


Figure 6.1: Partial photoionization cross sections and asymmetry parameters for the photoionization of ground state N_2 in the equilibrium geometry with the residual cation left in the $X^2\Sigma_g^+$ (first column), $A^2\Pi_u$ (second column) and $B^2\Sigma_u^+$ (third column) state. Green lines are the results obtained with our calculation. Black squares are the calculations of Tashiro [163], red circles are the experimental results from Plummer *et. al.* [167], yellow circles are the experiments of Marr *et. al.* [166] and the blue crosses are the experiments of Samson *et. al.* [168].

30eV. These differences could be either attributed to an inaccurate branching ratio used in the experiments, or a insufficient description of the channel coupling in our model in the energy range investigated.

Regarding the asymmetry parameters, we observe excellent agreement between our results and the experimental data. The asymmetry parameter for the $B^2\Sigma_u^+$ residual state obtained here, reproduce the experimental data better than the calculations of Tashiro.

In Fig.6.2 we compare our photoionization cross sections for the photoionization leaving the cation in the $X^2\Sigma_g^+$ and $A^2\Pi_u$ states, with the calculations using the Quante-mol software (the commercial branch of the UKRmol package), performed by Brigg *et. al.* [173]. In Quante-mol, the target models are simply obtained by a CI procedure using neutral Hartree Fock orbitals (generated by the SWSCF and SWFJK modules from the UKRmol pack-

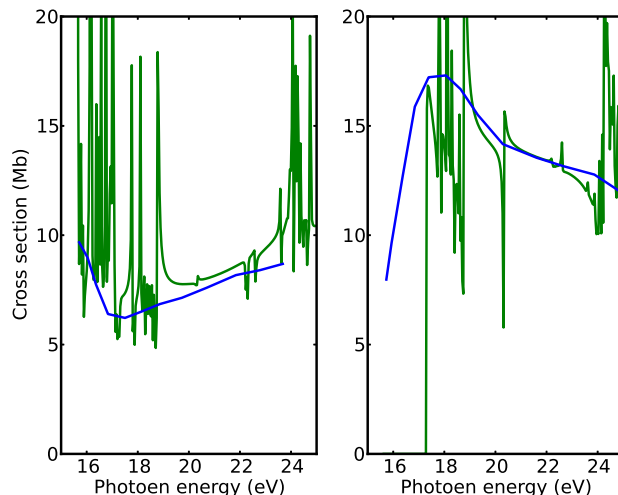


Figure 6.2: Partial photoionization cross sections and asymmetry parameters for the photoionization of ground state N_2 in the equilibrium geometry with the residual cation left in the $X^2\Sigma_g^+$ (left) and $A^2\Pi$ (right) state. Green lines are the results obtained with our calculation. Blue lines are the results of Brigg *et. al.*[173]

age). The difference between the target model employed here and in [173] justify the shift in the vertical excitation energy seen in Fig.6.2(right). Note also that in [173] the cross sections were smoothed with a Gaussian filter, in order to eliminate the autoionizing resonances. Overall, there is good agreement between both calculations, but it is clear that some details of the cross section are lost in [173] due to the gaussian smoothing and also to the low quality molecular orbitals used.

6.2 Photoionization of CO_2

Over the last decades an extensive list of experimental and theoretical works have investigated several different aspects of the electron-scattering and photoionization of the CO_2 molecule [174, 103, 175, 176, 177, 178, 179, 180, 181]. In the ground state, CO_2 is a linear molecule with a C-O bond distance of

Model	frozen orbs.	active space	CSFs
HF	$(1-2\sigma_g, 1\sigma_u)^6$	$(3-4\sigma_g, 2-3\sigma_u, 1\pi_u 1\pi_g)^{15}$	1
CI-1	$(1-2\sigma_g, 1\sigma_u)^6$	$(3-4\sigma_g, 2-3\sigma_u, 1\pi_u 1\pi_g)^{14}(5\sigma_g, 2\pi_u, 4\sigma_u)^1$ $(3-4\sigma_g, 2-3\sigma_u, 1\pi_u 1\pi_g)^{13}(5\sigma_g, 2\pi_u, 4\sigma_u)^2$	440
CI-2	$(1-2\sigma_g, 1\sigma_u)^6$	$(3-5\sigma_g, 2-3\sigma_u, 1-2\pi_u 1\pi_g)^{15}$	3692

Table 6.2: CI models used in the calculation of cationic electronic wavefunctions. In the last column, we indicate the maximum number of CSFs generated per irreducible representation and per spin.

2.19Å, and with a dominant electronic configuration given by

$$(1-2\sigma_g, 1\sigma_u)^6(3-4\sigma_g)^4(2-3\sigma_u)^4(1\pi_u)^4(1\pi_g)^4,$$

with the $(1-2\sigma_g, 1\sigma_u)$ being the core orbitals, and the valence space of the molecule extending up to the $5\sigma_g, 4\sigma_u, 2\pi_u, 1\pi_g$ orbitals.

6.2.1 Molecular orbitals and target models

A set of molecular orbitals was constructed from an initial Gaussian basis set (cc-pVTZ) [182] using a state averaged CASSCF [183, 184] procedure with the quantum chemistry package MOLPRO [170]. 21 states of the ion and the ground state of the neutral were included in the averaging. Choice of orbital set can have a strong influence on shape resonance features; in the spirit of the frozen core Hartree-Fock approximation, we chose the state averaging to be predominantly weighted towards the neutral with a small (10%) component of ionic states to improve the description of the target.

All target models have 6 electrons frozen in the core orbitals $(1-2\sigma_g, 1\sigma_u)$. The HF model represents the target states with a single configuration state function (CSF) and thus does not include electronic correlation in the ion. The CI-1 model includes single and double excitations into the valence orbitals not included in model 1. The CI-2 model consists of the full valence complete active space minus the $4\sigma_u$ orbital.

Table 6.3 shows the energies of the lowest 4 ionic states. The HF model gives generally poor agreement with experimental energies. Model 2, is significantly better, and model 3 agrees to within 0.2 eV.

Cationic states			
Model/Experiment	$A^2\Pi_u$	$B^2\Sigma_u^+$	$C^2\Sigma_g^+$
HF	4.70	5.33	7.14
CI-1	4.12	4.77	5.97
CI-2	3.97	4.45	5.77
Experiment [177]	3.8	4.3	5.6

Table 6.3: Vertical excitation energies (eV) for the first three CO_2^+ states.

6.2.2 Inner and outer region

Continuum orbitals with $l \leq 5$ and spanning an energy range from 0 to approximately 90eV were generated by optimizing a set of GTO to represent Coulomb functions. 3 virtual orbitals were included in each symmetry to improve the description of inner region polarization. Single channel calculations were performed using the model 1 description of the ion and multichannel calculations with models 2 and 3. With model 2 and 3 we included 96 states in the close coupling expansion. The lowest inner region wavefunction of the appropriate symmetry was used as the ground state of the neutral.

We matched to Coulomb functions at the R-matrix boundary: for molecules, such as CO_2 , with no permanent dipole, this approximation works well, at least at the level of the background cross section and shape resonances, and offers significant computational saving when there are many channels. Narrow resonance features however, are sensitive to channel coupling in the outer region and we would not expect to get good positions and widths without outer region propagation.

6.2.3 Partial photoionization cross sections

Fig. (6.3) shows orientationally averaged partial cross sections leaving the ion in the ground and first three excited states. The first feature to note is the presence of a high number of narrow resonance features in the R-matrix cross sections, these are autoionizing resonances associated with the various excitation thresholds included in the models. The single channel cross sections, with no excitation, are smooth. The experimental results we compare to here are of insufficient resolution to resolve the resonances, and the accurate characterization of such resonances, traditionally a strength of

R-matrix approaches, has been left for future work. In this work we concern ourselves with the background cross sections and broader shape resonance features.

The agreement with experiment and previous theory is excellent, with the CI models (2 and 3) generally in better agreement, up to 45 eV, than model 1. Above 45 eV the CI models display some unphysical pseudoresonances related to the omission of highly excited states in the close coupling expansion that are implicitly included in the L^2 configurations. The HF model gives slightly worse resonance positions compared to the previous work [103] (labelled Lucchese: 1 chan in the figures) at a similar level of approximation performed using the Schwinger variational approach. This difference is primarily due to the choice of orbitals (neutral HF vs state averaged CASSCF over both neutral and ionic states); our orbital choice includes some degree of orbital relaxation which tends to shift resonance positions to higher energy. Another difference is in the choice of gauge, our work uses the length gauge, as opposed to a mixed gauge approach in the previous theoretical work.

Previous theoretical work found a high, narrow shape resonance in the C channel at around 42 eV, approximately 5 eV above the IP of the ion, that was not evident in experimental cross sections. Various attempts to reconcile theory and experiment were made at the time, including vibrational averaging [175], and the inclusion of channel coupling and initial state correlation [174, 103], with partial success. It was speculated that the discrepancy was due to the need for correlation in the ion and many more excited states of the ion to be included in the channel coupling. Models CI-1 and CI-2 include both these and give very good agreement to experiment. In Fig (6.4) we see that the number of ionic channels plays a strong role in suppression of the resonance. With 64 states included the resonance is somewhat lowered in amplitude and significantly shifted in position, going to 96 states only has a small effect on position, but a dramatic effect on resonance height, which we attribute to loss of flux into highly excited ionic states.

Finally we note that cross sections near to and beyond the IP of the ion must be treated with some caution; for reliable treatment of the intermediate energy range (from close to the ionization threshold of the target up to several times this threshold), it has been found to be important in the accurate calculation of scattering and photoionization observables to account for highly excited electronic states of the target and the target continuum that are not included in the standard close-coupling approach. An approach that has found a great deal of success in atomic photoionization and scat-

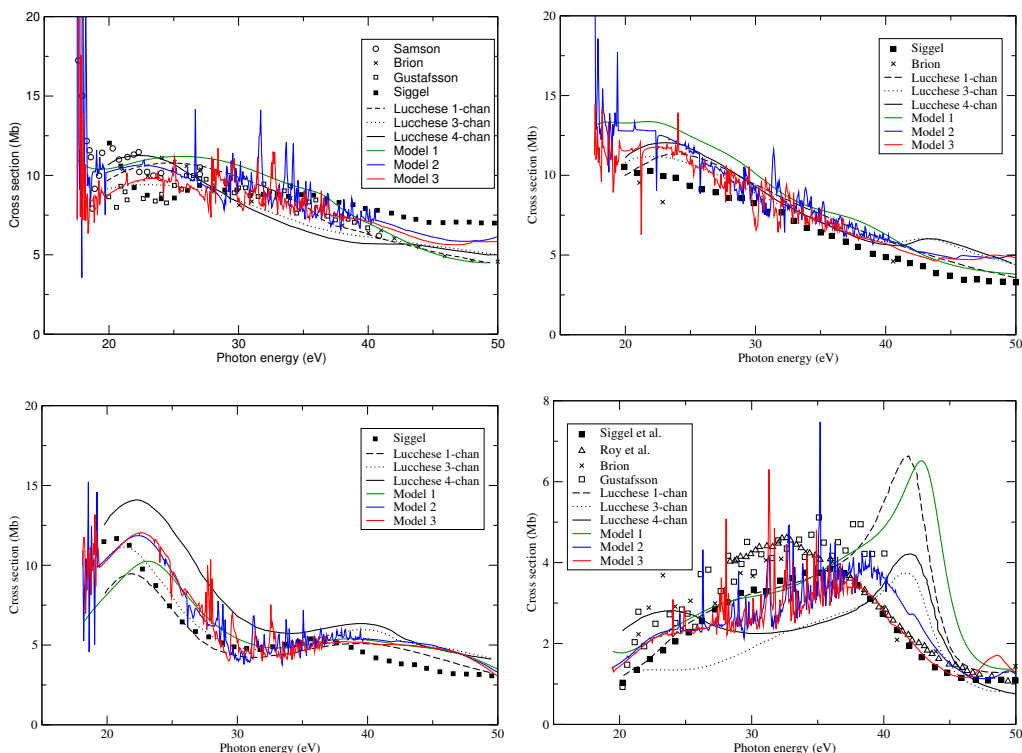


Figure 6.3: Partial photoionization cross sections of CO_2 : Top left, final ion state $X^2\Pi_g$. Top right, $A^2\Pi_u$. Bottom left, $B^2\Sigma_u^+$. Bottom right, $C^2\Sigma_g^+$. Experimental results: Samson et al. [178], Gustafsson et al. [179], Siggel et al. [180], Brion and Tan [181] and Roy et al. [176]. Previous theoretical results, Lucchese et al. [103]

tering calculations and is beginning to be applied to the molecular case is the R-matrix with pseudostates method (RMPS) [185]. As well as a rigorous treatment of the intermediate energy regime, RMPS has the benefit of converging the polarizability of the ion, which can have a strong effect on resonance position.

6.2.4 Photoelectron angular distributions

Two common experimental alignment distributions are: aligned with with the photon polarization and planar delocalized perpendicular (anti-aligned) to the photon polarization. These arise in the impulsive laser alignment of

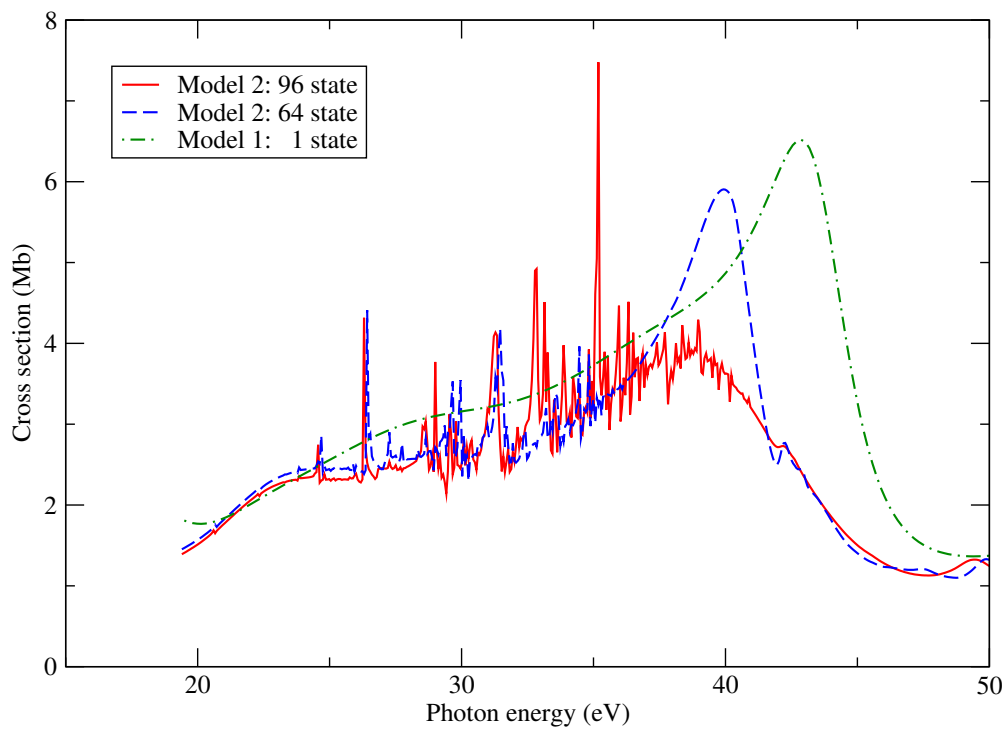


Figure 6.4: Partial photoionization cross sections of CO_2 : Final ion state $\text{C}^2\Sigma_g^+$. Comparison of models with different number of ionic states included.

molecules, where a rotational wavepacket is produced that cycles between alignment, anti-alignment and random alignment [186, 187, 188, 122, 189]. In this section we present photo-electron angular distributions (PAD) for these two scenarios.

Figures 6.5 and 6.6 show the $p_z - p_x$ emission plane for aligned and anti-aligned molecules respectively. The lab z -axis is defined by the (linearly polarized) photon polarization. In both these cases the cylindrical symmetry of the system is preserved leading to a cylindrically symmetric (around the z -axis) PAD. We therefore lose no information in looking at a 2D momentum cut.

We see that both aligned and anti-aligned results have rich angular structure, one useful method for the interpretation of angular distributions is to consider the angular momentum of the ejected photo-electron, the angular pattern in a particular energy region can be dominated by a particular partial wave, such as when there is a resonance in that partial wave, and interference between partial waves is a sensitive probe of the photoelectron-ion potential [117].

The ground state of the neutral has $^1\Sigma_g$ symmetry, for the aligned case the dipole operator has σ_u symmetry leading to final state symmetry of $^1\Sigma_u$. This leads to π_u , π_g , σ_g and σ_u symmetry of the continuum in the X, A, B and C channels respectively. For the anti-aligned case the dipole operator has π_u symmetry leading to final state symmetry of $^1\Pi_u$. This leads to a σ_u , σ_g , π_g and π_u , symmetry of the continuum in the X, A, B and C channels respectively. σ and π continua correspond to partial waves with $|m| = 0$ and $|m| = 1$ respectively. l is even or odd (gerade or ungerade) and a particular partial wave has $|m|$ longitudinal nodes $l - |m|$ latitudinal nodes. Taking the X channel in the aligned case as an example we can see that it is dominated by the $l = 3$ partial wave, with a smaller contribution from $l = 1$, between 20 and 30 eV. At higher energies, from 40 eV the $l = 5$ partial wave becomes dominant, we note that the maximum significant l value in the partial wave expansion can be estimated by $l_{max} = R_c p$ where R_c is a radius that characterises the size of the molecule and p is the photoelectron momentum, all in atomic units. By this estimation we would not expect to see significant contribution of $l = 6$ below 50 eV in photon energy, or $l = 7$ below 65 eV.

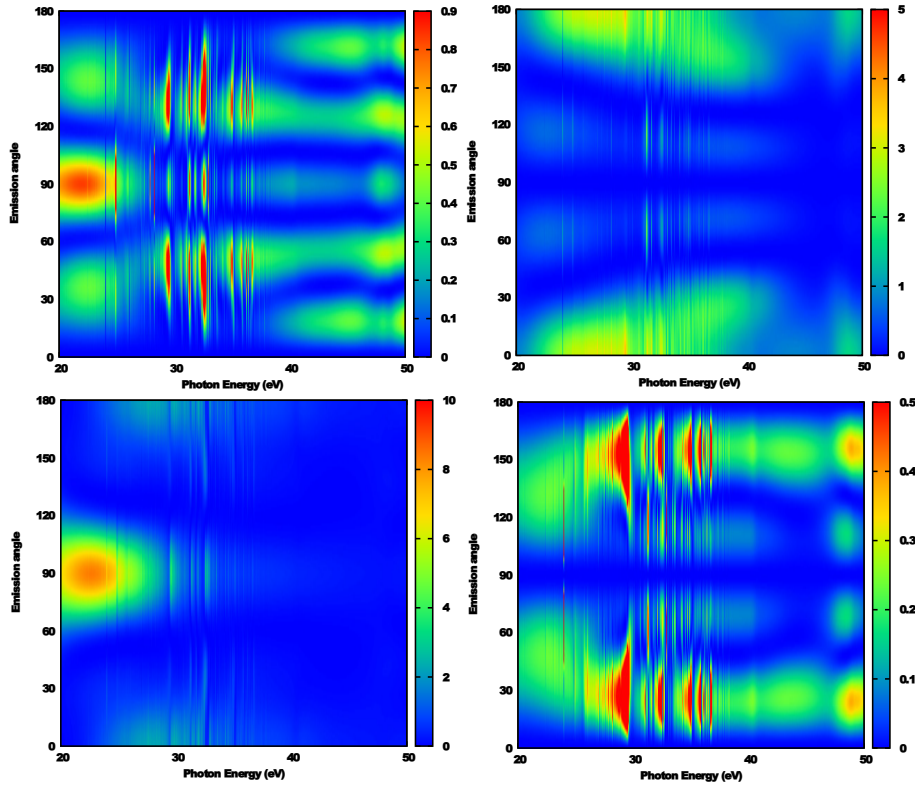


Figure 6.5: Aligned photoelectron angular distributions, the emission angle is defined relative to the lab frame photon polarization (which defines the lab z-axis), the magnitude has units Mb: Top left, $X^2\Pi_g$. Top right, $A^2\Pi_u$. Bottom left, $B^2\Sigma_u^+$. Bottom right, $C^2\Sigma_g^+$

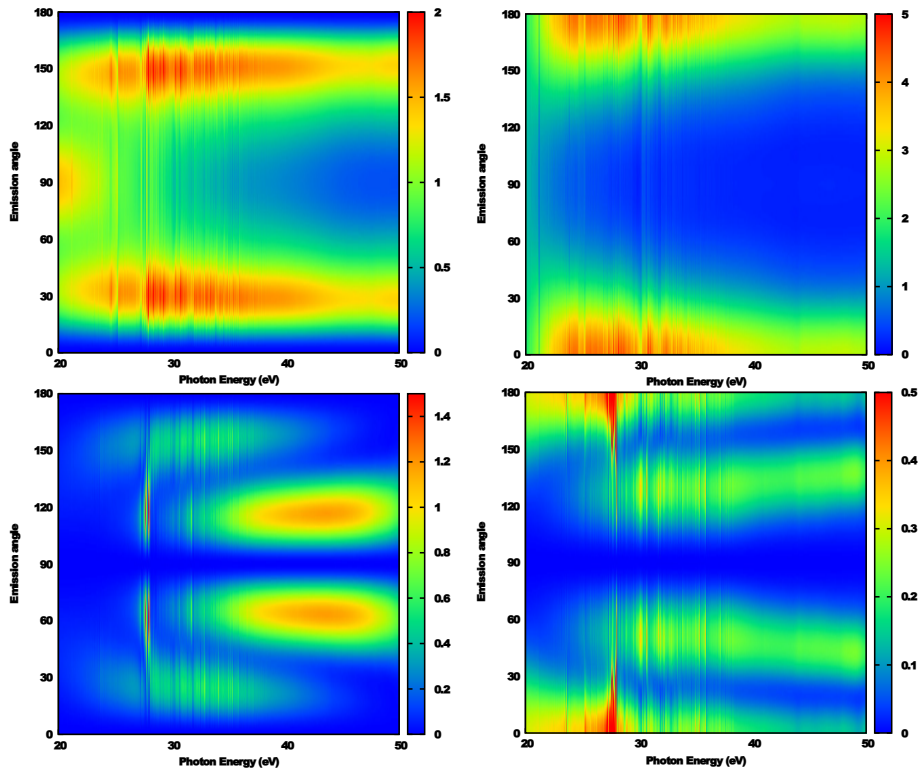


Figure 6.6: Anti-aligned photoelectron angular distributions, the emission angle is defined relative to the lab frame photon polarization (which defines the lab z-axis), the magnitude has units Mb: Top left, $X^2\Pi_g$. Top right, $A^2\Pi_u$. Bottom left, $B^2\Sigma_u^+$. Bottom right, $C^2\Sigma_g^+$

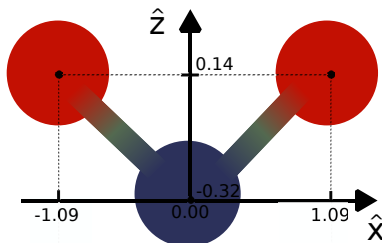


Figure 6.7: Geometry of NO_2 in its ground state. The molecule is placed in the \mathbf{zx} plane, thus B_1 and B_2 irreducible representations are swapped in relation to the usual ordering found in the literature.

6.3 Photoionization of NO_2

NO_2 (Fig.1) is an open shell molecule with the ground state electronic configuration

$$(1 - 2a_1, b_1)^6(3a_1)^2(2b_1)^2(4a_1)^2(3b_1)^2(1b_2)^2(5a_1)^2(1a_2)^2(4b_1)^2(6a_1)^1,$$

where $(1 - 2a_1, b_1)$ are core orbitals. NO_2 has a conical intersection between the ground 2A_1 and the first excited 2B_1 states at a bending angle $\angle ONO \approx 107^\circ$, making it a prototype system for investigating non-adiabatic dynamics. The photodynamics of the NO_2 molecule has been extensively explored in the literature, including time-resolved studies [190]. The first experiments on the high harmonic spectroscopy of NO_2 [191, 192] have revealed an interesting response in the high harmonic signal related to wave packet dynamics at conical intersections. This holds the promise to visualize proposed strong field control schemes of such dynamics [193]. Successful current models [91, 194, 195, 196] of molecular HHG incorporate angle-resolved recombination dipoles taken from time independent photoionization codes, driving the need for high quality recombination matrix elements.

6.3.1 Molecular orbitals and target models

The molecular orbitals were generated in MOLPRO[170] with a state averaged complete active space self consistent field (SA-CASSCF) procedure, using a 6-311G** atomic GTO basis set [197], and a Hartree Fock calculation of the NO_2 ground state as an initial guess for the molecular orbital coefficients. The state averaging included the 32 lowest energy ionic states and

Target models	Active space	CSFs
HF	$(1 - 5a_1, 1 - 3b_1, 1b_2)^{18}(6a_1, 4b_1, 2b_2, 1a_2)^4$	1
CI-1	$(1 - 2a_1, 1b_1)^6 (4 - 6a_1, 3 - 4b_1, 1 - 2b_2, 1a_2)^{16}$	250
CI-2	$(1 - 3a_1, 1 - 2b_1)^{10}(4 - 6a_1, 3 - 5b_1, 1 - 2a_2, 1b_2)^{12}$ $(1 - 3a_1, 1 - 2b_1)^{10}(4 - 6a_1, 3 - 5b_1, 1 - 2a_2, 1b_2)^{11}(7a_1, 5b_1)^1$	855
CI-3	$(1 - 2a_1, 1b_1)^6 (3 - 7a_1, 2 - 5b_1, 1 - 2b_2, 1a_2)^{16}$	28352

Table 6.4: Target models used in the calculation of the molecular orbitals and cationic electronic wavefunctions respectively. In the last column, we indicate the maximum number of configuration state functions (CSFs) generated for a single symmetry.

the ground state of the neutral, the latter having a weight of 30% in order to generate optimum molecular orbitals for both ionic and the neutral ground state.

Target wavefunctions were constructed using three different CI and a Hartree-Fock model. This allowed us to investigate the role of correlation in photoionization. As one of our future goals is to investigate HHG in the vicinity of the aforementioned conical intersection, requiring the calculation to be repeated for many geometries, we endeavored to find a minimal CI model that gave comparative results to our converged most sophisticated model. CI-3 uses the full valence space of orbitals in the active space, and leads to very large inner region Hamiltonians. CI-1 uses the same active space as used in the SA-CASSCF procedure, and in CI-2 we froze four extra electrons in the two lowest energy valence orbitals, which are energetically well separated from the rest, and added single excitations from the CI-1 active space to the orbitals $(7a_1, 5b_1)$.

6.3.2 Inner and region

In the photoionization calculation, the R-Matrix radius was set to $10 a_0$; a set of GTOs optimized to represent Coulomb functions spanning an energy range up to 90 eV and with $l \leq 6$ was used [107]. The radial wave functions derived from the R-Matrix were matched with Coulomb functions on the R-Matrix boundary. Propagating in the outer region and matching at a larger radius confirmed the convergence of the results [201, 106].

Two types of L^2 configurations were included in expansion (5.3): (i) those in which the N-th electron enters the active space; (ii) those in which the

Cationic states					
Model/Experiment	$(1)^3B_1$	$(1)^3A_2$	$(1)^1A_2$	$(1)^1B_1$	$(2)^3B_1$
HF	0.93	0.16	0.48	4.95	4.66
CI-1	1.82	2.34	2.56	3.28	4.86
CI-2	1.80	2.34	2.57	3.41	4.99
CI-3	1.91	2.45	2.81	3.42	5.02
Experiment [198]	1.78	2.37	2.83	3.28	
Experiment [199]	1.86	2.49	2.93	3.40	
CASPT2 [200]	1.81	2.48	2.92	3.27	4.86

Table 6.5: Vertical excitation energies (in electron volts) for the five lowest states of NO_2^+ and the target models used in this work.

continuum electron occupies one of 16 virtual orbital (chosen in energy order) (see [106] for more details on L^2 functions). The inclusion of a large number of target states was necessary to converge the close coupling expansion and to ameliorate unphysical pseudoresonances at higher energies related to target states left out of the expansion. All calculations were carried out with a total of 80 target states. To facilitate comparison to experiment, in the HF model we set the ionization thresholds equal to the experimental values from Baltzer [199], in the CI models the experimental ground state ionization threshold was used.

6.3.3 Partial photoionization cross sections and asymmetry parameters

In the calculations presented in this chapter the initial state is the ground state of the neutral molecule. We also have removed the sharp and narrow resonant features from the results obtained with the CI models by smoothing the partial wave dipoles with a Gaussian of width 1.36 eV for the purpose of easier comparison between the different models.

In Fig.6.8 we show the partial photoionization cross sections, σ_{fj} , for the six cationic states and for all CI models shown in Table 6.4. Shape resonances are observed for all the studied partial photoionization cross sections: around 17 eV and 26eV for the $(1)^1A_1$ and $(1)^1B_1$ cationic state, close to the ionization potential and at 25eV for the $(1)^3B_1$ cation, around 24eV for both

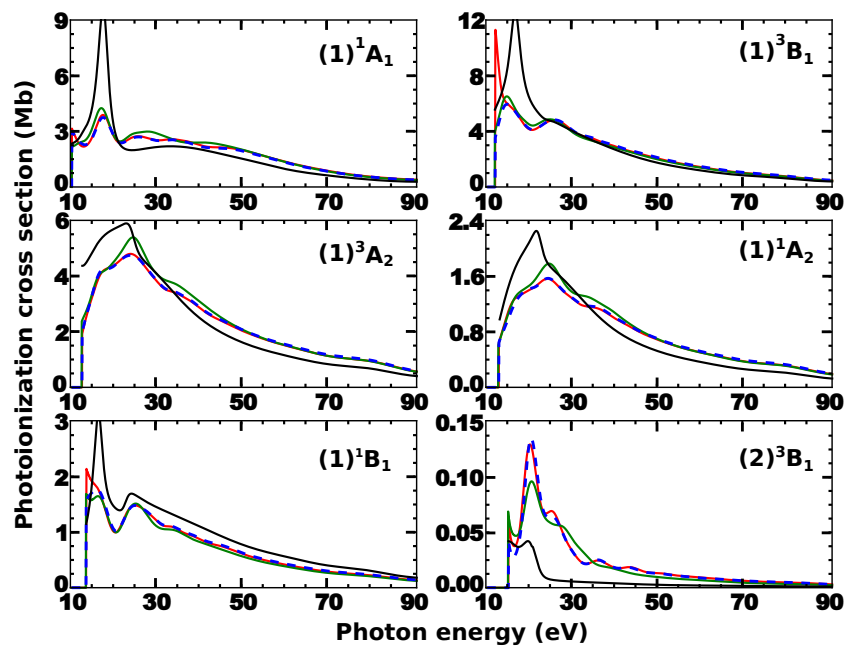


Figure 6.8: Partial photoionization cross sections for the 6 lowest energetic cationic states for the HF(black), CI-1(green), CI-2(red) and CI-3(dashed blue) calculations.

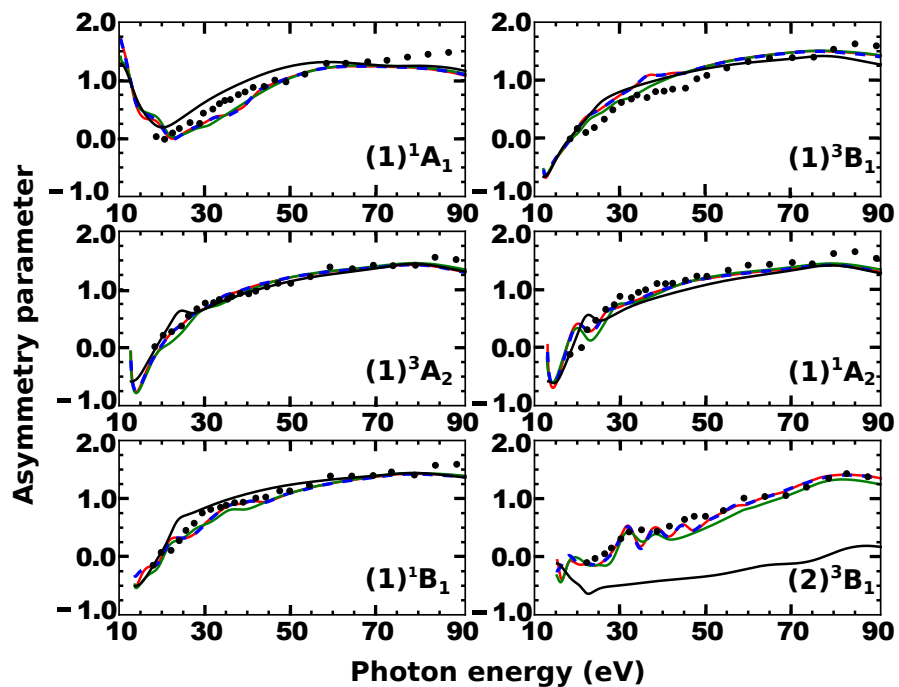


Figure 6.9: Asymmetry parameter for the 6 lowest energetic cationic states for the HF(black), CI-1(green), CI-2(red) and CI-3(dashed blue) calculations. Dots are the experimental results from Baltzer *et al.* [199].

(1)³A₂ and (1)¹A₂ cationic states, and finally at 20eV for the (2)³B₁ state. There is only a qualitative agreement between the shape resonances obtained with the HF and the CI models. In general, we observe that the HF models tend to overestimate the partial photoionization cross sections in relation to the CI-models, especially in the low energy shape resonance region for the ¹A₁, ³B₁ and ¹B₁ final cationic states. This can be explained by the loss of probability flux into the excited states of the target, an effect not included on a HF level.

We can see that the partial cross section for the (2)³B₁ state is much smaller than the other cross sections. (2)³B₁ is a satellite state of 2-hole 1-particle type and therefore electron correlation is necessarily involved in the photoionization leaving the residual ion in this state. This explains why the partial cross section for the (2)³B₁ state is much smaller compared to those of 1-hole type cationic states. The importance of correlation for this partial cross section is clearly revealed comparing the results obtained on the HF level (no correlation included) with the results obtained on the CI levels: the only significant enhancement of the HF cross section comes from the shape resonance around 20 eV.

In Fig.6.9 we compare the asymmetry parameter from equation (4.26) obtained here with the experimental data of Baltzer *et al.* [199] for all cationic states studied. We observe excellent agreement between all models and the experimental data, the exception being the HF model for the photoionization leaving the cation in (2)³B₁ state, indicating once again the importance of correlation/polarization for the accurate description of angular distributions for this state.

Analyzing Fig.6.8 and Fig.6.9, we conclude that CI-2 is the minimal model capable of reproducing all features observed with the robust CI-3 model for the cationic states considered here.

6.3.4 Photoionization dipoles

Finally, we investigate the photoionization dipoles relevant in HHG experiments. Since the ionization with NO₂ with a strong infrared field is most probable in the plane of the molecule (see Supplementary material of Ref. [191]), we present a 2D cut of the dipole in that plane. Analysis of the angular behavior of the dipoles shows (in a partial wave basis) that since the azimuthal dependency of the A₂ irreducible representation is always proportional to sin $m\phi$ with m being odd, the photoionization dipoles for cationic

states belonging to A_2 has nodal planes in \mathbf{zx} and \mathbf{zy} , thus, moreover, the $(1)^1B_1$ and $(2)^3B_1$ have a very high vertical ionization potential indicating that they play a negligible role in HHG. Consequently, we will consider here the photoionization dipoles only for the $(1)^1A_1$ and $(1)^3B_1$ cationic states.

In Fig.6.10 we show the photoionization dipoles, both phase and amplitude, for parallel S_{\parallel} and perpendicular S_{\perp} HHG light obtained:

$$S_{\parallel} = d_z(\theta, \mathbf{k}_f) \sin(\theta) + d_x(\theta, \mathbf{k}_f) \cos(\theta), \quad (6.1)$$

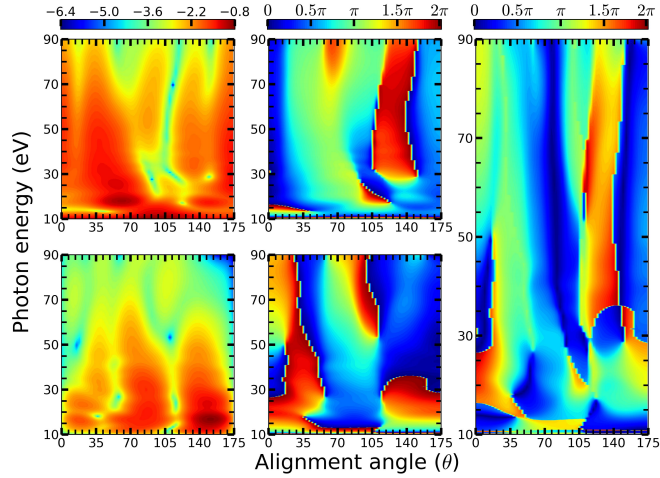
$$S_{\perp} = d_z(\theta, \mathbf{k}_f) \cos(\theta) - d_x(\theta, \mathbf{k}_f) \sin(\theta), \quad (6.2)$$

where $d_y(\theta, \mathbf{k}_f)$ and $d_z(\theta, \mathbf{k}_f)$ are the y and z components of the photoionization dipoles from equation (1), obtained from the fully converged photoionization calculations. On the horizontal axis of Fig.4 we show the angle θ between the z-axis (see Fig.1) of the molecular frame and the polarization direction of the infrared laser field, driving HHG. We note that for both parallel and perpendicular light there are amplitude maxima coinciding with the position of the shape resonances for the A_1 (at 17 eV and 25 eV) and B_1 (at 15 eV and 27 eV) states. The third column in Fig. 4 shows the relative phase between the parallel and perpendicular light

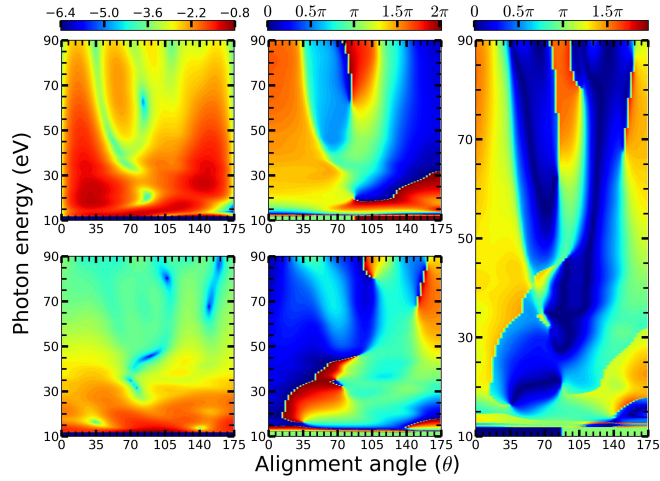
$$\Delta\phi = \arg(S_{\parallel}) - \arg(S_{\perp}), \quad (6.3)$$

which is important for the determination of the polarization state of HHG light.

Since the angular dependence of strong field ionization (see Supplementary material of [191]) favours electron ejection at small angles around 0° to 40° for the state and large angles around 135° for the state, the interference of these two channels in the emitted light could allow one to study the interplay of the two shape resonances that appear in these two channels at different angles. The large, but smooth variation of the phase around 35° for the state in the range of photon energies from 15 to 40 eV reflects recombination delays, associated with the presence of the shape resonance. For this state one may expect the emission of elliptically polarized light associated with the presence of the shape resonance around 10° and 40° , leading to strong signal in both parallel and perpendicular light in the energy region from 10 to 30 eV. The relative phase between the parallel and perpendicular light for this case varies from 0.5π to 1.5π .



(a)



(b)

Figure 6.10: Expected properties of HHG light, based on the analysis of recombination dipoles for the $(1)^1A_1$ (a) and the $(1)^3B_1$ (b) final cationic states and ionization from the ground state of the neutral molecule. First row shows the amplitudes (log scale) and the phase of parallel HHG light, the second row shows the amplitude (log scale) and the phase of perpendicular HHG light; the third column shows the relative phase between the two.

6.4 Discussion

We have shown the new ability of the current UKRmol to perform large photoionization calculations using a multiconfigurational description of the bound and scattering wavefunction of the system. We benchmarked the UKRmol and UKRmol+ codes, by comparing the results obtained here with several experiments and/or theoretical methods for the photoionization of N_2 , CO_2 and NO_2 . Additionally, the UKRmol+ codes allow us to compute the integrals in quadruple precision, extending the calculations to photon energies up to 90eV. Analysis of these calculations has allowed us to develop accurate moderate-sized models that open a number of opportunities in photoelectron (see chapter 7) and high harmonic spectroscopy (see chapter 9).

We demonstrated that high quality multichannel photoionization calculations with correlation effects included both in the neutral and the residual cationic states, are important for describing the photoionization from CO_2 and NO_2 molecules leaving the residual ion in certain excited state. In the case of photoionization from CO_2 , we have shown that for the photoionization leaving the ion in the $C^2\Sigma_g^+$ state, the amplitude of the shape resonance $\approx 40\text{eV}$ is heavily overestimated by single channel calculations. Indeed, for this specific shape resonance, we show that for obtaining a better comparison between theory and the experiments, as many as 96 states must be included in the close coupling expansion. In the calculations of photoionization from the ground state of NO_2 , we have shown the importance of using multiconfigurational methods for describing the partial photoionization cross section and asymmetry parameter in case the residual ion is a satellite state with respect to the initial molecular state. In this situation, all the contribution to the emission comes from non-dominant CSFs that are completely neglected in calculations where the cation is represented by a single Slater determinant.

Chapter 7

Photoionization of NO_2 for a range of nuclear geometries for time-resolved photoelectron spectroscopy

Understanding the photochemical reactions is a challenging task, since usually a large number of excited molecular states take part in the reaction, and often several intra-molecular radiationless processes e.g., internal conversion, isomerization, proton or electron transfer, etc [202, 203, 204], redistribute the charge and vibrational energy of the system. There are currently many experimental techniques for probing the reaction paths such as laser induced fluorescence [205] and resonant multiphoton ionization [206, 207], which are generally restricted to a specific region of the reaction coordinates. On the other hand, time-resolved photoelectron spectroscopy (TR-PES) stands out from other methods, due to the large amount of information imprinted in the photoelectron [34, 123, 124, 125] and its capability of probing a large region of the reaction coordinates.

In TR-PES an XUV/IR pump laser pulse initiates the reaction, creating a wavepacket that consists of a coherent superposition of molecular eigenstates constrained by the bandwidth of the pulse. The wavepacket starts then to explore the energetically accessible potential energy surfaces, and is photoionized (or probed) by an XUV/IR femtosecond laser pulse after a certain time t_p , normally ranging from tens of femtoseconds to a few picoseconds. By varying the delay between pump-probe laser pulses, the photoelectron is

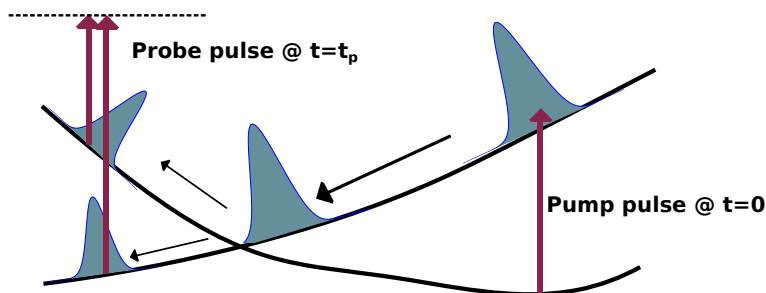


Figure 7.1: Scheme of a pump-probe experiment.

then used for tracking the path followed by the wavepacket along the several relevant potential energy surfaces.

In this work, we do not calculate the full wavepacket, but concentrate exclusively on the photoionization step (or probe) in TR-PES. The state of the art theoretical methods for calculating the photoionization of molecules relies on a high quality CI-type description of the bound molecular states [208, 209], but a single Slater determinant description of the residual ionic states. Therefore, these calculations struggle for computing the probe photoionization step in TR-PES involving highly excited ionic states [102] and ionic states that go through a conical intersection or an avoided crossing [210].

We address this limitation here by performing high quality calculations including correlation effects on both ground and ionic states of molecules using the multichannel R-Matrix method. The calculations are performed with the UKRmol+ package, which allow us to explore *ab initio* descriptions of several excited states of molecules over a large range of nuclear geometries using sophisticated quantum chemistry methods (CI, MCSCF, CASSCF, etc). We also have used the scripts developed by Houfek [211], which simplifies the inputs of the UKRmol+ and are adapted for easily performing calculations for a range of nuclear geometries. As a case study, we will investigate the photoionization of NO_2 molecules from the ground $((1)^2A')$ and the first excited $((2)^2A')$ neutral states, with the residual cationic states being $(1)^1A'$ and $(1)^3A'$. We are particularly interested in analyzing the reaction coordinates close to the conical intersection between $(1)^2A'$ and $(2)^2A'$ states, since in this region electronic correlation is important for both neutral and the $(1)^1A'$ ionic states [212].

This chapter is organized as follows: in section 7.1 we present the limi-

tations of the Born Oppenheimer approximation, and define key concepts in TR-PES such as non-adiabatic couplings, conical intersections and avoided crossings. In section 7.2, we present the details of the calculations. We also report in section 7.2 the orientationally averaged results and the PADs for the photoionization of the NO_2 molecule in a range of nuclear geometries. Finally in section 7.3, we present the conclusions and future work for the calculations presented in this chapter.

7.1 The Born Oppenheimer approximation and beyond

The properties of a molecular systems are found by solving the time-independent Schrödinger equation

$$\mathbf{H}^N(\mathbf{x}, \mathbf{R})\Psi^N(\mathbf{x}, \mathbf{R}) = E\Psi^N(\mathbf{x}, \mathbf{R}), \quad (7.1)$$

where E is the total energy of the system, $\mathbf{x} = (\mathbf{x}_1, \dots, \mathbf{x}_N)$ is the electron space-spin coordinate, $\mathbf{R} = (\mathbf{R}_1, \dots, \mathbf{R}_n)$ is the spatial coordinates of the nuclei, and \mathbf{H}^N is the molecular Hamiltonian given by

$$\mathbf{H}^N(\mathbf{x}, \mathbf{R}) = \mathbf{T}_n(\mathbf{R}) + \mathbf{H}_{el}(\mathbf{x}, \mathbf{R}), \quad (7.2)$$

with \mathbf{T}^n being the nuclear kinetic energy operator. \mathbf{H}_{el} is the electronic Hamiltonian defined by the eigenvalue equation

$$\mathbf{H}_{el}(\mathbf{x}; \mathbf{R})\Phi_i^{(N)}(\mathbf{x}; \mathbf{R}) = E_{el,i}(\mathbf{R})\Phi_i^{(N)}(\mathbf{x}; \mathbf{R}), \quad (7.3)$$

where $\Phi_i^{(N)}$ and $E_{el,i}$ are respectively the electronic wavefunctions and the adiabatic potential energy surface of the i^{th} electronic state. The semicolon in the argument indicates that the dependency on the nuclear coordinates is only parametric.

Expanding the solutions of Eq.7.1 in the basis of the electronic states $\Phi_i^{(N)}$

$$\Psi_k^N(\mathbf{x}; \mathbf{R}) = \sum_i \xi_i(\mathbf{R})\Phi_i^N(\mathbf{x}; \mathbf{R}), \quad (7.4)$$

with $|\xi\rangle$ being the nuclear wavefunction, we obtain the eigenvalue equation for ξ

$$[T_n(\mathbf{R}) + V_i - \sum_{j\alpha} \Gamma_{ij\alpha}] \xi_i(\mathbf{R}) = E_{\xi_i} \xi_i(\mathbf{R}) \quad (7.5)$$

where $\Gamma_{ij\alpha}$ is the non-adiabatic coupling given by

$$\Gamma_{ij}(\mathbf{R}) = \frac{G_{ij} + 2\mathbf{F}_{ij} \cdot \nabla}{2M_\alpha} \quad (7.6)$$

with M_α being the mass of the nuclei α , $G_{ij} = \langle \Phi_i | \nabla_{R_\alpha}^2 | \Phi_j \rangle$ and $\mathbf{F}_{ij} = \langle \Phi_i | \nabla_{R_\alpha} | \Phi_j \rangle$. Using the Hellmann Feynman theorem [213]

$$\mathbf{F}_{ij} = \frac{\langle \Phi_i(\mathbf{r}; \mathbf{R}) | \nabla_{R_\alpha} \mathbf{H} | \Phi_j(\mathbf{r}; \mathbf{R}) \rangle}{V_i - V_j}. \quad (7.7)$$

Note that when the potential energy surfaces of the i^{th} and j^{th} electronic states are far from each other the non-adiabatic couplings are negligible. In this case, different electronic states are completely decoupled from each other and we can evoke the Born Oppenheimer approximation (or adiabatic approximation), which states that the wavefunction of the system is dictated by a single term in the expansion in Eq.7.4. On the other hand, when the potential energy surfaces of the electronic states are close to each other, the non-adiabatic couplings are strong, resulting in a coupling of the electronic states from the neighboring potential energy surfaces. In this situation, the diagonalization of the molecular Hamiltonian becomes challenging, since the non-adiabatic couplings actually diverge for electronic states that are degenerate. Thus, it is convenient to introduce an unitary transformation that diabaticizes the Hamiltonian, making the non-adiabatic couplings zero or at least finite.

7.1.1 Conical intersections and avoided crossings

Isolating two coupled potential energy surfaces, one can write the Hamiltonian in the diabatic picture in terms of a two-level system

$$\mathbf{H}_2 = \begin{bmatrix} H_{11} & H_{12} \\ H_{21} & H_{22} \end{bmatrix}. \quad (7.8)$$

with the diagonal terms being the diabatic potentials, and the non-diagonal terms are the non-adiabatic couplings between the two electronic states. One can go from the diabatic to the adiabatic picture, by diagonalizing \mathbf{H}_2

$$\mathbf{S}^\dagger \mathbf{H}_2 \mathbf{S}, \quad (7.9)$$

where \mathbf{S} is the unitary rotation matrix

$$S = \begin{bmatrix} \cos \alpha(\mathbf{R}) & \sin \alpha(\mathbf{R}) \\ -\sin \alpha(\mathbf{R}) & \cos \alpha(\mathbf{R}) \end{bmatrix}, \quad (7.10)$$

where

$$\alpha = \frac{1}{2} \arctan \left(\frac{2H_{12}}{H_{22} - H_{11}} \right) \quad (7.11)$$

The eigenvalues of \mathbf{H}_2 are then given by

$$E_{\pm} = \frac{1}{2} \left[H_{11} + H_{22} \pm \sqrt{(H_{11} - H_{22})^2 + 4H_{12}^2} \right], \quad (7.12)$$

Note that $E_+ = E_-$ if the following conditions are satisfied

$$H_{11} - H_{22} = 0, \quad (7.13)$$

$$H_{12} = 0, \quad (7.14)$$

For a molecule with N^{free} degrees of freedom, the conditions in Eq.7.13 and Eq.7.14 are only satisfied in a $N^{free} - 2$ subspace. Since diatomic molecules have a single degree of freedom, the conditions in Eq.7.13 and Eq.7.14 are never satisfied, resulting in the so called *non-crossing rule* for diatomic molecules. On the other hand, for molecules with more than two atoms, there is enough degrees of freedom for satisfying Eq.7.13 and Eq.7.14, thus the two electronic states can cross, resulting in a so called *conical intersection*.

7.2 Photoelectron spectroscopy with the R-Matrix method: case study of NO_2

NO_2 has 3 nuclear vibrational modes: symmetric stretching, where both $N-O$ bonds vary equally (Fig.7.2a); scissors, which accounts for variations of the $\gamma = \angle ONO$ angle (Fig.7.2b); and asymmetric stretching where the variations of the $N-O$ bonds vary equally but in opposite direction (Fig.7.2c). Here, we will fix the symmetric stretching at 1.25Å, and consider a 2D variation of the reaction coordinates corresponding to the scissors and asymmetric stretching modes. Consequently, the calculations performed in this chapter are carried

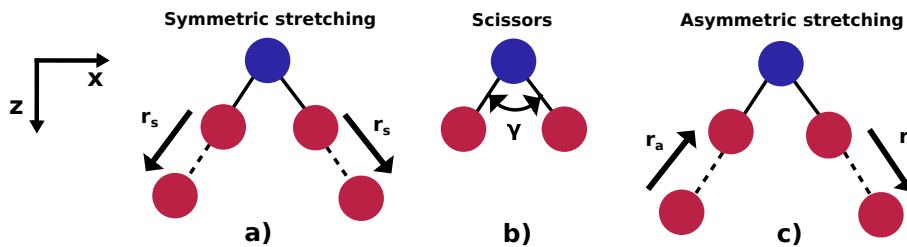


Figure 7.2: Vibrational modes of the NO_2 molecule.

in the C_s point symmetry group. We fix the molecule in the zx plane, thus, the A_1, B_1 (A_2, B_2) irreducible representations in C_{2v} map to A' (A'') in C_s . In C_s the ground electronic configuration of NO_2 in the equilibrium geometry is

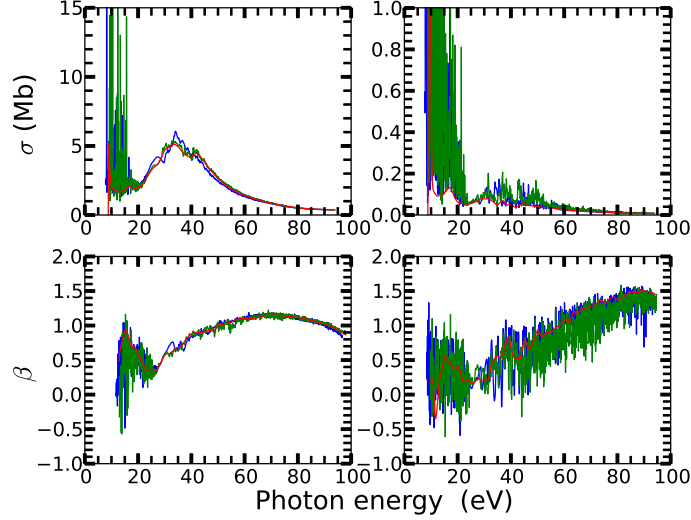
$$(1 - 3a')^6(4 - 7a')^8(1a'')^2(8a')^2(2a'')^2(9 - 10a')^3$$

with $1 - 3a'$ being the core orbitals, and the valence space extending up to the $11 - 12a'$ and $1 - 3a''$ orbitals. Moreover, the $(1)^2A'$ and $(2)^2A'$ neutral states form a conical intersection ($\gamma \approx 107^\circ$ for $r_a = 0$ and $r_s \approx 1.25\text{\AA}$), which has been extensively studied in the literature [212, 190].

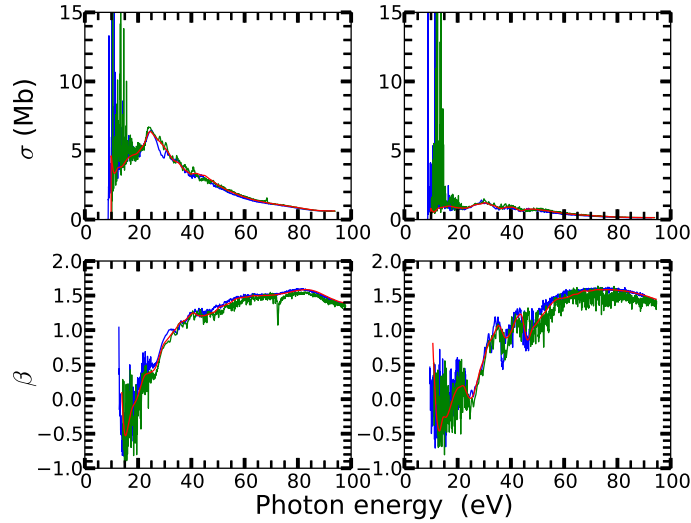
7.2.1 Molecular orbitals and target models

The molecular orbitals over the geometric grid are generated by a SA-MCSCF procedure with the active space consisting of the $6 - 12a'$ and $1 - 4a''$ orbitals from a set of 6-311G** atomic basis [197]. We included in the state averaging two cationic states per symmetry per spin, and the $(1)^2A', (2)^2A'$ neutral states of NO_2 . Both neutral states had a weight of 30%. An intuitive behavior of the molecular orbitals was observed in three distinct geometric arrangements:

- Linear limit: there is a localization of the electronic density in each of the atoms that favors dissociation of the molecule.
- Small bending angles: there is the formation of an $O-O$ bond, redistributing the electronic density more uniformly along the molecule, consequently, we observe that the molecular orbitals are spread along the $N-O$ and $O-O$ bounds, as well as in the center of mass of the molecule.

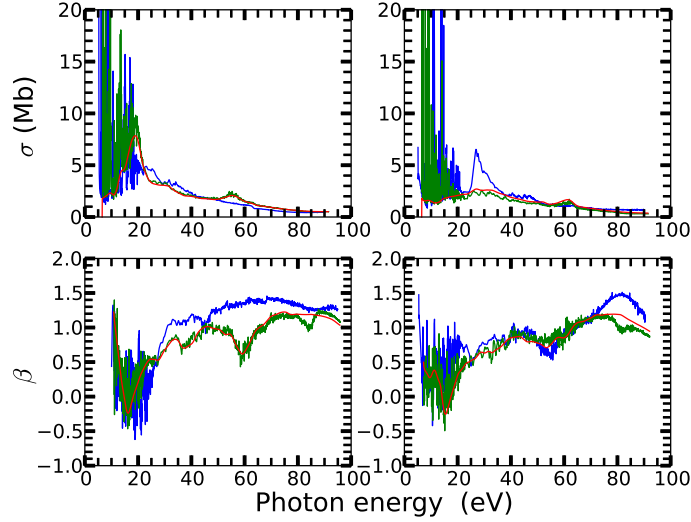


(a)

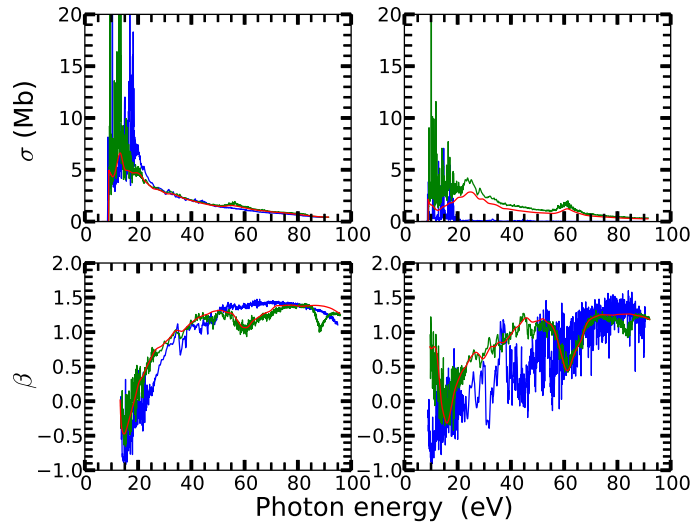


(b)

Figure 7.3: Partial photoionization cross sections (top) and asymmetry parameters (bottom), for photoionization from the $(1)^2A'$ (left) and $(2)^2A'$ (right) neutral states for $\gamma = 85^\circ$ and $r_a = 0.2\text{\AA}$. The residual ion is in the $(1)^1A'$ state in (a), and $(1)^3A'$ in (b). Blue, red and green curves correspond to the calculations using models CI-4, CI-5 and CI-6 respectively.



(a)



(b)

Figure 7.4: Partial photoionization cross sections (top) and asymmetry parameters (bottom), for photoionization from the $(1)^2A'$ (left) and $(2)^2A'$ (right) neutral states for $\gamma = 160^\circ$ and $r_a = 0\text{\AA}$. The residual ion is in the $(1)^1A'$ state in (a), and $(1)^3A'$ in (b). Blue, red and green curves correspond to the calculations using models CI-4, CI-5 and CI-6 respectively.

- Large asymmetric stretching: there is a larger overlap between the tight $N-O$ bond, while the more distant oxygen becomes more and more isolated.

In order to reduce the size of the photoionization calculations, we aimed to have a minimal target model capable of reproducing all main features of the potential energy surfaces of the ionic and neutral states. From the calculations at the equilibrium geometry in chapter 6, we have learned that:

- it is important to add the $2b_2$ orbital to the active space of the CASSCF procedure for obtaining a good ionization potential for the first six cationic states;
- excitations from the two lowest energetic valence orbitals ($4, 5a'$) do not play a significant role in the description of the ground and lowest excited states of the cation;

Motivated by these results and the model CI-2 from the equilibrium geometry calculation, we defined a reference space consisting of the $6 - 10a'$ and $1 - 3a''$ orbitals, and tested three different CI models that are shown in Table 7.1. We note that freezing the first $5a'$ orbitals allow us to increase the active space of the calculation without prohibitively increasing the number of CSFs being generated.

In Fig.7.5 we show the potential energy curves (PEC) from some of the NO_2^+ states for $r_a = 0\text{\AA}$ (left) and $r_a = 0.2\text{\AA}$ (right), obtained with model CI-4. In this chapter, we are particularly interested in investigating photoionization of NO_2 leaving the ion in the $(1)^1A'$ and $(1)^3A'$ states. In Fig.7.6 we compare the PEC from the $(1)^1A'$ and $(1)^3A'$ states obtained with model CI-4 against the calculations of Hirst [214]. A good agreement between both calculations is observed. The main features of the PEC from the $(1)^1A'$ and $(3)^1A'$ states are:

- the ground cationic states swaps from the $(1)^1A'$ to the $(1)^3A'$ state for $95^\circ \leq \gamma \leq 115^\circ$;
- there is a global minimum close to the linear limit, and a local minimum at 80° for the $(1)^1A'$ ionic state;
- the equilibrium geometry of the $(1)^3A'$ state is found at $\gamma = 118^\circ$, in good agreement with previous calculations ($\gamma = 120.9^\circ$ in [200])

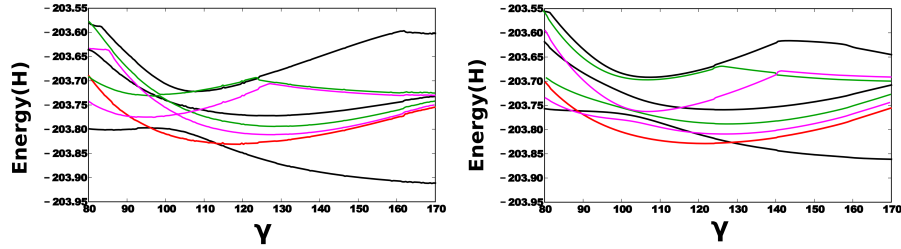


Figure 7.5: Potential energy curve for $r_a = 0$ (left) and $r_a = 0.2\text{\AA}$ (right) from the CI-4 model for the $^1A'$ (black), $^3A'$ (red), $^3A''$ (green) and $^1A''$ (pink) irreducible representations.

Target models	Active space	CSFs
CI-4	$(1 - 5a')^{10} (6 - 10a', 1 - 3a'')^{11}$	3219
	$(1 - 5a')^{10} (6 - 10a', 1 - 3a'')^{11} (11 - 14a')^1$	
CI-5	$(1 - 5a')^{10} (6 - 10a', 1 - 3a'')^{11}$	4731
	$(1 - 5a')^{10} (6 - 10a', 1 - 3a'')^{11} (11 - 15a', 4a'')^1$	
CI-6	$(1 - 5a')^{10} (6 - 10a', 1 - 3a'')^{11}$	5522
	$(1 - 5a')^{10} (6 - 10a', 1 - 3a'')^{11} (11 - 12a')^1$	
	$(1 - 5a')^{10} (6 - 10a', 1 - 3a'')^{11} (11 - 12a')^2$	

Table 7.1: Target models used in the photoionization calculation. In the last column, we indicate the maximum number of configuration state functions (CSFs) generated for a single irreducible representation.

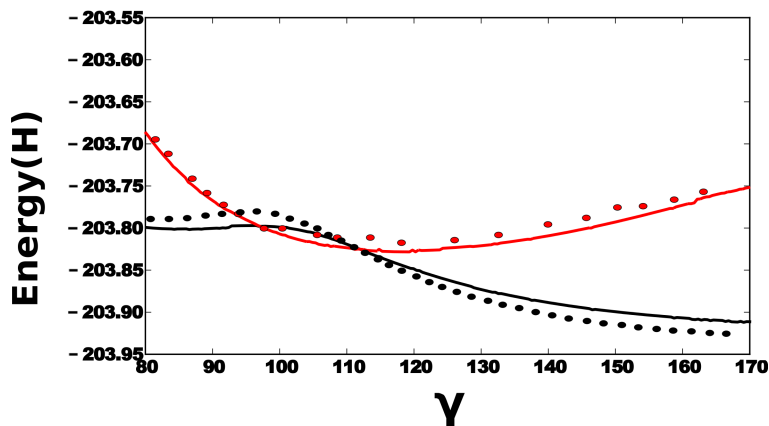


Figure 7.6: Potential energy curve for $r_a = 0$ for the $(1)^1A'$ (black) and $(1)^3A'$ (red). Solid lines are the results obtained with CI-4 model, dots are the calculations of [214]

7.2.2 Inner and outer region

The continuum orbitals were generated for $l \leq 6$ and spanned an energy range up to 90eV, which required the use of quadruple precision in computing the target and continuum integrals. Convergence for all models with respect to the number of states included in the close coupling expansion was achieved for calculations with 80 target states. Under these considerations, the calculation of a single geometry in the VULCAN cluster at MBI using 5 nodes took from 5 to 6 hours depending on the target CI model considered.

Due to computational limitations, we only performed convergence tests at the photoionization level for a few critical nuclear geometric configuration where electronic correlation plays a major rule: at the extremes of the angular grid ($r_a = 0\text{\AA}, \gamma = 160^\circ$) and ($r_a = 0.2\text{\AA}, \gamma = 80^\circ$), and close to the conical intersection ($r_a = 0.2\text{\AA}, \gamma = 105^\circ$).

As indicated in Fig.7.3 and Fig.7.4, there is good agreement for the asymmetry parameter and cross sections for photoionization leaving the ion in the $(1)^1A'$ and $(1)^3A'$ states, for all CI models considered here. Thus we choose the simplest target model (CI-4) for the photoionization calculations over the whole geometric grid.

We evaluate the quality of the neutral states calculated with the UKRmol+ codes, by plotting their PEC, using model CI-4, in Fig.7.7. We observe that our calculation successfully reproduces the expected features of the PEC,

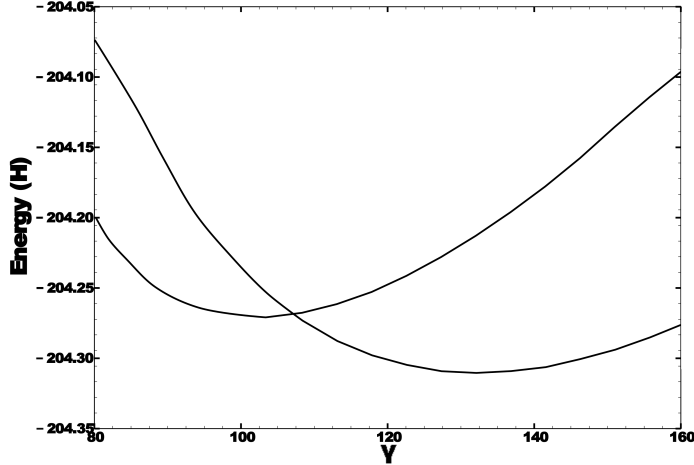


Figure 7.7: Potential energy curve of the neutral states obtained with model CI-4, and a grid with $\Delta\gamma = 4.5^\circ$.

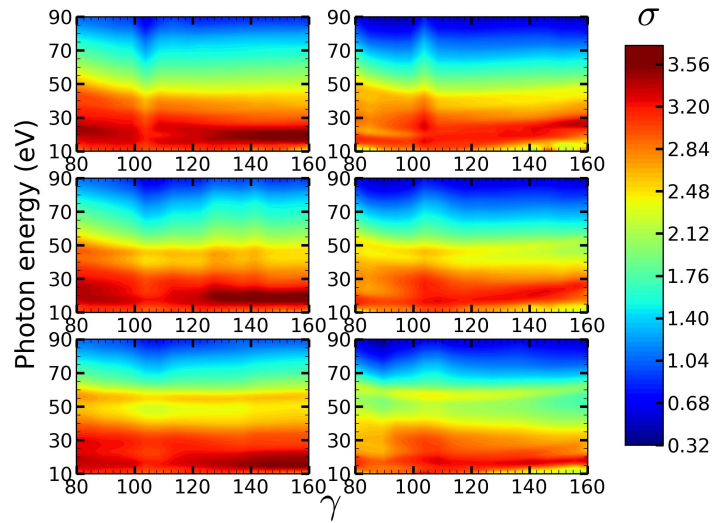
including the conical intersection, found here at $\gamma \approx 107.5^\circ$.

7.2.3 Total photoionization cross sections

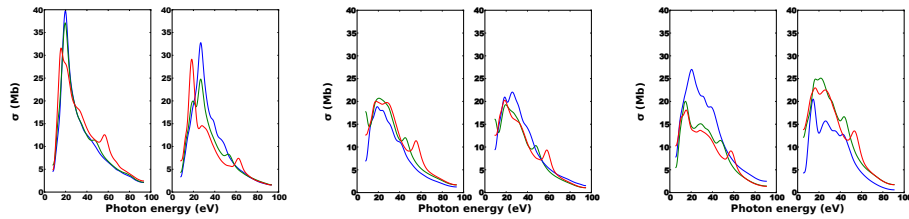
In Fig.7.8(a) we plot the total cross section for the photoionization from the $(1)^2A'$ and $(2)^2A'$ neutral states for $80^\circ \leq \gamma \leq 160^\circ$ and $r_a = 0\text{\AA}, 0.1\text{\AA}$ and 0.2\AA (see details of the plot in the caption). We notice in this plot a clear signature of the conical intersection, shown as a decrease (increase) of cross section amplitude for the photoionization from the $(1)^2A'$ ($(2)^2A'$) neutral state. A better understanding of the mechanisms involved in the variation of the cross section close to the conical intersection requires the resolution of the final ionic states after ionization.

In all plots we notice a broad peak with a width of ($\approx 5eV$) at approximately 25 eV for all γ . For both neutral states, the amplitude of this peak decreases as one approaches $\gamma = 105^\circ$. Additionally, we notice that the peak bifurcates into two peaks found at $\approx 20eV$ and $\approx 30eV$ for $\gamma < 105^\circ$, for the photoionization from the $(1)^2A'$ state.

Finally, we observe for all bending angles the emergence of a peak for $r_a \neq 0$, which is located at $\approx 60eV$ for $r_a = 0.4\text{\AA}$. This feature can be more clearly seen in Fig.7.8(b,c,d) where we plot cuts of the total cross sections



(a)



(b)

(c)

(d)

Figure 7.8: In (a) we show the total cross section (in Megabarns) for photoionization from the $(1)^2A'$ (left column) and $(2)^2A'$ (right column) neutral states for $80 \leq \gamma \leq 160^\circ$. in logscale. First row corresponds to $r_a = 0$, the second to $r_a = 0.1$ and the third to 0.2 . In b),c),d) we show cuts of the total cross section for photoionization from the $(1)^2A'$ (left column in the subplot) and $(2)^2A'$ (right column in the subplot) neutral states for $\gamma = 160$ (b), $\gamma = 115$ (c) and $\gamma = 80$ (d). Blue, green and red curves correspond respectively to $r_a = 0, 0.1$ and 0.2 \AA .

for the photoionization from the $(1)^2A'$ and $(2)^2A'$ neutral states for several values of r_a and γ .

7.2.4 Partial photoionization cross sections and asymmetry parameters

$(1)^1A'$ residual ionic state

In Fig.7.9(a) we show the cross sections for the photoionization from both neutral states leaving the ion in the $(1)^1A'$ state. The most striking feature is the sudden decrease (increase) of amplitude at $\gamma \approx 107^\circ$ for the photoionization from the $(1)^2A'$ ($(2)^2A'$) neutral state, the cross sections are roughly homogeneous for $80^\circ \leq \gamma \leq 160^\circ$. We also see in Fig.7.9(a) a resonance at high photon energies for $r_a \neq 0\text{\AA}$ for photoionization from both the $(1)^2A'$ and $(2)^2A'$ neutral states, which coincides with the peak at high photon energies for $r_a \neq 0\text{\AA}$ found in the total photoionization cross sections.

The behavior of the cross section can be understood by analyzing the dominant electronic configurations of the ionic and the neutral states. A satellite state is defined as a 2h-1p electronic configuration from a reference state. Since there is a difference of two spin-orbitals between the reference and the satellite state, this transition is forbidden due to the Slater rules for the dipole operator. Consequently, all signal observed in the cross section comes from non-dominant electronic configurations of the cation and the neutral.

Firstly we analyze the leading electronic configuration of the ionic and neutral states far from the conical intersection between the $(1)^2A'$ and $(2)^2A'$ neutral states.

- The $(1)^1A'$ ionic state has a leading configuration of $\dots(9a')^0(10a')^2$ for $\gamma < 100^\circ$ and $\dots(9a')^2(10a')^0$ for $\gamma > 115^\circ$. The changing of electronic configuration of the $(1)^1A'$ ionic state at $\gamma \approx 107^\circ$, is due to the proximity between the PEC of $(1)^1A'$ and $(2)^1A'$ ionic states shown in Fig.7.5(top left).
- The $(1)^2A'$ neutral state has a leading configuration of $\dots(9a')^1(10a')^2$ for $\gamma < 100^\circ$ and $\dots(9a')^2(10a')^1$ for $\gamma > 115^\circ$.
- The $(2)^2A'$ neutral state has a leading configuration of $\dots(9a')^2(10a')^1$ for $\gamma < 100^\circ$ and $\dots(9a')^1(10a')^2$ for $\gamma > 115^\circ$.

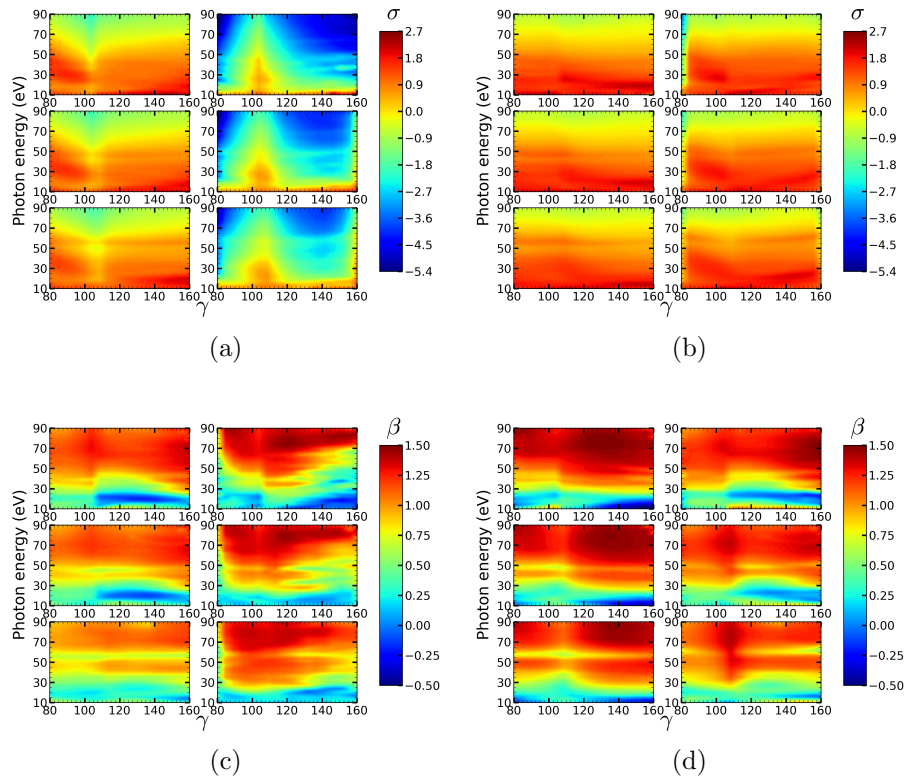


Figure 7.9: Partial photoionization cross sections (in Mega barns) in logscale (a,b) and asymmetry parameters (c,d) for $80^\circ \leq \gamma \leq 160^\circ$. In each subplot, the left column (right column) corresponds to the photoionization from the $(1)^2A'$ ($(2)^2A'$) neutral state. In each subplot, the first row corresponds to $r_a = 0$, the second to $r_a = 0.1\text{\AA}$ and the third to 0.2\AA .

Far from the conical intersection, the leading electronic configuration of the $(1)^1A'$ ionic state is always a 1h-1p in relation to the $(1)^2A'$ neutral state. Consequently, we observe a strong signal in Fig.7.9(a). On the other hand, the leading electronic configuration of the $(1)^1A'$ ion is a satellite state in relation to the $(2)^2A'$ neutral. In this case we observe a very low signal, coming essentially from low order electronic configurations of the $(1)^1A'$ and $(2)^2A'$ states.

There are two important factors to be noticed for $100^\circ \leq \gamma \leq 108^\circ$:

- For $\gamma \approx 100^\circ$, the $(1)^1A'$ ionic state is described by a strong mix between the $[\approx 0.7] \dots (9a')^0(10a')^2$ and $[\approx 0.5] \dots (9a')^2(10a')^0$ electronic configurations. The neutral states on the other hand are far enough from the conical intersection, that they can be described by single electronic configurations.
- For $\gamma \approx 107^\circ$, i.e., close to the conical intersection, the neutral states are described by a strong mix between $[\approx 0.7] \dots (9a')^1(10a')^2$ and $[\approx 0.7] \dots (9a')^2(10a')^1$ electronic configuration. On the other hand, the $(1)^1A'$ ionic state is described by the dominant $\dots(9a')^2(10a')^0$ electronic configuration.

Consequently, for $\gamma \approx 107^\circ$ the cross section for photoionization from both neutral states are very similar, as they are nearly degenerate. All signal observed comes from the $[\approx 0.7] \dots (9a')^2(10a')^1 \rightarrow \dots(9a')^2(10a')^0$ dipole transition.

Close to $\gamma \approx 100^\circ$, the dominant electronic configuration of the ion is a 2h-1p with respect to the neutral. On the other hand the second most dominant electronic configuration of the ion is a 1h-1p in respect with the $(1)^2A'$ neutral. Overall, we observe a decrease in the cross section as shown in Fig.7.9(a). For the photoionization from the $(2)^2A'$ state, the dominant electronic configuration of the ion is a 1h-1p with respect to the $(2)^2A'$ neutral, resulting in a large amplitude of the photoionization cross section. Note however that there is still some loss of amplitude, since the second most dominant electronic configuration of the ion is a 2h-1p with respect to the $(2)^2A'$ neutral.

In Fig.7.9(c) we plot the asymmetry parameter for the photoionization from both neutral states leaving the ion in the $(1)^1A'$ state. For photon energies above 50eV there is almost no signature of the change of electronic

configurations of the neutral or the ionic states. For photon energies below 50eV we notice that there is a pronounced change of the asymmetry parameter as γ passes by the conical intersection (see Fig.7.9(c)).

(1)³A' residual ionic state

For the photoionization from the (1)²A' and (2)²A' neutral states and leaving the cation in the (1)³A' state (see Fig.7.9(b)), the cross section is approximately homogeneous for ($80^\circ < \gamma < 160^\circ$, $r_a \neq 0$). This can be understood by the same analysis done in the last section: the (1)³A' state has a ... $(9a')^1(10a')^1$ leading electronic configuration, thus, a difference of exactly one spin-orbital in relation to the relevant electronic configuration of both neutral states for all γ and r_a considered here. Consequently, we do not observe any significant decrease of the cross section in Fig.7.9(b).

The asymmetry parameter for photoionization of both neutral states with a (1)³A' residual cation shown in Fig.7.9(c), also exhibit a sudden change of amplitude when crossing the conical intersection at low photon energies, in analogy to the photoionization with a (1)¹A' residual cation.

7.2.5 Dyson Orbitals

An analysis of the Dyson orbitals close to the conical intersection sheds light on the abrupt change of the asymmetry parameter previously observed. In Fig.7.10 we show the Dyson orbitals for photoionization from the (1)²A' and (2)²A' neutral states leaving the ion in the (1)¹A' and (1)³A' states at $\gamma = 108^\circ$ and $\gamma = 103^\circ$ ($r_a = 0\text{\AA}$). Taking the example of the transition with (1)¹A' final ionic state, we note that the Dyson orbitals for photoionization from the (1)²A' and (2)²A' states are swapped as the system goes through the conical intersection. This results in an abrupt change of the angular pattern of the Dyson orbital, as observed in Fig.7.10. Indeed, at the molecular axis nodal planes becomes maxima and vice versa. Therefore, the abrupt changes of the asymmetry parameter are related to the abrupt change of the angular pattern of the Dyson orbitals.

7.2.6 PADs

From Fig.7.13 to Fig.7.20 we show the PADs for parallel and perpendicular alignment for photoionization from the (1)¹A' and the (2)¹A' neutral state

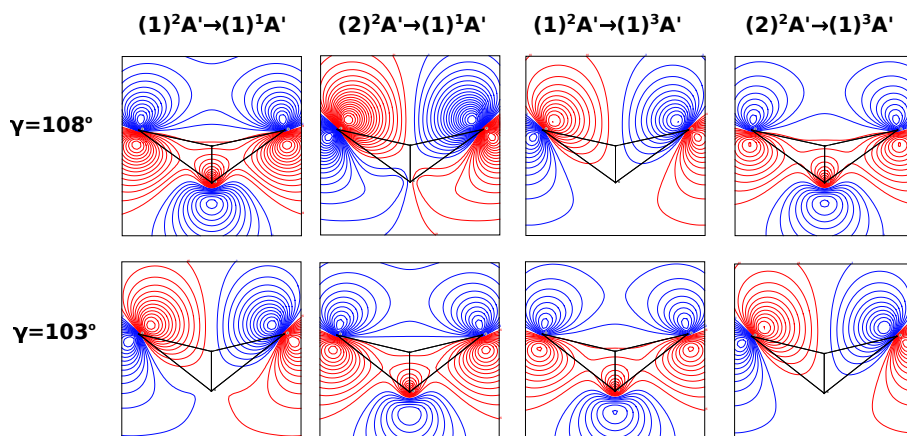


Figure 7.10: Dyson orbitals for $r_a = 0\text{\AA}$ for $\gamma = 108^\circ$ (top) and $\gamma = 103^\circ$ (bottom). The initial and final states of the photoionization process for each column are shown at the top the figure. Note as the system goes through the conical intersection, the Dyson orbital of the $(1)^2A' \rightarrow (1)^1A'$ and the $(2)^2A' \rightarrow (1)^1A'$ transitions are swapped. The same happen for transitions with the $(1)^3A'$ final state.

leaving the ion in the $(1)^1A'$ and $(1)^3A'$ states in the vicinity of the conical intersection. As in the equilibrium photoionization calculations of NO_2 presented, the partial wave channels involved in the photoionization of a laser polarized in the $\hat{\mathbf{y}}$ axis has only even l and m components, thus \mathbf{yx} and \mathbf{yz} are nodal planes.

For $r_a = 0\text{\AA}$ we observe a node along the molecular axis in the PADs for different values of γ , which is also observed in the plot of the Dyson orbitals. For example, in the photoionization from the $(1)^2A'$ state leaving the ion in the $(1)^1A'$ state, in case the dipole is oriented along the molecular axis, this node occurs whenever $\gamma < 107^\circ$ (Figs.7.13). The origin of this node can be explained by analyzing the irrep spanned by the continuum electron in the C_{2v} point symmetry group. For $\gamma > 107^\circ$ the $(1)^2A'$ state maps into the $(1)^2A_1$ and $(2)^2A_1$ states for $\gamma > 107^\circ$ and $\gamma < 107^\circ$ respectively. The dipole operator in the case of parallel alignment spans the A_1 irrep. Therefore, the dipole operator spans the totally symmetric irreducible representation group A_1 only if the final scattering state spans the irrep A_1 for $\gamma > 107^\circ$ and B_1 for $\gamma < 107^\circ$. Consequently, as in this specific example we are interested in the term of the scattering state coupled to the $(1)^1A_1$ target state, the

continuum electron spans the A_1 irrep for $\gamma > 107^\circ$ and the B_1 irrep for $\gamma < 107^\circ$. As the B_1 irrep has a reflection plane along the molecular axis, the continuum electron has necessarily a node at the molecular axis, as confirmed in Fig.7.13. The same arguments are valid for explaining the nodal planes observed in Fig.7.13 to Fig.7.20. In Fig.7.12 we show a complete list of the irrep relevant from the ground and first excited neutral states, the dipole operator, scattering states with their respective target and continuum states.

It is also possible to identify the relevant partial wave channels in the PADs, specially for high photon energies. For a continuum electron spanning the B_1 irrep, the partial waves have any value of l and odd positive defined magnetic quantum number. For a continuum electron spanning the A_1 irrep, the partial waves have any value of l and $m = 0$. In Fig.7.11 we plot the spherical harmonics that spans the B_1 irrep for m being odd positive defined, and $l = 6, 5$. Taking again as an example the PAD for parallel dipoles for photoionization from the ground neutral state and leaving the ion in the $(1)^1A_1$ symmetry ($r_a = 0$), we observe that in the PAD corresponding to a B_1 continue there is a local maxima at an emission of angle 90° at high energies, which most probably comes from the partial waves with $l = 5$, since the partial waves with $l = 6$ have a node at such an emission angle. At lower energies there is a strong mixing between different partial waves and it becomes hard to draw strong conclusions. However, for a B_1 continue we can clearly see that at photon energies of 30eV the Y_{11} , Y_{31} and Y_{33} starts to be important for producing the maxima at the such photon energies seen in the PAD (Fig.7.13) at an emission angle of 90° .

7.3 Discussion

We performed NO_2 photoionization calculations for a range of geometries, specially, close to the conical intersection between the $(1)^2A'$ and $(2)^2A'$ neutral states. We looked at partial cross section, asymmetry parameters, Dyson orbitals and PADs from photoionization leaving the ion in the $(1)^1A'$ and $(1)^3A'$ states. In the case of $r_a = 0\text{\AA}$, for partial cross section leaving the ion in the $(1)^1A'$ state we saw a peak in the signal in photoionization from the $(2)^2A'$ state due to the conical intersection in the neutral and the avoided crossing between the $(1)^1A'$ and $(2)^2A'$ ionic states at $102^\circ \leq \gamma \leq 107^\circ$. Away from this region the signal was low. This was due to the character of the ionic state changing from a satellite to a main line state when passing through the

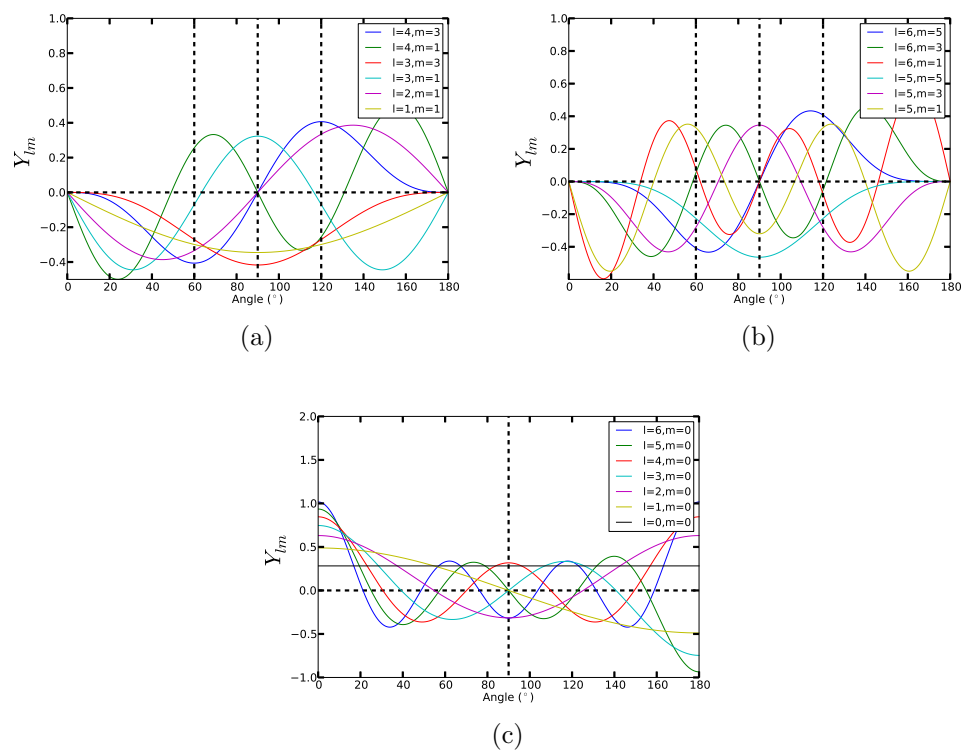


Figure 7.11: Spherical harmonics for the relevant partial wave channels in the photoionization of NO_2 at the range of geometries considered here.

$$\begin{array}{c}
\langle \Psi_{\text{neut}} | \mu (\parallel) | \Psi_{\text{scat}} \rangle \quad \langle \Psi_{\text{neut}} | \mu (\perp) | \Psi_{\text{scat}} \rangle \\
\begin{array}{c} \mathbf{A}_1 \\ \mathbf{B}_1 \end{array} \left| \begin{array}{c} \mathbf{A}_1 \\ \mathbf{A}_1 \end{array} \right. \left\{ \begin{array}{l} \text{tgt.} \quad \text{cont.} \\ \mathbf{A}_1 \oplus \mathbf{A}_1 \\ \mathbf{A}_2 \oplus \mathbf{A}_2 \\ \mathbf{B}_1 \oplus \mathbf{B}_1 \\ \mathbf{B}_2 \oplus \mathbf{B}_2 \end{array} \right. \begin{array}{c} \mathbf{A}_1 \\ \mathbf{B}_1 \end{array} \left| \begin{array}{c} \mathbf{A}_1 \\ \mathbf{B}_1 \end{array} \right. \left\{ \begin{array}{l} \text{tgt.} \quad \text{cont.} \\ \mathbf{A}_1 \oplus \mathbf{A}_1 \\ \mathbf{A}_2 \oplus \mathbf{A}_2 \\ \mathbf{B}_1 \oplus \mathbf{B}_1 \\ \mathbf{B}_2 \oplus \mathbf{B}_2 \end{array} \right. \begin{array}{c} \mathbf{A}_1 \\ \mathbf{B}_1 \end{array} \left\{ \begin{array}{l} \mathbf{A}_1 \oplus \mathbf{B}_1 \\ \mathbf{A}_2 \oplus \mathbf{B}_2 \\ \mathbf{B}_1 \oplus \mathbf{A}_1 \\ \mathbf{B}_2 \oplus \mathbf{A}_2 \end{array} \right.
\end{array}$$

Figure 7.12: Irrep, in C_{2v} , from the ground and first excited neutral states of NO_2 (Ψ_{neut}), the dipole operator for parallel (left) / perpendicular (right) alignment and the scattering state $\Psi^{(-)}$. For $\gamma > 107^\circ$ the ground and first excited neutral states belongs to the A_1 and B_1 irrep respectively. For $\gamma < 107^\circ$ the symmetry between both neutral states is swapped. We just show in the table the products such that $\langle \Psi_{\text{neut}} | \mu | \Psi^{(-)} \rangle \neq 0$, i.e., the direct product between each of the terms spans the A_1 irrep. In brackets we show the irrep from the target and continuum states which leads to the respective irrep of the scattering state.

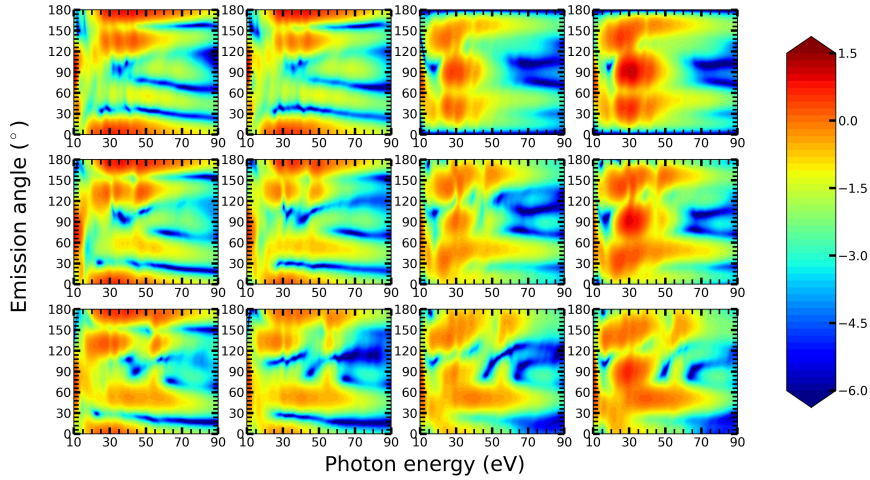


Figure 7.13: PADs parallel to the molecular axis, for photoionization from the $(1)^2A'$ state leaving the ion in the $(1)^1A'$ state. Each row shows the PAD for different r_a (from top to bottom, $r_a = 0, 0.1, 0.2\text{\AA}$) Each column shows the PAD for different γ (from left to right, $\gamma = 115^\circ, 108^\circ, 103^\circ, 96^\circ$)

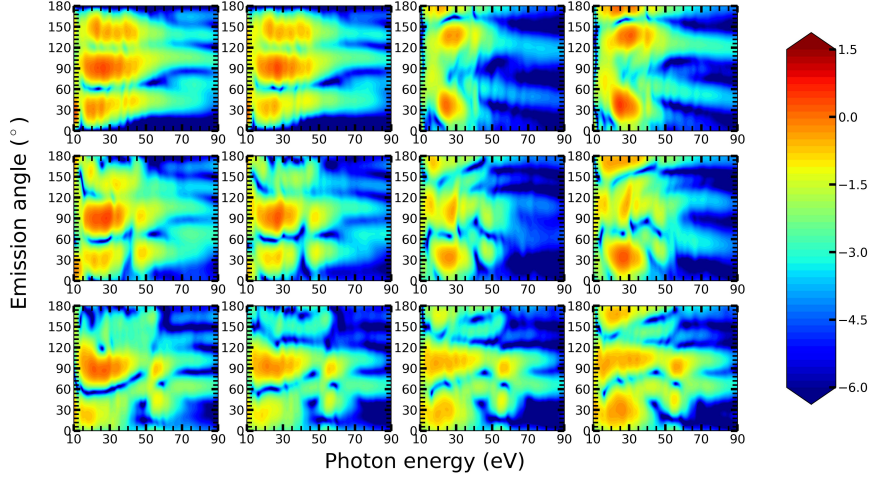


Figure 7.14: PADs perpendicular to the molecular axis, for photoionization from the $(1)^2A'$ state leaving the ion in the $(1)^1A'$ state. Each row shows the PAD for different r_a (from top to bottom, $r_a = 0, 0.1, 0.2\text{\AA}$) Each column shows the PAD for different γ (from left to right, $\gamma = 115^\circ, 108^\circ, 103^\circ, 96^\circ$)

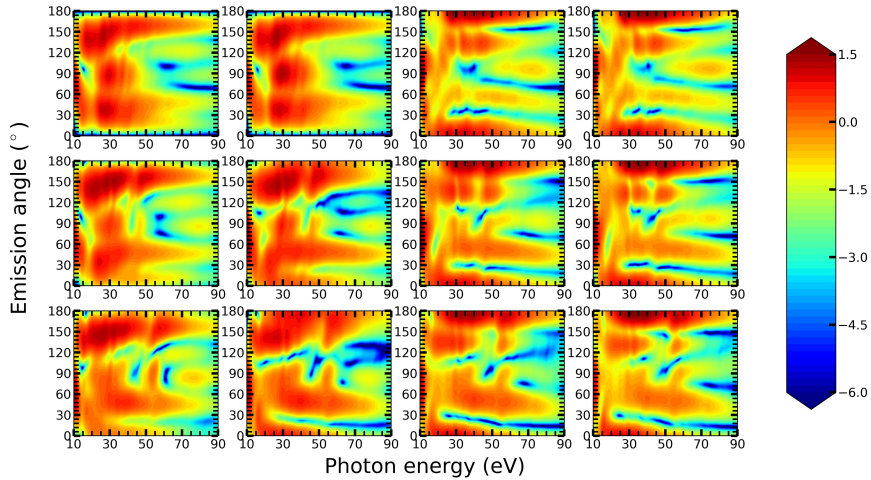


Figure 7.15: PADs parallel to the molecular axis, for photoionization from the $(1)^2A'$ state leaving the ion in the $(1)^3A'$ state. Each row shows the PAD for different r_a (from top to bottom, $r_a = 0, 0.1, 0.2\text{\AA}$). Each column shows the PAD for different γ (from left to right, $\gamma = 115^\circ, 108^\circ, 103^\circ, 96^\circ$).

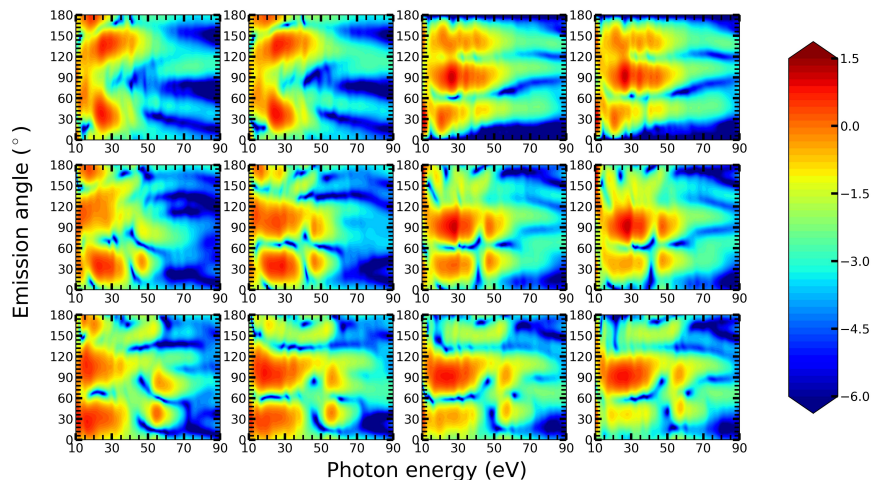


Figure 7.16: PADs perpendicular to the molecular axis, for photoionization from the $(1)^2A'$ state leaving the ion in the $(1)^3A'$ state. Each row shows the PAD for different r_a (from top to bottom, $r_a = 0, 0.1, 0.2\text{\AA}$). Each column shows the PAD for different γ (from left to right, $\gamma = 115^\circ, 108^\circ, 103^\circ, 96^\circ$).

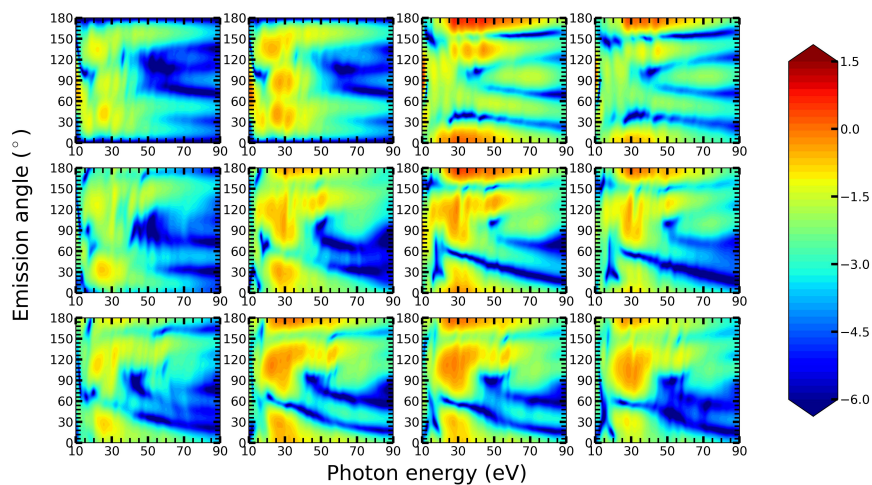


Figure 7.17: PADs parallel to the molecular axis, for photoionization from the $(2)^2A'$ state leaving the ion in the $(1)^1A'$ state. Each row shows the PAD for different r_a (from top to bottom, $r_a = 0, 0.1, 0.2\text{\AA}$). Each column shows the PAD for different γ (from left to right, $\gamma = 115^\circ, 108^\circ, 103^\circ, 96^\circ$).

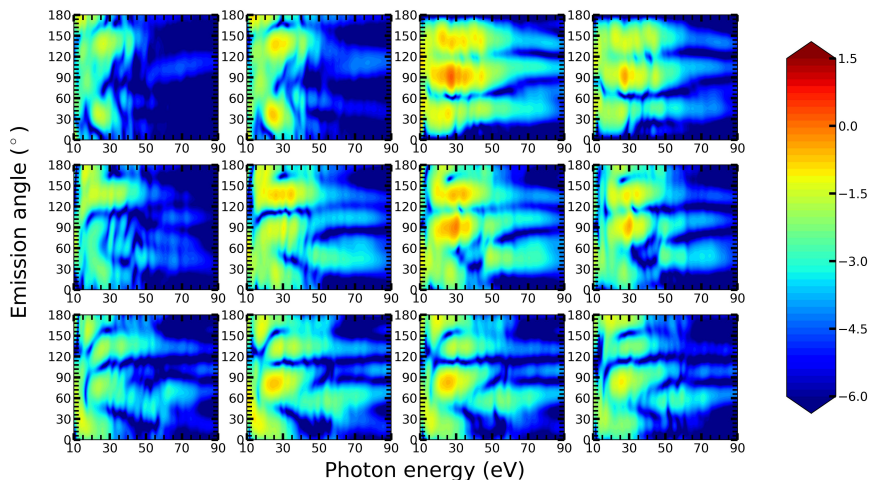


Figure 7.18: PADs perpendicular to the molecular axis, for photoionization from the $(2)^2A'$ state leaving the ion in the $(1)^1A'$ state. Each row shows the PAD for different r_a (from top to bottom, $r_a = 0, 0.1, 0.2\text{\AA}$). Each column shows the PAD for different γ (from left to right, $\gamma = 115^\circ, 108^\circ, 103^\circ, 96^\circ$).

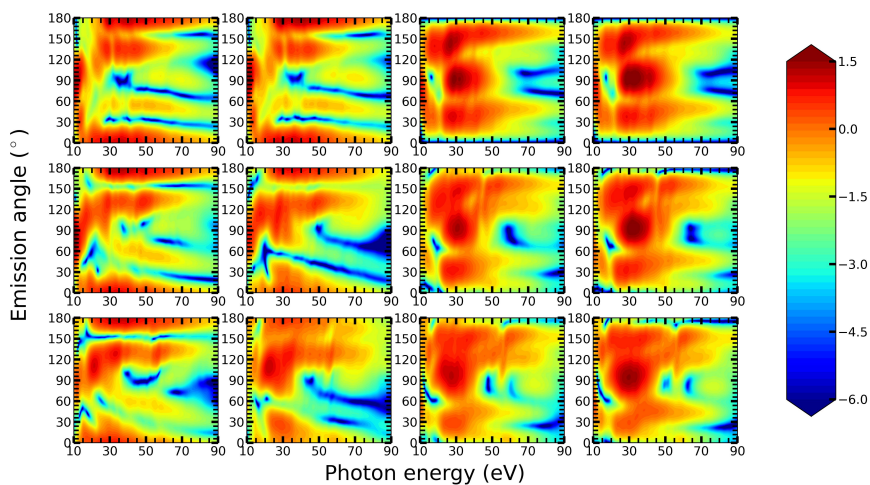


Figure 7.19: PADs parallel to the molecular axis, for photoionization from the $(2)^2A'$ state leaving the ion in the $(1)^3A'$ state. Each row shows the PAD for different r_a (from top to bottom, $r_a = 0, 0.1, 0.2\text{\AA}$). Each column shows the PAD for different γ (from left to right, $\gamma = 115^\circ, 108^\circ, 103^\circ, 96^\circ$).

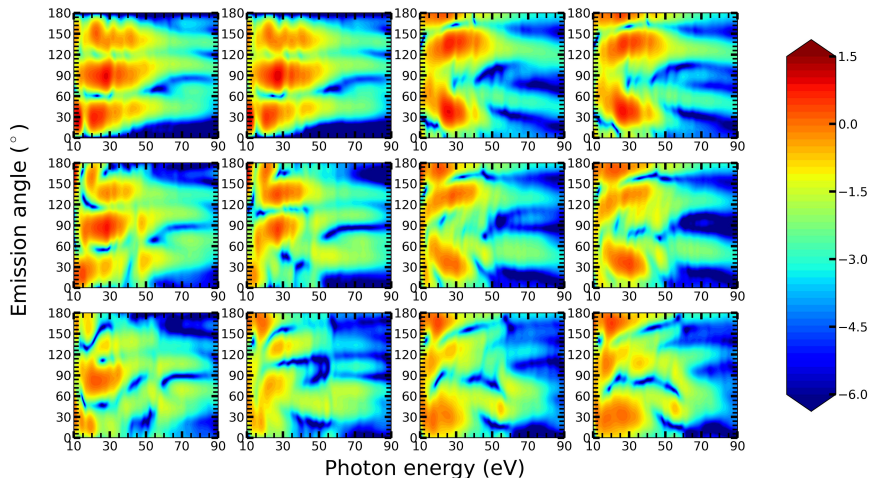


Figure 7.20: PADs perpendicular to the molecular axis, for photoionization from the $(2)^2A'$ state leaving the ion in the $(1)^3A'$ state. Each row shows the PAD for different r_a (from top to bottom, $r_a = 0, 0.1, 0.2\text{\AA}$). Each column shows the PAD for different γ (from left to right, $\gamma = 115^\circ, 108^\circ, 103^\circ, 96^\circ$).

conical intersection ($\gamma \approx 107^\circ$), then back to a satellite state when passing through the avoided crossing ($\gamma \approx 102^\circ$). The opposite happens with ionization from the $(1)^2A'$ state with a dip showing up at $102^\circ \leq \gamma \leq 107^\circ$. For the photoionization leaving the ion in the $(1)^3A'$ state, the cross section remains a main line state throughout the range of geometries investigated, resulting in a relatively homogeneous signal.

The asymmetry parameter for photoionization leaving the ion in the $(1)^1A'$ and $(2)^3A'$ state shows a sharp change (≈ 0.3) upon passing through the conical intersection, due to the change in dominant orbital involved in the ionization (from $9a'$ to $10a'$). This was later confirmed by the sudden change of the angular pattern of the Dyson orbitals as one passes through the the conical intersection.

Inspection of the irrep spanned by the continuum orbitals leads one to expect a maxima(/nodal plane) at 0° in the MFPAD for ionization from the $9a'$ ($10a'$) orbitals. Looking at the Dyson orbitals and the MFPADs this is exactly what we see as we pass through the conical intersection.

As the asymmetric stretch is varied the main change we see is the appearance of a resonance with a constant position across the entire angular range.

For $r_a = 0.1\text{\AA}$ we see it at $\approx 50\text{eV}$ in all cross sections. For $r_a = 0.2\text{\AA}$ it has moved to $\approx 57\text{eV}$.

To the best of our knowledge, we presented in this chapter the first photoionization calculations over a large grid of reaction coordinates using robust CI methods for describing both the neutral and the ionic states. It would be interesting in the future to investigate the TR-PES for photoionization leaving the residual ion either in higher excited states, or close to the dissociation limit. Another possibility, is to use photorecombination transition dipoles (the time reversal of the photoionization transition dipoles) as the final recombination step in the theoretical description of HHG from NO_2 for applications in high harmonic spectroscopy.

Chapter 8

R-Matrix with weak static fields

In this chapter, we present an extension of the UKRmol electron-(photon)-molecule scattering code suit [106, 215] that allows for the inclusion of a weak external static electric field. The method presented here could be used to investigate electron scattering and photoionization of molecules embedded in a DC field, as it is known that external fields induce important structural changes on the autoionizing resonances of the system, and also used to understand the response of atoms and molecules to low-frequency laser fields, e.g., in the mid-IR regime.

As a first application, we will study the effect of the static field on the Feshbach resonances converging to the first excited state of H_2^+ ($1\Sigma_u^+$) and He^+ . These resonances follow a Fano profile, and their origin is the temporary trapping of the system in a Rydberg like state [102]. Subsequently, due to electronic correlation, the system autoionizes, i.e., the continuum electron is ejected and the cation decays to the first excited state of the cation. Particularly interesting are the characteristics of the autoionizing states under the influence of a static electric field. In these conditions, effects such as Stark splitting and rearrangement of the autoionizing states were previously reported [216, 217]. Experimentally the scenario is extremely rich, as at fields of 85 KeV/cm a high number of new states, and a strong interaction between them is observed [218, 219, 220, 221]. Recent calculations qualitatively corroborate the experimental findings, but are still far from fully reproducing the laboratory results [222, 223, 224].

This chapter is organized as follows: in section 1 we discuss how a static

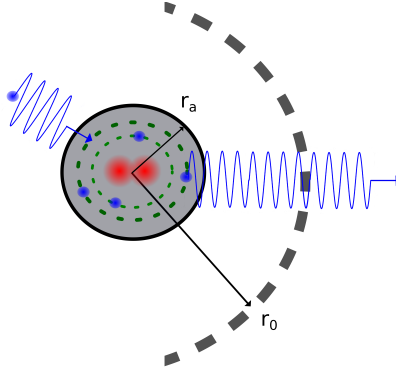


Figure 8.1: Schematic illustration of the R-Matrix method in a static electric field. Blue circles are electrons and red are nuclei. The inner, outer and asymptotic regions are delimited by $r < r_a$, $r_a < r < r_p$ and $r > r_p$ respectively. The static electric field is included in the inner and outer region.

electric field affects the molecular R-Matrix theory already presented in chapter 4, in section 2 we present how the static electric field affects the autoionizing resonances converging to the first excited state of H_2^+ .

8.1 R-Matrix with static electric field

Under the influence of an external static electric field, the stark Hamiltonian is given by

$$\mathbf{H}_{\text{st}}^{N+1} = \mathbf{H}^{N+1} + \mathbf{d}, \quad (8.1)$$

$$\mathbf{d} = \sum_{n=1}^{N+1} \mathbf{F}_s \cdot \mathbf{r}_n, \quad (8.2)$$

where \mathbf{F}_s stands for the static electric field strength, r_n is the radial coordinate of the n^{th} electron, \mathbf{d} is the interaction potential \mathbf{H}^{N+1} is the usual molecular Hamiltonian. It is straightforward to show that the potential added by the field is Hermitian. Thus, we do not have to adapt the Bloch operator discussed in Chapter 2. Note that the static electric field considered in our present calculation has a limited range, i.e., we implement a cut off sufficiently far away from the scattering center, and use simply the well known field free asymptotics (Coulomb or Bessel functions) for $r \geq r_p$.

8.1.1 Inner region

A non-zero \mathbf{d} results in changes to the structure of the Hamiltonian matrix. In the field free case, the symmetry of the molecular system can be used to decompose the Hamiltonian matrix into a direct sum over irreducible representations, $\mathbf{H}^{N+1} = \bigoplus_{\Gamma} \mathbf{H}^{N+1,\Gamma}$. On the other hand the addition of a static electric field induces couplings between different irreducible representation, thus breaking the symmetry of the system. For example, suppose a target belonging to the D_{2h} point group, with scattering wavefunctions in the $\Sigma_u, \Sigma_g, \Pi_g$ and Π_u irreducible representations. A static electric field in the $\hat{\mathbf{z}}$ direction couples the Σ_u and Σ_g , and the Π_u and Π_g as shown in the scheme below

$$\begin{pmatrix} \Sigma_g & 0 & 0 & 0 \\ 0 & \Sigma_u & 0 & 0 \\ 0 & 0 & \Pi_g & 0 \\ 0 & 0 & 0 & \Pi_u \end{pmatrix} \xrightarrow{\mathbf{F} \text{ in } \hat{\mathbf{z}}} \begin{pmatrix} \Sigma_g & \langle \Sigma_g | \mathbf{d} | \Sigma_u \rangle & 0 & 0 \\ \langle \Sigma_u | \mathbf{d} | \Sigma_g \rangle & \Sigma_u & 0 & 0 \\ 0 & 0 & \Pi_g & \langle \Pi_g | \mathbf{d} | \Pi_u \rangle \\ 0 & 0 & \langle \Pi_u | \mathbf{d} | \Pi_g \rangle & \Pi_u \end{pmatrix}.$$

The general form of the Hamiltonian, \mathbf{H}_{st}^{N+1} , in the field-free eigenfunctions basis is,

$$\mathbf{H}_{st}^{N+1} = \sum_{jj'\Gamma\Gamma'} \left(E_{j\Gamma} \delta_{jj'} \delta_{\Gamma\Gamma'} + \sum_n \langle \psi_j^{(N+1)\Gamma'} | \mathbf{d} | \psi_{j'}^{(N+1)\Gamma} \rangle \right), \quad (8.3)$$

where $E_{j\Gamma}$ are the j^{th} field-free eigenvalues belonging to the symmetry Γ .

By diagonalizing \mathbf{H}_{st}^{N+1} we obtain the Stark eigenvectors ($\psi_{st,j}^{(N+1)\Gamma}$) and eigenvalues ($E_{st,j}$). For computational results, it is more convenient to diagonalize the Stark shifted Hamiltonian in the field-free eigenfunction basis, and later on transform the eigenfunctions to the canonical basis by doing

$$\boldsymbol{\psi}^{(\text{st},\mathbf{N}+1)} = \boldsymbol{\psi}^{(\mathbf{N}+1)} \tilde{\boldsymbol{\psi}}^{(\text{st},\mathbf{N}+1)}, \quad (8.4)$$

where $\boldsymbol{\psi}^{(\mathbf{N}+1)}$ is simply the field-free eigenfunction matrix.

The Stark scattering wavefunction is then written as

$$\Psi_{st,k}^{N+1}(E) = \sum_{\Gamma f} A_{st,kf}^{\Gamma}(E) \psi_f^{(N+1)\Gamma}, \quad (8.5)$$

and the stark shifted R-Matrix is then finally given by

$$R_{st,ii'}(E, r_a) = \sum_{\Gamma} R_{st,ii'}^{\Gamma}(E, r_a) \quad (8.6)$$

with

$$R_{st,ii'}^\Gamma(E, r_a) = \frac{1}{2r_a} \sum_j \frac{\xi_{st,ij}^\Gamma(r_a) \xi_{st,i'j}^\Gamma(r_a)}{E_j^{st} - E}. \quad (8.7)$$

where E_j^{st} being the Stark shifted eigenvalues and $\xi_{st,ij}^\Gamma$ the Stark shifted boundary amplitudes

$$\xi_{st,ij}^\Gamma(r_a) = \langle r_{N+1}^{-1} \tilde{\Phi}_i^\Gamma | \psi_{st,j}^{(N+1)\Gamma} \rangle'. \quad (8.8)$$

8.1.2 Outer region

Following the steps of the inner region, we define the close coupling expansion in the outer region as

$$\Psi_{st,k}^{N+1}(E) = \sum_\Gamma \tilde{\Phi}_i^\Gamma(\mathbf{x}_1, \dots, \mathbf{x}_N; \sigma_{N+1}) r_{N+1}^{-1} F_{ik}^\Gamma(r_{N+1}), \quad (8.9)$$

with i labeling the partial wave channels belonging to the symmetry Γ . The Hamiltonian H_{st}^{N+1} can be written as

$$\mathbf{H}_{st}^{N+1} = \mathbf{H}^N - \frac{\nabla_{N+1}^2}{2} - \frac{Z}{r_{N+1}} + \sum_{i=1}^N \frac{1}{r_{iN+1}} + \sum_{i=1}^{N+1} \mathbf{F}_s \cdot \mathbf{r}_i \quad (8.10)$$

Applying \mathbf{H}_{st}^{N+1} to Eq. 8.9 and using the properties of the channel functions

$$\left[-\frac{d}{dr^2} + \frac{l_i \Gamma(l_i \Gamma + 1)}{r^2} - \frac{2Z}{r} - k_{i\Gamma}^2 \right] F_{ik}^\Gamma(r_{N+1}) = 2 \sum_{i'\Gamma'} V_{ii'}^{\Gamma\Gamma'} F_{i'k}^{\Gamma'}(r_{N+1}) + 2 \sum_{\Gamma'i'} \langle \tilde{\Phi}_{i'}^{\Gamma'} | \mathbf{d} | \tilde{\Phi}_i^\Gamma \rangle F_{i'k}^{\Gamma'}(r_{N+1}). \quad (8.11)$$

Apart from the last dipole term, Eq. 8.11 are the usual reduced radial equations for the electron scattering problem. The long range potential in this case includes the couplings between channels belonging to different symmetries. This potential and the laser field induce a non-diagonal coupling between the asymptotic channels, raising effects such as the redistribution of resonance amplitudes and widths.

8.1.3 Asymptotic region

Clearly in the length gauge, the field has a stronger effect at large distances from the center of mass of the molecule. However, here we are mainly interested in autoionizing resonances that are confined in space, there is no need for using the exact asymptotic solutions of \mathbf{H}_{st}^{N+1} . Thus, we will match the R-Matrix at r_p with the field free asymptotic solutions of the system. This assumption of course breaks down if the field becomes strong, since reflections at the outer/asymptotic region boundary would affect the quality of the characteristics of the autoionizing resonances.

8.2 Resonance Analysis

The autoionizing resonances were analyzed with the program RESON [225], which fits the resonance peak positions (E_i^{res}) and widths (Γ_i^{res}) using the Breit-Wigner equation

$$\omega(E) = \sum_{i=1}^M \tan^{-1} \left[\frac{\Gamma_i^{res}}{E - E_i^{res}} \right] + \sum_{i=1}^N q_i(E)^i, \quad (8.12)$$

where ω is the eigenphasesum obtained by diagonalizing the K-Matrix of the system. The second summation accounts for the resonance background. The quantum defects (μ) can also be extracted by evaluating

$$E_i^{res} = - \left[\frac{Z}{N} \right]^2 + \left[\frac{Z-1}{n^*} \right]^2, \quad (8.13)$$

$$n^* = n - \mu, \quad (8.14)$$

where $N = 2$, as we are studying the second ionization threshold.

8.3 $e - H_2^+$ scattering in a static electric field.

We first prepared a field-free calculation using a cc-PVTZ basis for the hydrogen atoms [226] and a SA-CASSCF procedure to obtain the molecular orbitals using MOLRPO[170]. The internuclear distance between the hydrogen atoms was set to $1.4 a_0$. The cationic states $(1)^1\Sigma_g^+$, $(1)^1\Sigma_u^+$ and $(1)^1\Pi_u^+$ were included in the close coupling expansion. Note that D_{2h} is the highest symmetry allowed in the UKRmol codes for linear molecules.

ν	Position (eV)	Position (eV) [227]	Width(eV)	Width(eV) [227]
$^1\Sigma_g^+$				
1.600	12.97	12.87	0.940	0.770
2.765	16.48	16.95	0.116	0.107
3.778	17.31	17.81	0.045	0.043
4.782	17.67	18.17	0.022	0.023
5.784	17.86	18.36	0.013	0.014
6.786	17.97		0.007	
$^1\Pi_u$				
1.924	14.60	14.76	0.446	0.553
2.902	16.65	17.11	0.110	0.084
3.887	17.36	17.86	0.037	0.034
4.884	17.69	18.19	0.018	0.017
5.885	17.87	18.37	0.012	0.010
6.890	17.98		0.009	

Table 8.1: Field-free Rydberg series of H_2^{**} with total symmetries $^1\Sigma_g^+$ and $^1\Pi_u$. Energies are given in relation to the first excited state threshold of H_2^+ . Terms lying deeper on the Rydberg series are not considered, since they require a better description of the polarization of the target, and a continuum with higher angular momentum.

The R-Matrix boundary was placed at $10 a_0$ from the center of mass of the molecule. The continuum basis is given in terms of Gaussian type orbitals spanning an energy range up to $3H$ and with $l \leq 4$. Table 8.1 shows the Rydberg series converging to the second ionic threshold obtained in the $e + H_2^+$ calculations. No virtual orbitals were included in the inner region calculation.

In Table 8.1, we present the autoionizing resonances found in the $^2\Sigma_g^+$ and $^2\Pi_u$ scattering symmetries, converging to the first excited state of H_2^+ . The agreement between the resonance widths obtained here and reported in [227] is excellent. The resonance positions found here are consistently 0.5eV below the ones in [227], and this is due to inaccuracies in the calculation of the cationic states of H_2^+ . We included fields up to 6×10^{-5} atomic units in the same direction of the nuclear axis (see the inset of Fig.8.2). Because of the high number of angular momentum included in the continuum basis, we had to propagate the R-Matrix from 10 to 100 a_0 in order to eliminate the dependency of the resonance position with the propagation radius. It is

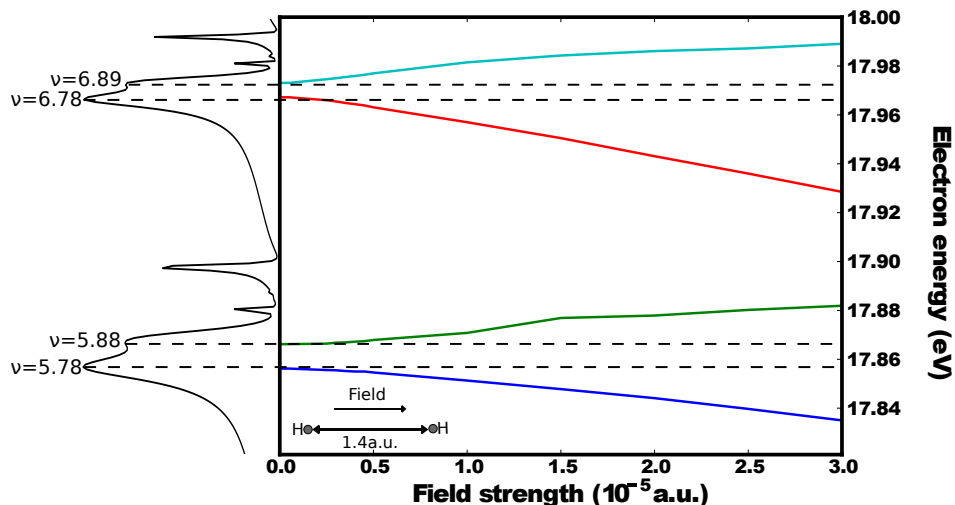


Figure 8.2: Stark shifts for the $e - H_2^+$ scattering with a static electric field. The field is directed along the molecular axis, as shown in the inset of the figure. On the left we show the field free scattering cross section of the autoionizing resonances being analyzed.

important to highlight that the changes of the resonance position with the field were minimal from a propagating radius of 50 to 100 a_0 , thus we can conclude that the calculations are converged.

Autoionizing resonances found below 17eV are not affected at all by the fields considered here, since these resonances are confined close to the molecular center of mass, a region where the field effects are negligible. On the other hand resonances lying close to the ionic threshold are strongly affected by the field, since they are composed of partial waves with high angular momentum, i.e., the wavefunction of these Rydberg-like states are diffuse. Thus, we concentrate on the electron energies of 17.8 – 18 eV where the resonances with $\nu = 5.784, 6.786$ in $^1\Sigma_g^+$ and $\nu = 5.885, 6.890$ in $^1\Pi_u$ are found.

In the weak field regime investigated here, we note that the interaction between neighboring autoionizing resonances is dominant. As the $(\nu = 5.784)^1\Sigma_g^+ / (\nu = 5.885)^1\Pi_u$, and the $(\nu = 6.786)^1\Sigma_g^+ / (\nu = 6.890)^1\Pi_u$ resonance pairs are nearly degenerate, we observe a “splitting” of each resonance pair induced by the stark effect, which is linear in first order perturbation theory. For stronger fields, couplings between non-neighbor resonances are

expected as reported in [217].

We also notice that the field induces a mixing between the irreducible representations, thus, the series can not be classified as purely Σ_g^+ and Π_u types, an effect already reported in [228] for the case of photoionization in the presence of a strong IR field.

8.4 $e-He^+$ scattering and He photoionization in a static electric field.

8.4.1 Field free calculations.

UKRmol, in common with many quantum chemistry codes, uses a basis of Gaussian type orbitals (GTO) to construct the target orbitals. This allows one to import atomic/molecular orbitals generated by other codes. We performed a state averaged CASSCF calculation in Molpro [170] using the cc-pVQZ basis of neutral helium [229] supplemented with a set of even-tempered GTO of s and p character (see Table 8.2). The continuum orbitals were also constructed from a set of GTO, with exponents optimised to well represent Coulomb functions in the inner region. To avoid over completeness, we found it necessary to drop the first 2 s -type GTO from the cc-pVQZ basis set. The use of GTO to describe the continuum puts an upper limit of $\sim 20 a_0$ on the R-matrix boundary position, limiting the number of target states that can be included in the calculation. We found that a boundary of $r_a = 17a_0$ was large enough to fully contain up to the third excited state of He^+ . Our calculations lead to a ground state energy of He of $-2.8328H$ (experimental= $-2.8611H$ [230]). Table 8.3 shows target state energies for the states included in the close-coupling expansion. Converged results were observed after propagating the outer region channels up to $67a_0$ using a multiprecision LAPACK library [231].

In Fig. 8.3 we plot the electron scattering cross section (left) and the total eigenphase sum (right) obtained with our model. The first resonance observed in Fig. 8.3 at approximately 33 eV marks the beginning of the Rydberg series converging to the first excited ionic threshold of He . As the electron energy approaches the threshold (approximately 40.5eV in our model), an increasing number of resonances emerges. A good description of resonances deep in the Rydberg series is a demanding problem even for simple atom as Helium, as these resonances have an increasing sensitivity to

Table 8.2: cc-pVQZ and even tempered GTO's to represent the continuum basis of the He^+ target. The doublets are the normalization and exponential coefficients respectively for each gaussian.

		Basis set	
		cc-pVQZ	even-tempered GTO's
orbitals	s	(18.0500, 0.035975) (5.0850,0.127782) (1.6090, 1.00) (0.5636,1.00)	(0.25,1.00),(0.09,1.00) (0.10,1.00),(0.0650,1.00)
	p	(5.9940, 1.00), (1.7450,1.00) (0.56, 1.00)	(0.28, 1.00), (0.14,1.00) (0.10, 1.00), (0.07,1.00)

Table 8.3: Energy (in Hartrees) of the target states of He^+ for each of the principal quantum number (PQN) and angular momentum. The exact energies of the excited states are known, since He^+ is an hydrogenic atom.

PQN	$l = 0$	$l = 1$	Exact
1	-1.991		-2.000
2	-0.499	-0.498	-0.500
3	-0.200	-0.205	-0.222
4	0.094	0.060	-0.125

the polarizability of the system.

We analyzed the resonances observed in Fig.8.3 using the program RE-SON [225], which fits the resonance peak positions (E_i^{res}) and widths (Γ_i^{res}) using the Breit-Wigner equation for the eigenphase sum ω

$$\omega(E) = \sum_{i=1}^M \tan^{-1} \left[\frac{\Gamma_i^{res}}{E - E_i^{res}} \right] + \sum_{i=1}^N q_i(E)^i, \quad (8.15)$$

where ω is the eigenphase sum, and the second summation accounts for the resonance background. The quantum defects (μ) can also be extracted by evaluating

$$E_i^{res} = - \left[\frac{Z}{N} \right]^2 + \left[\frac{Z-1}{n^*} \right], \quad (8.16)$$

$$n^* = n - \mu, \quad (8.17)$$

where $N = 2$, as we are studying the second ionization threshold. Table 8.4 summarizes the Rydberg states correctly described by our model. The

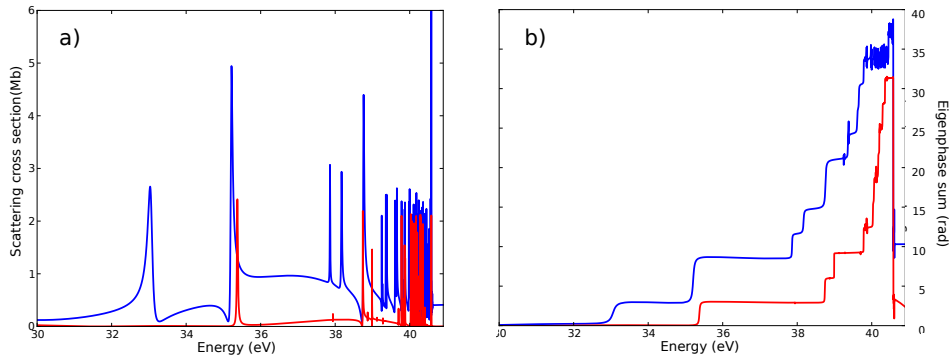


Figure 8.3: Field free $e^- + He^+$ scattering cross sections (a) and eigenphase sum (b) for the S (blue) and P (red) states.

resonance positions agrees very well with other calculations and experiments [230]. On the other hand, the width of the resonances becomes more inaccurate for resonances at higher electron energy, since more diffuse Rydberg states are increasingly more sensitive to a good description of the polarization of the system. It is important to highlight that the limitations on the R-matrix radius imposed by the use of GTO's in the UKRmol codes, is the main cause for a decreasing accuracy of the description of the high order resonances in the Rydberg series.

8.4.2 The effect of a static electric field on the Rydberg series of He^{**}

With a good calculation of field free $e - He^+$ scattering in hand, we add a static electric field to the system in the z direction. For low amplitude fields, we did not observe a variation of the autoionizing width and position for different field cut-offs. At low energies (below 39.8eV), the fields used in this work (typically $10^{-4}, 10^{-5} a.u.$) have a negligible effect on the autoionizing states shown in Table 8.4. On the other hand, close to the ionic threshold there is a considerable variation of the scattering cross section due to the field, as the wavefunction of the autoionizing states becomes increasingly more diffuse. Thus, we will focus our analysis on the region of 39.8 – 40 eV

Table 8.4: Field-free Rydberg series of He** . Terms lying deeper on the Rydberg series are not considered, since they require a better description of the polarization of the target.

Label	Position	Position [230]	Width	Width [230]	μ
(1S)2,2a	-1.5545	-1.5556	9.676(-3)	9.160(-3)	1.343
2,3a	-1.1764	-1.1797	2.689(-3)	2.760(-3)	2.379
2,4a	-1.0878	-1.0897	5.744(-4)	5.800(-4)	3.371
2,5a	-1.0524	-1.0533	1.478(-4)	4.200(-4)	4.361
(1D)2,2a	-1.3947	-1.4033	4.131(-3)	4.820(-3)	1.593
2,3a	-1.1338	-1.1382	2.026(-3)	1.400(-3)	2.723
2,4a	-1.0712	-1.0733	8.600(-4)	4.740(-4)	3.745
2,5a	-1.0440	-1.0454	4.074(-4)	2.380(-4)	4.758
(1P)2,2a	-1.3827	-1.3856	2.217(-3)	2.660(-3)	1.618
2,3a	-1.1320	-1.1280	1.350(-4)	6.200(-4)	2.751
2,4a	-1.0644	-1.0686	1.123(-5)	2.480(-4)	3.779
2,5a	-1.0402	-1.0429	3.047(-4)	1.316(-4)	4.979

where the resonances $(2, 5a)^1P^o$ and $(2, 5a)^1D^e$ are found, and rich dynamics are observed even for fields as low as $F \approx 10^{-5} a.u..$

$e^- + He^+$ scattering

Fig.8.4(a) shows the electron scattering cross section for several different field strengths. The field induces a strong interaction between autoionizing states coupled by the static electric field [217]. However, for weak fields the interaction between neighboring autoionizing states is dominant, and we can partially neglect the interaction between states well separated in energy.

The neighboring $(2, 5a)^1P^o$ and $(2, 5a)^1D^e$ autoionizing states are shifted towards lower energies due to the quadratic Stark shift [216]. As shown in Fig.8.4 (c), the shift of the resonance position obtained with our model is in good qualitative agreement with the calculation reported at [217]. Quantitative agreement is not expected, due to the current limitations of the UKRmol package to a maximum R-matrix boundary of $\approx 20a_0$, thus, more diffuse states necessary for describing the polarization of the system have to be neglected, since the boundary amplitude of the confined electrons would be non-negligible at the R-Matrix radius.

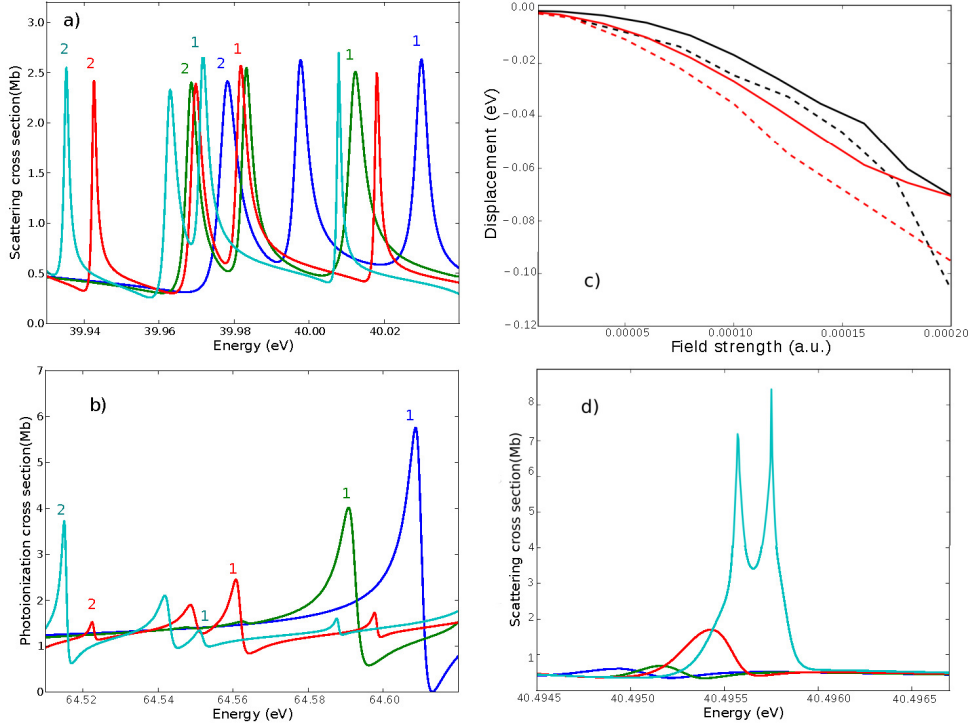


Figure 8.4: $e^- + He^+$ scattering (a) and photoionization (b) cross sections by electron energy for several field strengths (\mathbf{F}_s). In (a), (b) and (d) the blue curve corresponds to $\mathbf{F}_s = 0$ a.u., green to $\mathbf{F}_s = 0.8 \times 10^{-4}$ a.u., red to $\mathbf{F}_s = 1.4 \times 10^{-4}$ a.u. and cyan to $f = 1.6 \times 10^{-4}$ a.u. The labels 1 and 2 are placed on the positions of the $(2, 5a)^1P^o$ and $(2, 5a)^1D^e$ resonances respectively. In (c) we show the energy displacement of the $(2, 5a)^1P^o$ (red) and $(2, 5a)^1D^e$ (black) by field strength. The full lines are our results, dashed are the results reported at [217]. In (d) we show the resonance splitting for an increasing field strength.

In Fig.8.4 (d) we show the dynamics of an autoionizing state lying at 40.494 – 40.497 eV. The autoionizing state splits into two new states, as a consequence of the break of spherical symmetry induced by the field. This is an expected effect, since in the presence of the field the total angular momentum L is no longer a good quantum number and must be replaced by the projection of L on the field axis M . This implies that each resonance should split into $L + 1$ new states as the field strength is increased. In general, the field has a more notable effect on Rydberg states lying deeper in the series, i.e., states with high principal quantum numbers. This is as one would expect as they are more loosely bound and more likely to be found far from the ion in the region where the external field is dominant. The splitting was not observed for the autoionizing resonances in Fig. 8.4 (a), because the autoionizing states $(2, 5a)^1P^o$ and $(2, 5a)^1D^e$ are still relatively tightly bound when compared to the resonances shown in Fig. 3(d).

8.4.3 Photoionization of He

In Fig.8.4(b), we show the total photoionization cross section of He . The most striking effect induced by the field, is the emergence of the resonance $(2, 5a)_{M=0}^1D^e$ with increasing field strength. In the absence of the field, the transition $\langle \psi((2, 5a)_{M=0}^1D^e) | z | \psi_g \rangle$ is forbidden, as the ground wavefunction of He has a total angular momentum of $l = 0$. When a field in the \hat{z} direction is applied, there is a mixing of the atomic orbitals and the $(2, 5a)_{M=0}^1D^{e, st}$ state is written as a linear combination of the basis belonging to each of the coupled orbitals

$$\psi((2, 5a)_{M=0}^1D^{e, st}) = \sum_j \tilde{b}_{d,j} \psi_{d,j}^{N+1} + \sum_j \tilde{b}_{p,j} \psi_{p,j}^{N+1}. \quad (8.18)$$

In consequence, the photoionization dipole will take the form

$$\langle \psi((2, 5a)_{M=0}^1D^{e, st}) | z | \psi_g \rangle = \sum_j \tilde{b}_{p,j} \langle \psi_{p,j}^{N+1} | z | \psi_g \rangle, \quad (8.19)$$

justifying the observation of the $(2, 5a)_{M=0}^1D^e$ resonance. The coupling between different symmetry species is translated to the couple of resonances, which result in a redistribution of the resonance parameters as shown in Fig.8.4.

For stronger fields ($\approx 10^{-3}a.u.$), we start to observe the limitations of the approximation of neglecting the static electric field for $r \geq 67a_0$. As we

increase the field strength, boundary reflections in the region where we turn off the field starts to introduce unphysical artifacts.

8.5 Discussion

We have implemented the ability to include an external static electric field in the UKRmol codes. As a test of the new development, we studied the effect of a static electric field on the Rydberg series converging to the first excited state of H_2^+ and He^+ . We observed that the weak fields induces a low order stark effect that repels the quasi-degenerate auto-ionizing resonance. We note that the number of autoionizing resonances described by our codes could be dramatically increased by using a larger R-matrix radius, allowing us to include more ionic excited states in the inner region. Such a step, still needs to wait for the further development of the UKRmol+ package. The photoionization calculations on He shows that the field couples two irreducible representations of the system.

In the future, it would be interesting to extend the capability of the codes for dealing with strong static electric fields. This would allow us to investigate the role of the field in photorecombination in HHG, in adiabatic alignment techniques, and also tunnel ionization in a quasi-static picture. Note that for strong fields, approximating the asymptotics to the field free solutions results in strong reflections in the outer/asymptotic region boundary, thus, a correct treatment of asymptotic solution is necessary. A very powerful way of tackling this problem, is to use exterior complex scaling (ECS) [232, 233, 234] at the outer region of the UKRmol codes. In ECS, the electron spatial coordinates are multiplied by a phase $e^{i\phi}$. Substituting the scaled spatial coordinates in the Schrödinger equation, one obtains a dumped wavefunction that decays to zero in the asymptotic limit, so one never needs to worry about the correct asymptotics of the system. Ken Taylor and co-workers have developed in the 90's a R-Matrix+ECS method for the atomic codes [235]. In their work, they neglect the effect of the field in the inner region and match the solutions to the field free asymptotic solutions, extracting then the K-Matrix of the system and the wavefunction coefficients. ECS is then applied to the outer part of the wavefunction. Even though very clean and powerful, this method suffers from some limitations. It can not be applied to large molecules for example, since in this case the R-Matrix boundary is necessarily set at a large distance from the center of mass, and the field can not be

neglected in the inner region. Another possibility, would be to implement the exact static electric field asymptotics, which are a linear combination of regular and irregular Airy functions. This last possibility does not suffer from the limitation of the ECS, but its derivation and implementation are far more complicated than performing an ECS.

Chapter 9

Accurate photorecombination matrix elements for high harmonic spectroscopy

High harmonic generation is the result of the strong non-linear interaction of the target atom or molecule with an intense IR laser field. The HHG process can be factorized into the following three steps[71, 236]: (i) tunnel ionization of the electron through the target+static laser field potential, (ii) propagation of the electron in the continuum driven by the IR field, and (iii) recombination of the continuum electron with the parent ion, resulting in the generation of an attosecond burst of light.

The works [237, 91, 90] have laid the foundations for high harmonic spectroscopy [191, 238, 239], showing how a quantitative analysis of the recombination step allows one to gain access to both spatially- and temporally-resolved electron-hole dynamics triggered by the ionization step. The key component of this analysis is the need for accurate photorecombination matrix elements, as we show in this chapter.

This chapter is organized as follows: in section 9.1, we present a full quantum mechanical derivation of the HHG process that provides rigorous quantitative support for the 3-step model of HHG. In section 9.2 we theoretically evaluate the high harmonic spectra of aligned CO₂ for imaging the relevant orbitals of the molecule in the HHG process. The high harmonic spectra are calculated with two different models, which employ different methods for the evaluation of the recombination matrix elements: one uses the *ab initio* UKRmol package, the other, the Eikonal approximation. Both models share

the same ionization and propagation matrix elements, which are calculated using the formulas derived in section 9.1. A comparison of the two theoretical harmonic spectra with the experiments of Mairesse *et al.* [240] demonstrates the importance of employing accurate photorecombination matrix elements in the HHG calculations. Finally in section 9.3, we investigate the effects of the short temporal observation window of attosecond emission bursts associated with macroscopic propagation effects, which select the so called 'short trajectories' and suppress the contribution of the so-called "long trajectories" [14]. on the recombination step of HHG. Analyzing the experimental data of Pedatzur *et al.* [241] on the high harmonic spectroscopy in Helium gas, we show that the short duration of the attosecond pulse filters out sharp resonances of the recombination matrix elements used to model HHG.

9.1 Theory

Under the influence of an electromagnetic radiation, the dipole response of an atom or a molecule is

$$D(t) = \langle \Psi^N(\mathbf{r}, t) | \hat{\mathbf{d}} | \Psi^N(\mathbf{r}, t) \rangle, \quad (9.1)$$

with $\Psi^N(\mathbf{r}, t)$ being eigenfunctions of the following Hamiltonian

$$\mathbf{H}^N(t) = \mathbf{T}_e + \mathbf{T}_n - \sum_q \sum_i \frac{Z_q}{|\mathbf{R}_q - \mathbf{r}_i|} + \sum_{i \neq j} \frac{1}{|\mathbf{r}_j - \mathbf{r}_i|} - \sum_i \mathbf{F}(t) \cdot \mathbf{d}_i, \quad (9.2)$$

where \mathbf{T}_e and \mathbf{T}_n are the electronic and nuclear kinetic operator respectively, the third term is the electron-nuclei interaction, the fourth is the electron-electron interaction, and the last is the interaction of the electrons of the molecule with the laser field.

The Schrödinger equation of 9.2 is given by

$$i \frac{\partial \Psi^N(\mathbf{r}, t)}{\partial t} = \mathbf{H}^N(t) \Psi^N(\mathbf{r}, t), \quad (9.3)$$

$$\Psi^N(\mathbf{r}, t = t_0) = \Psi_n^N(\mathbf{r}), \quad (9.4)$$

where $\Psi_n^N(\mathbf{r})$ is the initial state of the molecule, and t_0 is the time of ionization. The solution from the Schrödinger equation above can be written in an

intuitive integral form [70]

$$\begin{aligned} |\Psi^N(t)\rangle &= - \int_{t=t_0}^t dt' U^N(t, t') \\ &\times V_L^N(t') U_0^N(t', t_0) |\Psi_n^N(\mathbf{r})\rangle + U_0^N(t, t_0) |\Psi_n^N(\mathbf{r})\rangle, \end{aligned} \quad (9.5)$$

where U_0^N is the field free propagator, which when applied to the eigenfunctions of \mathbf{H}^N yields

$$U_0^N(t', t_0) |\Psi_n^N(\mathbf{r})\rangle = e^{-iE_n(t'-t_0)} |\Psi_n^N(\mathbf{r})\rangle. \quad (9.6)$$

U^N on the other hand has non-trivial solutions, but can be simplified if we adopt the following assumptions: (i) there is no correlation between the continuum electron and the bound wavefunction, so the propagator can be factorized in a bound (U^N) and a continuum (U^e) part, and (ii) assume that sufficiently far away from the molecule the continuum electron is driven exclusively by the laser field.

Introducing the identity operator

$$\mathbf{I} = \int d\mathbf{p} \sum_m \mathcal{A} |\Phi_n^{N-1} \otimes \mathbf{p}_t^N\rangle \langle \Phi_n^{N-1} \otimes \mathbf{p}_t^N | \mathcal{A} \quad (9.7)$$

the dipole response can be written as

$$\begin{aligned} D(t) &= -i \langle \Psi_n^N(\mathbf{r}) | \mathbf{d} | \int_{t_0}^t dt' e^{iE_n(t-t')} \int d\mathbf{p} U^{N-1}(t, t') |\Phi_n^{N-1}\rangle \\ &\times U^e(t, t') | \mathbf{p}_{t'}^N \rangle \langle \mathbf{p}_{t'}^N | \Phi_n^{N-1} | V_L^N(t') | \Psi_n^N(\mathbf{r}) \rangle + c.c. \end{aligned} \quad (9.8)$$

Note that the $U^{N-1}(t, t') |\Phi_n^{N-1}\rangle$ term in Eq.9.8 accounts for the transfer of population of the ionic states induced by the laser field. We define the time-dependent transition amplitudes for ionization from an initial ionic state Φ_m at time t' , to the Φ_n state at time t as $a_{mn} = \langle \Phi_m^{N-1} | U^N(t, t') | \Phi_n^{N-1} \rangle$. The explicit form of the a_{mn} amplitudes are determined by solving the time dependent Schrödinger equation

$$\frac{d\mathbf{a}}{dt} = [\mathbf{H}_0^{N-1} + \mathbf{V}(t)] \mathbf{a}, \quad (9.9)$$

where \mathbf{H}_0^N is the field free Hamiltonian, \mathbf{a} is the vector of a_{mn} coefficients, and $\mathbf{V} = -\mathbf{d}_{mn} \cdot F(t)$, with $-\mathbf{d}_{mn}$ being the dipole coupling between the Φ_m and Φ_n ionic states.

It is convenient then to decompose the dipole response into

$$D(t) = \sum_{mn} D^{mn}(t), \quad (9.10)$$

$$D^{mn}(t) = i \int_{t_0}^t dt' \int d\mathbf{p} d_m^*(\mathbf{p} + A(t)) a_{mn}(t, t') e^{-iS_n(\mathbf{p}, t, t')} F(t') d_n(\mathbf{p} + A(t')) \quad (9.11)$$

where

$$S_n(\mathbf{p}, t, t') = \frac{1}{2} \int_{t'}^t [\mathbf{p} + A(\tau)]^2 d\tau + I_{p,n} \quad (9.12)$$

is the action, with $I_{p,n}$ being the ionization potential of the Φ_j^{N-1} ionic state. We also define in Eq.9.11 the ionization and recombination matrix elements respectively as

$$d_n(\mathbf{p} + A(t)) = \langle \mathbf{p} + A(t) | \mathbf{d} | \Psi_n^D \rangle, \quad (9.13)$$

$$d_m(\mathbf{p} + A(t)) = \langle \mathbf{p} + A(t) | \Phi_m^{N-1} | \mathbf{d} | \Psi_i^N(\mathbf{r}) \rangle, \quad (9.14)$$

where we have introduced the Dyson orbitals $\Psi_n^D = \langle \Phi_n^{N-1}(\mathbf{r}) | \Psi_i^N(\mathbf{r}) \rangle$, which is the overlap between the wavefunction of the initial neutral state and the wavefunction of the ionic state. Evaluating the integral over t' by parts we obtain

$$\int_{t_0}^t dt' e^{-iS(\mathbf{p}, t, t')} \mathbf{F}(t') d_n(\mathbf{p} + A(t')) = \int_{t_0}^t dt' e^{-iS(\mathbf{p}, t, t')} \Upsilon_n(\mathbf{p} + A(t')), \quad (9.15)$$

$$\Upsilon_n(\mathbf{p} + A(t')) = \left[\frac{(\mathbf{p} + A(t'))^2}{2} + I_{p,n} \right] \langle \mathbf{p} + A(t') | \Psi_n^D \rangle. \quad (9.16)$$

Note that Υ is effectively the Fourier transform of the dyson orbitals.

The high harmonic spectra is then finally given by

$$I(N\omega) \propto (N\omega)^4 |D(N\omega)|^2, \quad (9.17)$$

where $D(N\omega)$ is the Fourier transform of the dipole response

$$D(N\omega) = \int dt e^{iN\omega t} D(t) \quad (9.18)$$

Eq.9.11 can be written in a rather intuitive form if one uses the saddle point method [70], that allows the factorization of the ionization (a_{ion}), propagation (a_{prop}) and recombination (a_{rec}):

$$D^{mn}(t) = \sum_j D^{j,mn}(t), \quad (9.19)$$

with the summation covering each half cycle that contributes to the generation of the harmonic light, and

$$D^{j,mn}(t) = a_{rec}^m(\mathbf{p}_s, t) a_{prop}^{mn}(\mathbf{p}_s, t, t_{ion}^{(j)}) a_{ion}^n(\mathbf{p}_s, t_{ion}^{(j)}) \quad (9.20)$$

with

$$a_{ion}^n(\mathbf{p}_s, t_{ion}^{(j)}) = \sqrt{\frac{2\pi}{S''_{t_{ion}^{(j)}, t_{ion}^{(j)}}}} e^{-iS(\mathbf{p}_s, t_{ion}^{(j)}, t_{ion}^{(j)})} \Upsilon_n(\mathbf{p}_s + A(t_{ion}^{(j)})) \quad (9.21)$$

$$a_{prop}^{mn}(\mathbf{p}_s, t, t_{ion}^{(j)}) = \left[\frac{2\pi}{t - t_{ion}^{(j)}} \right]^{3/2} e^{-iS(\mathbf{p}_s, t, t_{ion}^{(j)})} a_{mn}(t, t_{ion}^{(j)}) \quad (9.22)$$

$$a_{rec}^m(\mathbf{p}_s, t) = d_m^*(\mathbf{p}_s + A(t)). \quad (9.23)$$

$t_{ion}^{(j)}$ is the time where ionization starts for each half cycle j , $t_{ion}^{\prime(j)} - t_{ion}^{(j)}$ is the duration of the tunnel ionization, and \mathbf{p}_s is the momentum of the continuum electron at $t_{ion}^{\prime(j)}$. $t_{ion}^{(j)}$, $t_{ion}^{\prime(j)}$ and \mathbf{p}_s are all obtained from the application of the saddle point method to Eq.9.11.

9.2 High high harmonic spectroscopy of CO₂

The imaging of molecular orbitals via high harmonic generation of aligned molecules was first theoretically proposed for H_2^+ by Lein and co-workers [242], and later experimentally realized for N₂ [90]. By varying the angles (θ) between the incident IR field and the molecular axis, one could use the high harmonic spectra to obtain a 3-D image of the dominant target molecular orbitals in the HHG process. Note however that the experiments are never performed under perfect alignment conditions, thus one typically has to consider a range of alignment angles ranging from $\pm 20^\circ$.

A series of experiments have pursued this method to visualize the molecular orbitals of CO₂ [91, 243, 238, 244, 245]. These experiments found a characteristic minimum in the HHG spectrum at $\theta = 0$, located between harmonics 19 and 35, depending on the specific experimental conditions, such as the intensity of the fundamental laser field driving the HHG process. If the minimum in the harmonic spectrum was associated with the structure of the recombination matrix elements, such a large variation of its position (about 20eV) was very surprising. The solution of this puzzle lies in the importance

of multiple ionization-recombination channels in the HHG spectra. At $\theta = 0^\circ$ ionization leaving the ion in the ground $X^2\Pi_g$ state is suppressed, and it is necessary to consider also ionization leaving the ion in the $B^2\Sigma_u^+$ state (see Fig.9.1 for a detailed description of the CO_2^+ in the equilibrium geometry considered in our calculation). Smirnova and co-workers have shown that at $\theta = 0^\circ$, the low energy part of the harmonic spectrum (from harmonic 17 to 29, depending on the laser intensity) is dominated by the channel opened by ionization leaving the ion in the $X^2\Pi_g$ state [91]. On the other hand, the high energy part of the spectrum is dominated by the channel opened by ionization leaving the ion in the $B^2\Sigma_u^+$ state. As HHG is a coherent process, the interference between these channels modulate the harmonic spectrum for harmonic order from 20 to 30. Indeed, in [91] it was demonstrated that the minimum observed in the experiments is directly related to the destructive interference of the HHG channels associated with these two ionic states, and is directly mapped to a specific time of recombination, where the relative phase between these channels is $\approx 3\pi$.

Here we present two theoretical calculations of the high harmonic spectra of CO_2 for $0 < \theta < 50^\circ$. We employ the formalism presented in the previous section to factorize the HHG process into ionization, propagation and recombination amplitudes. The two calculations presented here differ only by the method used in the evaluation of the photorecombination matrix elements: one uses the Eikonal approximation [70], while the other uses the *ab initio* UKRmol package. A comparison between the theoretical high harmonic spectra obtained with both calculations and the experiments of Levesque *et al.* [240] demonstrates the importance of using high quality photorecombination matrix elements for modeling the high harmonic spectra of CO_2 .

9.2.1 Wavefunctions of CO_2 and CO_2^+

The first step in our calculations is to determine the wavefunction of the neutral and ionic states involved in the HHG process. A set of molecular orbitals were constructed from an initial Gaussian basis set (cc-pVTZ) [182] using a state averaged CASSCF [183, 184] procedure with the quantum chemistry package MOLPRO [170]. 21 states of the ion and the ground state of the neutral were included in the averaging. We chose the state averaging to be predominantly weighted towards the neutral with a small (10%) component of ionic states to improve the description of the target. The wavefunction

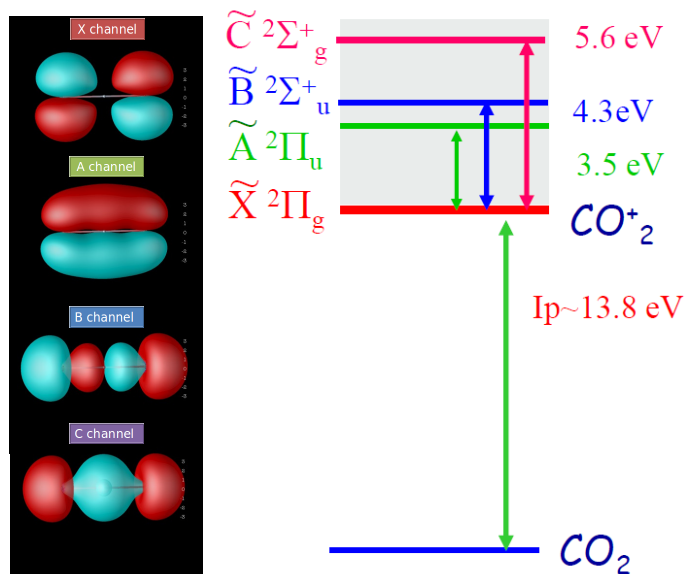


Figure 9.1: Dyson orbitals for ionization of ground state CO_2 leaving the ion in the ground ($X^2\Pi_g$), and first three excited states ($A^2\Pi_u, B^2\Sigma_u^+$, and $C^2\Sigma_g^+$).

of the neutral and the ionic states were then computed using a CI procedure with 6 electrons frozen in the core orbitals ($1-2\sigma_g, 1\sigma_u$) and the other electrons distributed over the ($3-5\sigma_g, 2-3\sigma_u, 1-2\pi_u, 1\pi_g$) valence orbitals.

9.2.2 Ionization

We include in the calculations ionization leaving the ion in the $X^2\Pi_g$, $A^2\Pi_u$, $B^2\Sigma_u^+$ and $C^2\Sigma_g^+$ states of CO_2^+ . In Fig.9.1 we show the Dyson orbitals for each of the ionic states considered, using the neutral and ionic state wavefunctions computed from the CI procedure detailed in the last section. As observed in previous experiments and calculations [91, 240], ionization leaving the ion in the $X^2\Pi_g$ state is suppressed along and perpendicular to the molecular axis. Therefore we expect contributions to the high harmonic spectra coming from the channels opened by ionization leaving the ion in the $A^2\Pi_u$ state at $\theta = 90^\circ$, and the $B^2\Sigma_u^+$, $C^2\Sigma_g^+$ states at $\theta = 0^\circ$. The ionization amplitude factors are then calculated using Eq.9.21.

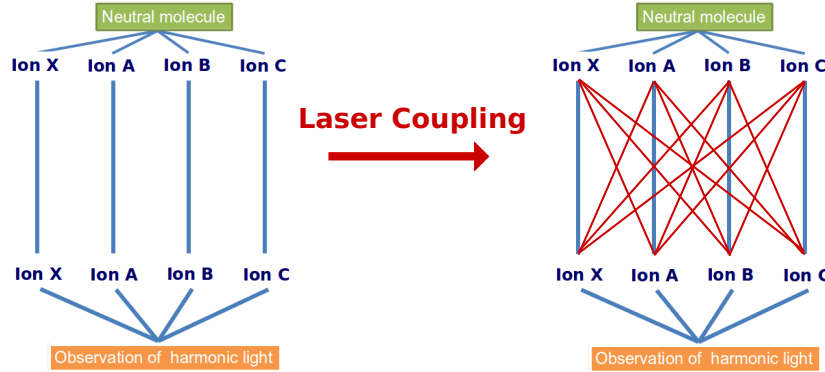


Figure 9.2: Direct channels corresponds to the case where the ionic states at the time of ionization and recombination are the same. Cross channels corresponds to the case where, due to the laser field, the ionic states are different at the time of ionization and recombination.

9.2.3 Propagation

In HHG, the strong IR field not only drives the continuum electron, but also couples different ionic states of CO_2^+ . Consequently if ionization leaves the ion in the state $X^2\Pi_g$, at the time of recombination, the wavefunction of the residual ion is a linear combination of all coupled states. We evaluate the population transfer coefficients (a_{mn}) by solving the Hamiltonian of the system, with the laser field included (Eq.9.9). In Fig.9.3 we plot the laser coupling induced by a field of $1.24 \times 10^{14} \text{W}/\text{cm}^2$, ($\lambda = 800\text{nm}$ and $\theta = 30^\circ$) for the $X^2\Pi_g$, $X^2\Pi_g$, $A^2\Pi_u$, $B^2\Sigma_u^+$ and $C^2\Sigma_g^+$ ionic states. We observe a strong coupling between the $X^2\Pi_g$ - $A^2\Pi_u$ states, and also the $B^2\Sigma_u^+$ - $C^2\Sigma_g^+$ states. We included in the HHG calculations direct (ionization and recombination occurs with the same residual ion) and cross channels (ionization and recombination occurs with different ions). The propagation amplitude for each of the channels are then evaluated with Eq.9.22.

9.2.4 Recombination

The scattering wavefunctions are given in terms of a close coupling expansion that included the 96 lowest energy states of CO_2^+ . The ionic states used in the close coupling expansion were generated with the CI target model discussed in section 9.2.1. The continuum orbitals used were generated with

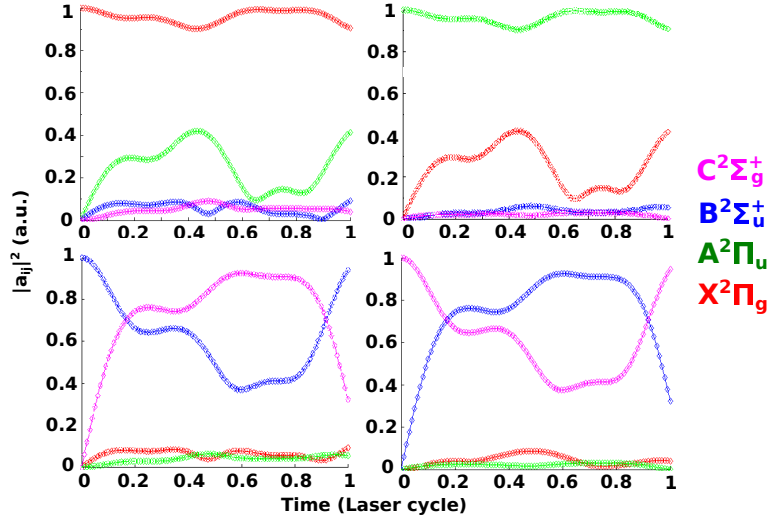


Figure 9.3: Laser coupling induced by a field of $1.24 \times 10^{14} \text{W/cm}^2$, $\lambda = 800 \text{nm}$ and at 30° in relation to the molecular axis for ionization leaving the ion in the $X^2\Pi_g$ (top left), $A^2\Pi_u$ (top right), $B^2\Sigma_u^+$ (bottom left) and $C^2\Sigma_g^+$ (bottom right) states. Time is given in relation to one laser cycle.

a Gaussian basis that spanned energies up to 50eV, and $l \leq 4$. The basis set were optimized for reproducing the wavefunction of the continuum electron up to a radius of 10 atomic units from the center of mass of the CO_2 molecule. At this radius, the inner region wavefunction was matched to the analytic asymptotic solutions of the system.

The Eikonal recombination matrix elements were obtained from [246]. These recombination matrix elements are similar to the ones used in [91] and neglect electronic correlation on the scattering wavefunction of the target.

9.2.5 High harmonic spectra

Using the codes of Smirnova [246], we could put together the ionization, propagation and recombination matrix elements for each of the direct/cross channels, and obtain the high harmonic spectra for CO_2 . The experimental data have imperfect alignment, which can be modelled by a $\cos^4 \theta$ or $\cos^6 \theta$ distribution. We averaged the theoretical high harmonic spectra with a $\cos^6 \theta$ distribution. In Fig.9.4, we show the experimental (first row), and the theoretical (second row, using the photorecombination matrix elements obtained

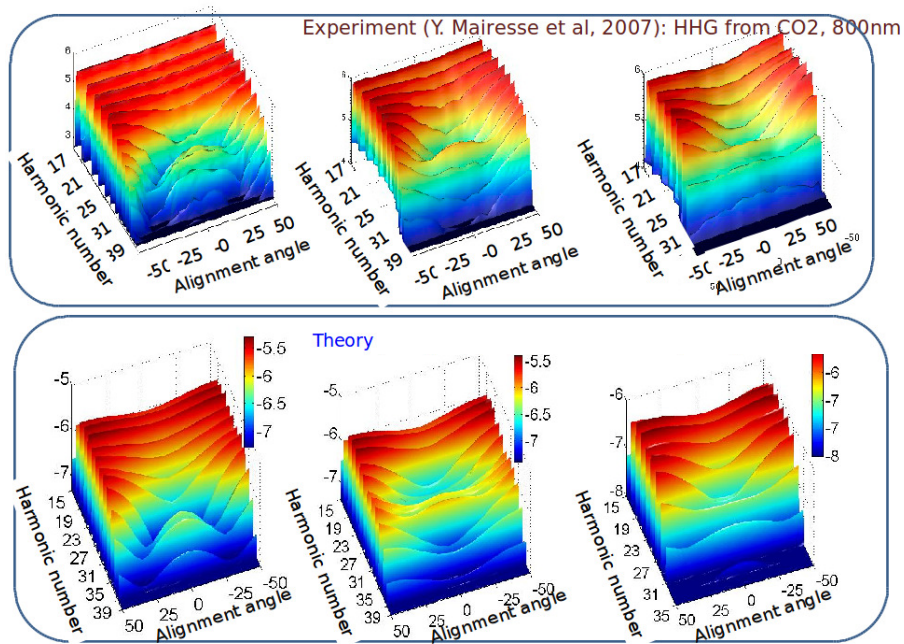


Figure 9.4: High harmonic spectra measured by Mairesse *et. al.* (top) [240] for a field intensity of $2.0 \times 10^{14} \text{W/cm}^2$ (left) $1.8 \times 10^{14} \text{W/cm}^2$ (middle) and $1.3 \times 10^{14} \text{W/cm}^2$ (right). In the bottom we present the theoretical high harmonic spectra, which uses the photorecombination matrix elements calculated with the UKRmol package.

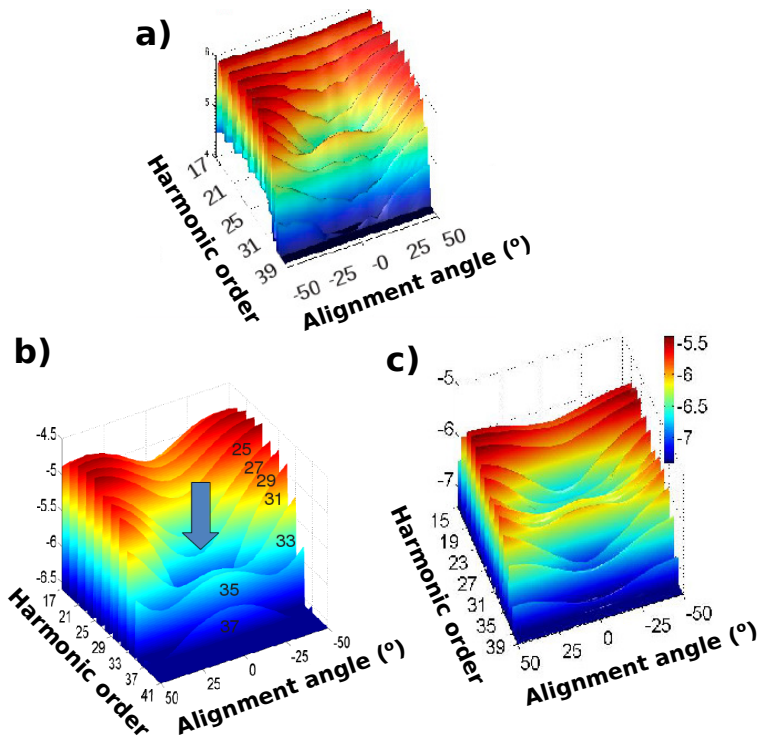


Figure 9.5: High harmonic spectra measured by Mairesse *et. al.*(a) for a field intensity of $1.8 \times 10^{14} W/cm^2$ [240]. In (b) and (c) we show the theoretical high harmonic spectra. In (b), the photorecombination matrix elements are calculated with the Eikonal approach, in (c) the photorecombination matrix elements are calculated with the UKRmol package.

from the UKRmol package) high harmonic spectra of CO₂ for laser intensities of $2 \times 10^{14} \text{W/cm}^2$ (left), $1.8 \times 10^{14} \text{W/cm}^2$ (middle) and $1.3 \times 10^{14} \text{W/cm}^2$ (right).

All main features observed experimentally are well reproduced by the calculation that used the recombination matrix elements calculated with the UKRmol package. On the other hand, the calculations using Eikonal recombination matrix elements (Fig.9.5b) exhibit some clear deficiencies: at harmonic 31 this calculation predicts a dip close to the alignment angle of 0° , while the experiment shows an island from harmonics 35 to 31; note that close to the alignment angle of 0° , Fig.9.5b has a minimum in several low order harmonics in clear contrast with the experimental data. These results stress the importance of using high quality recombination matrix elements in the calculations.

9.3 Observation window in HHG: an example on He

In [241], Pedatzur *et. al.* have measured the high harmonic spectra of Helium with a 2-color field scheme for probing the duration of the tunnel ionization process. In this experiment, a strong IR pulse induces tunnel ionization of a bound electron from the atomic target, and drives the free electron back to the parent ion, leading then to recombination and a subsequent attosecond burst. The interference between the attosecond burst at consecutive half cycles results in the emission of exclusively odd harmonics. A perturbative second harmonic pulse is then used to break the symmetry of the HHG process: while in a given cycle the tunnel ionization barrier is enhanced, in the consecutive cycle the barrier is suppressed. Varying the time-delay (ϕ) between the two fields, the different tunnelling times at consecutive half cycles can be mapped into the amplitude modulations in the high harmonic spectra. In [241], Pedatzur *et. al.* are particularly interested in measuring complex phase difference (σ) between consecutive half-cycles extracted from the modulations of the high harmonic spectra. In [241], the measured region of the high harmonic spectra overlaps with the doubly excited autoionizing resonances of Helium, which were already discussed in detail in chapter 8. However, the well known signatures of the autoionizing resonances, which induces abrupt phase and amplitude changes in the photorecombination of

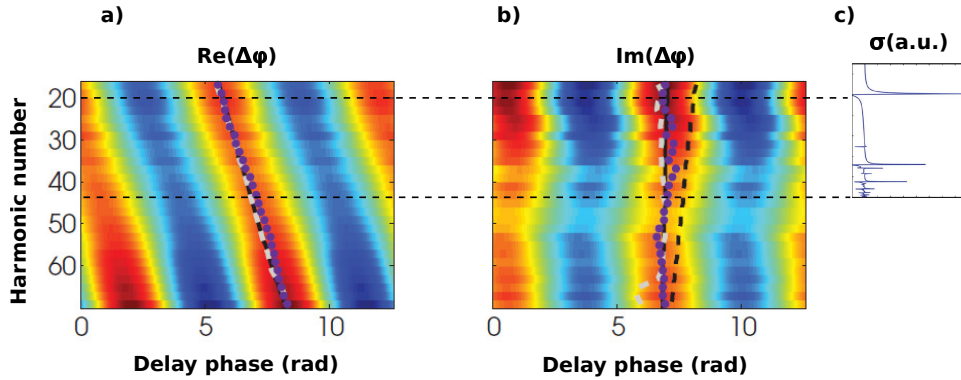


Figure 9.6: Complex phase difference (σ) for paths taken by the ionized electron at two consecutive half cycles, as a function of the delay between the strong and the perturbative field (ϕ). In a) and b) we plot the real and imaginary parts of σ respectively. In c), we plot the photorecombination cross sections of Helium. The energy axis of a), b) and c) coincides. Note that not signatures of the autoionizing resonances from the photorecombination cross section are observed in σ .

Helium, are not observed in the experimental data (see Fig.9.3). Using the calculations presented in chapter 8 for He, we investigate here the reason for the absence of any signature of the autoionizing resonances in the high harmonic spectra.

9.3.1 Observation window of the high harmonic light

A crucial reason is the time-gating of the XUV emission associated with the autoionizing resonances. Field-free, these resonances have far longer lifetimes than the duration of the XUV emission bursts which make up the harmonic spectrum. The origin of this temporal gating is the strong driving laser field, which not only reduces the lifetime of the weakly bound states by field ionization, but also suppresses the contribution of the 'bound' part of the auto-ionizing states due to the macroscopic effects of phase matching. Indeed, long-lived amplitude in the resonance acquires substantial intensity-dependent-phase, which is mapped onto the phase of the emitted light. Since the laser intensity is inhomogeneously distributed in the laser focus, large intensity-dependent phase leads to a spatially inhomogeneous phase-mask, which, in turn, leads to the strong divergence of the emitted light and sup-

presses constructive interference of the emission from different molecules in the forward direction, i.e., phase matching.

What will happen if we introduce a finite observation window into the emission, i.e. time-gate the emission? The experiment uses 40-fsec IR pulses. Our numerical simulations of the time-dependent Schrodinger equation show that high harmonic emission is limited to about 10-15 fsec time window near the center of the IR pulse. We therefore start with the very conservative simple analysis, and gate the photorecombination with the time-window of 12 fsec. Mathematically, we perform the convolution of photorecombination dipoles with the 12 fsec Gaussian window. This leads to the very substantial broadening of the resonances (compare blue and red curves in Fig.9.7a), virtually eliminating all but one resonance near 61 eV photon energy. However, such conservative analysis misses a key macroscopic aspect of high harmonic emission. In the time domain, high harmonic emission corresponds to very short bursts of XUV light that occur every half period of IR field (see for example the measurements of S. Haessler et al. [247], where the duration of such pulses has been measured experimentally for different orientations of N₂ molecule). The typical duration of an emission burst is about 300 asec. The result is not specific to the N₂ molecule, but is general as it has been shown by Mairesse et al. [248]. Due to phase matching, only the so-called short trajectories contribute to bright on-axis emission collected in the experiment. Long emission tails associated with long trajectories and multiple recollisions are strongly filtered out by propagation. This introduces even shorter observation window into the experiment. With calculations similar to Figure 2 repeated for 300 asec window, no traces of resonances are left (see Fig.9.7b).

9.4 Discussion

In this chapter we have applied the photorecombination matrix elements obtained with the UKRmol package to the investigation of HHG. We first demonstrated, using HHG from CO₂ as an example, the importance of using accurate photorecombination matrix elements in the HHG model, in order to accurately reproduce the experimental high harmonic spectra. Later we showed how the short window of observation of the HHG light results in a convolution of the recombination matrix elements, thus eliminating a any signature of the autoionizing resonances in the harmonic spectra. This later

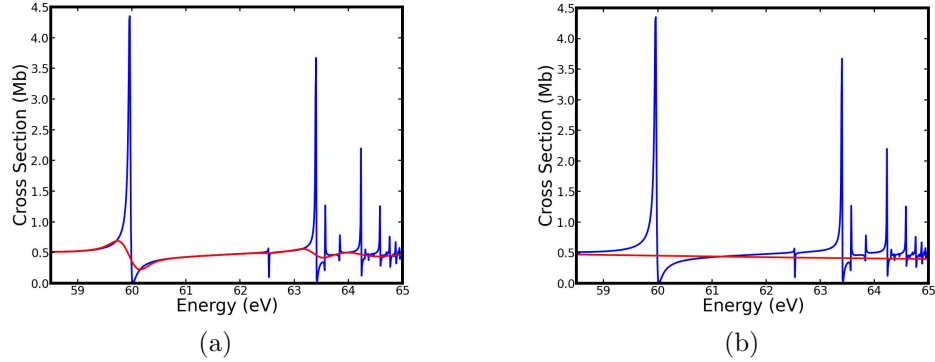


Figure 9.7: Photoionization cross section for He atom (blue curve) obtained by us using the ab-initio R-matrix method shows prominent resonance structure. Red curve corresponds to finite observation window of 12 fsec (a) and 300 asec (b). Virtually all resonances are eliminated, except for the one near 61 eV photon energy.

results was confirmed in the experiments of Pedatzur *et. al.* [241] on the high harmonic interferometry of He. The results presented in this chapter raises also demonstrates how accurate photorecombination matrix elements raises the standards of the theoretical description of the HHG process.

Chapter 10

Conclusions

In this thesis, we have used the multichannel R-Matrix method to calculate single photoionization of polyatomic molecules. The calculations were performed with the UKRmol package and required the implementation of the new modules CDENPROP and DIPELM, which extract photoionization observables from the electron-molecule scattering UKRmol codes.

In chapters 4 and 5 we explained in detail the equation and methods used in the implementation of CDENPROP and DIPELM. Both modules are now integrated to the UKRmol+ and Quante-mol-N packages.

We have successfully benchmarked the codes in chapter 6, by comparing the partial photoionization cross sections, photoelectron angular distributions, and asymmetry parameters obtained here with several other calculations and experiments. We have demonstrated that multichannel calculations that consistently include electronic correlation in both the bound (initial) and the scattering (final) states are necessary for a high quality description of the photoionization leaving the ion in certain excited molecular states, such as: (i) the photoionization from ground CO_2 leaving the ion in the $C^2\Sigma_g^+$, and (ii) photoionization of ground NO_2 leaving the ion in the $(2)^3B_1$ state. In case (i) we have shown that static exchange models tend to overestimate the amplitude of the shape resonances. In case (i), we have also demonstrated that a better agreement of theory with respect to the experiments can be obtained by increasing the number of target states included in the close coupling expansion. In case (ii), $(2)^3B_1$ is a satellite state in respect to ground state NO_2 . Therefore all signal observed in the cross sections comes from low order electronic configurations that plays a significant contribution in the CI description of this ionic state.

In chapter 7 we have explored the capability of the UKRmol+ codes to calculate the photoionization from the ground and first excited state of NO₂ leaving the ion in the (1)¹A' and (1)³A' states for several nuclear geometries. These are the first calculations over a large geometry range where electronic correlation is consistently included not only in the initial bound state, but also in the final ionic state, allowing us to precisely evaluate the probing (photoionization) step in TRPES. The photoionization dipoles obtained here could be in the future coupled to wavepacket propagation codes, in order to investigate the photoexcitation of NO₂ in regions of the reaction coordinates where non-adiabatic couplings either in the neutral or in the final ionic states becomes non-negligible, thus a CI description of the electronic configuration is necessary. Another possibility would be to use the photoionization dipoles in High Harmonic generation codes, in order to investigate the photoexcitation of NO₂ using high harmonic generation as a probing step. We have shown that observables such as partial photoionization cross sections, asymmetry parameters and PADs can be used for retrieving the dominant electronic configurations of the neutral and the ionic states.

In chapter 8 we have explored the effects of a weak static electric field in photoionization. The module STCFLD and a small adaptation to the propagation step in the outer region of the codes were implemented for the inclusion of the static field on the UKRmol. STCFLD could be used in the future for several applications, such as the inclusion of strong static fields to the UKRmol package, and also in time-dependent electron-scattering/photoionization calculations. We tested the codes by evaluating the effect of the field on the series of autoionizing resonances converging to the first excited states of H₂⁺ and He⁺. We show that the static field has a strong effect on the autoionizing resonances, inducing a stark shift and eventually a stark splitting of the resonances. The number of autoionizing resonances investigated could be increased if extra target states were included to better describe the polarization of the target system, a critical factor for near threshold ionization and electron scattering. In addition to the investigation of the dynamics of autoionizing resonances, our codes could be used to evaluate the effect of adiabatic alignment techniques in molecular frame photoelectron angular distribution experiments. Another interesting future application, would be also to compute tunnel ionization rates, which would requires static fields 3 orders of magnitude larger than the ones tested in chapter 8. Exterior complex scaling is a powerful approach, which could be used in the new developments, in the same fashion as proposed by Ken Taylor [235].

Finally in chapter 9 we applied our results to high harmonic generation. We first used the photorecombination matrix elements (time reversal of the photoionization dipoles) obtained for CO₂ at the equilibrium geometry and coupled it to the codes already previously developed by Smirnova [246] for generating the high harmonic spectra. An excellent agreement between calculations and experiments is obtained. Later we also analyze the experiments of Pedatzur *et. al.* on the high harmonic interferometry of Helium, and concluded that the absence of any signature of the autoionizing resonances in the harmonic spectra is fully consistent with the short window of observation of the emitted HHG light. The effect of this time-window is to convolute the photorecombination matrix elements with a certain spectral window, thus eliminating narrow autoionizing resonances from the spectra. In addition, we demonstrated how an accurate calculation of the photorecombination matrix elements using the R-Matrix methods raises the accuracy standards of the theoretical description of high harmonic spectroscopy.

In a future work, adaptations to extend the capability of UKRmol+ to calculate time dependent processes and collisions involving many electrons in the continuum would allow the investigation of a huge number of different physical effects such as the Auger effect, sequential ionization, multiphoton ionization; and it would also make it possible to self consistently calculate processes such as high harmonic generation (HHG) of polyatomic molecules. Another interesting branch of development is to extend the codes for using a B-spline continuum basis set. This would allow the increase of the R-Matrix box size and consequently enable the calculation of electron scattering and photoionization of larger polyatomic molecules.

Appendix A

A.1 Multipole expansion

In this section we derive an explicit expression for the coupling potentials in Eq.2.71. From the close coupling equations we have that the direct potential in the asymptotic limit (see Eq. 2.67 and Eq.5.13) is given by

$$V_{ii'}(r) = \langle S_{l_i}^{m_i}(\Omega_{N+1})\Phi_i | \sum_{p=1}^N \frac{1}{r_{p,N+1}} - \sum_{k=1}^{N_n} \frac{Z_k}{r_{k,N+1}} | S_{l_{i'}}^{m_{i'}}(\Omega_{N+1})\Phi_{i'} \rangle'. \quad (\text{A.1})$$

where Φ_i is the i^{th} ionic state, Z_k is the electronic charge of the k^{th} atom and the prime indicates that the integration is performed over all electronic coordinates except r_{N+1} . For convenience, we omit the dependency of the target states on the electronic coordinates $\mathbf{x}_1, \dots, \mathbf{x}_N$.

The Coulomb potential can be decomposed into a basis of Legendre polynomials

$$\frac{1}{r_{ii'}} = \sum_{\lambda=0}^{\infty} \frac{r_i^\lambda}{r_{i'}^{\lambda+1}} P_\lambda(\cos \theta) \quad (\text{A.2})$$

where $\cos \theta = \hat{\mathbf{r}}_i \cdot \hat{\mathbf{r}}_{i'}$ and $r_i > r_{i'}$. The first and second summation go over the N bound electrons and the N_n atomic nuclei of the target. Using Eq.A.2 we find that the first summation of Eq.A.1 becomes

$$\begin{aligned} & \langle S_{l_i}^{m_i}(\Omega_{N+1})\Phi_i | \sum_{p=1}^N \frac{1}{r_{p,N+1}} | S_{l_{i'}}^{m_{i'}}(\Omega_{N+1})\Phi_{i'} \rangle = \\ & \sum_{\lambda=0} \frac{1}{r^{\lambda+1}} \sum_{p=1}^N \langle S_{l_i}^{m_i}(\Omega_{N+1})\Phi_i | P_\lambda(\hat{\mathbf{r}}_i \cdot \hat{\mathbf{r}}_{i'}) r_p^\lambda | S_{l_{i'}}^{m_{i'}}(\Omega_{N+1})\Phi_{i'} \rangle. \end{aligned} \quad (\text{A.3})$$

The addition theorem for spherical harmonics allow us to decompose the Legendre polynomials into

$$P_l(\hat{\mathbf{r}}_i \cdot \hat{\mathbf{r}}_{i'}) = \sum_{m=-l}^l S_l^m(\hat{\mathbf{r}}_i) S_l^m(\hat{\mathbf{r}}_{i'}) \quad (\text{A.4})$$

Substituting Eq.A.4 in Eq.A.3 and factorizing the integration over the radial and angular coordinates

$$\begin{aligned} \langle S_{l_i}^{m_i}(\Omega_{N+1}) \Phi_i | \sum_{p=1}^N \frac{1}{r_{p,N+1}} | S_{l_{i'}}^{m_{i'}}(\Omega_{N+1}) \Phi_{i'} \rangle = \\ \sum_{\lambda=0}^{\infty} \sum_{m=-\lambda}^{\lambda} \frac{4\pi}{2\lambda+1} \frac{T_{ii'}^{\lambda m}}{r^{\lambda+1}} \langle S_{l_i}^{m_i} | S_{\lambda}^m | S_{l_{i'}}^{m_{i'}} \rangle \end{aligned} \quad (\text{A.5})$$

with

$$T_{ii'}^{\lambda m} = \sum_{p=1}^N \langle \Phi_i | S_{\lambda}^m | \Phi_{i'} \rangle. \quad (\text{A.6})$$

Following the same steps that lead to Eq.A.5 for the first summation in Eq.A.1, the second summation in Eq.A.1 is found to be

$$\begin{aligned} \langle S_{l_i}^{m_i}(\Omega_{N+1}) \Phi_i | \sum_{k=1}^{N_n} \frac{Z_k}{r_{k,N+1}} | S_{l_{i'}}^{m_{i'}}(\Omega_{N+1}) \Phi_{i'} \rangle = \\ - \langle \Phi_i | \Phi_{i'} \rangle \sum_{\lambda=0}^{\infty} \sum_{m=-\lambda}^{\lambda} \frac{4\pi}{2\lambda+1} \frac{1}{r^{\lambda+1}} \langle S_{l_i}^{m_i} | S_{\lambda}^m | S_{l_{i'}}^{m_{i'}} \rangle \sum_{k=1}^{N_n} Z_k S_{\lambda}^m(\hat{\mathbf{R}}_k) R_k^{\lambda} \end{aligned} \quad (\text{A.7})$$

Combining Eq.A.5 and Eq.A.7 we have

$$V_{ii'}(r) = \sum_{\lambda=0}^{\infty} \frac{\alpha_{ii'\lambda}}{r^{\lambda+1}} \quad (\text{A.8})$$

where

$$\alpha_{ii'\lambda} = \sum_{m=-\lambda}^{\lambda} \langle S_{l_i}^{m_i} | S_{\lambda}^m | S_{l_{i'}}^{m_{i'}} \rangle \frac{4\pi}{2\lambda+1} \left(T_{ii'}^{\lambda m} - \langle \Phi_i | \Phi_{i'} \rangle \sum_{k=1}^{N_n} Z_k S_{\lambda}^m(\hat{\mathbf{R}}_k) R_k^{\lambda} \right). \quad (\text{A.9})$$

The term $\langle S_{l_i}^{m_i} | S_{\lambda}^m | S_{l_{i'}}^{m_{i'}} \rangle$, which is simply an integral over three real spherical harmonics can be computed using the formulas presented in [249].

Appendix B

B.1 Adaptations to the UKRmol package

For an extensive discussion of the UKRmol codes we refer to [106] and references therein. Here we will focus exclusively on the parts of the codes that needs to be adapted for the inclusion of the static field.

Regarding the inner region, initially we proceed in the usual way and obtain the field free eigenvectors and eigenvalues with the module SCATCI, which diagonalizes the $N + 1$ electron field free Hamiltonian on the close coupling basis (Eq. 5.3). The new module STCFLD adds a static field of arbitrary strength to the codes, in the same fashion as described in the last section. STCFLD builds a super Hamiltonian matrix containing all the symmetries affected by the field, using the field free eigenvectors as basis. Consequently, the super-matrix will have the form given in Eq. 8.3, with the diagonal terms being directly read from SCATCI. The off-diagonal terms are obtained by first reading the dipoles between the field free scattering wavefunction (calculated by the module CDENPROP), and subsequently multiplying them by the static field vector. The super matrix is then diagonalized with a LAPACK routine and the Stark shifted eigenvectors ($\tilde{\Psi}^{st}$) are then transformed to the canonical basis.

Concerning the outer region, there are no major modifications, but two important adaptations: (i) the asymptotic channels of symmetry groups coupled by the field are brought together in the outer region close coupling expansion; and (ii) the field induced couplings on the asymptotic channels are included via the module STC-CPL, which simply adds the last term of Eq. 8.11 to the outer region Hamiltonian.

B.2 STCFLD organization and input data

The body of the module STCFLD is composed of the following routines:

- **READCIP** reads the eigenvectors for each of the symmetries involved.
- **ADDIAG** adds the field free eigenvalues to the super-matrix.
- **ADDNDP** reads the dipole transition moments calculated by the module CDENPROP, multiply them by the field strength and finally place them in their respective positions in the super-matrix.
- **QLDIAG** is a subroutine taken from **SCATCI**, which diagonalized the super-matrix using LAPACK built in functions.
- **DGEMM** is a LAPACK subroutine used for transforming the eigenvectors to the canonical basis.

The input data is given by the namelist DIAG and DIPCP, which carries the information regarding the construction of the diagonal and off-diagonal blocks of super-matrix respectively.

DIAG

- NDGB [2]: Number of symmetries included in the super-matrix.
- DGLU [25]: Logical unit containing the stacked field free eigenvalues and eigenvectors .
- DICTN ['z']: direction of the static field (x, y, z)

DIPCP

- TCPL [1]: total number of symmetry pairs coupled by the field.
- ICPL [1,2]: pairs coupled by the static field
- ODLU [24]: logical units containing the transition dipole moments for each of the pairs given in ICPL.
- LSFIELD [0]: static field strength in atomic units.

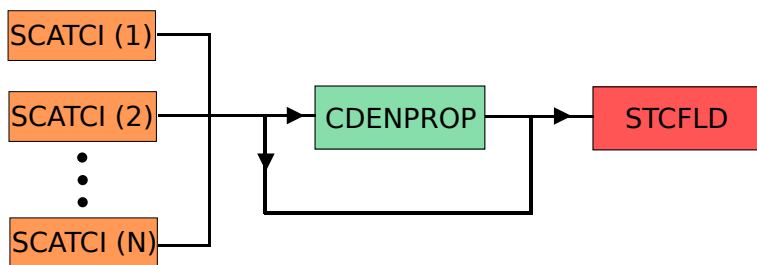


Figure B.1: Chart flow indicating the procedures for obtaining the Stark scattering wavefunctions.

Bibliography

- [1] Evans, M.G. and Polanyi, M. *Transactions of the Faraday Society*, 33(448), 1935.
- [2] Eyring, H. J. *The Journal of Chemical Physics*, 3(107), 1935.
- [3] Arrhenius, S. *Zeitschrift fr Physikalische Chemie*, 4(226), 1899.
- [4] Schawlow, A. L. et al. Masers and maser communications system. US Patent 2,929,922, 1960.
- [5] DeMaria, A.J. et al. *Picosecond Laser Pulses*, pages 11–70. Springer US, 1971.
- [6] Shank, C. V. and Ippen, E. P. Subpicosecond kilowatt pulses from a modelocked cw dye laser. *Applied Physics Letters*, 24(8):373–375, 1974.
- [7] Fork, R. L., Greene, B. I., and Shank, C. V. Generation of optical pulses shorter than 0.1 psec by colliding pulse mode locking. *Applied Physics Letters*, 38(9):671–672, 1981.
- [8] Fork, R. L. et al. Compression of optical pulses to six femtoseconds by using cubic phase compensation. *Opt. Lett.*, 12(7):483–485, 1987.
- [9] Sola, I. J. et al. Controlling attosecond electron dynamics by phase-stabilized polarization gating. *Nature Physics*, 2(5):319–322, 2006.
- [10] Burnett, N. H. et al. Harmonic generation in CO₂ laser target interaction. *Applied Physics Letters*, 31(3):172–174, 1977.
- [11] McPherson, A. et al. Studies of multiphoton production of vacuum-ultraviolet radiation in the rare gases. *J. Opt. Soc. Am. B*, 4(4):595–601, 1987.
- [12] Li, X. F. et al. Multiple-harmonic generation in rare gases at high laser intensity. *Physical Review A*, 39:5751–5761, 1989.
- [13] Ferray, M. et al. Multiple-harmonic conversion of 1064 nm radiation in rare gases. *Journal of Physics B: Atomic, Molecular and Optical Physics*, 21(3):L31, 1988.
- [14] Krausz, F. and Ivanov, M. Attosecond physics. *Reviews of Modern Physics*, 81:163–234, 2009.
- [15] Scherer, N. F. et al. Femtosecond photofragment spectroscopy of the reaction iodine cyanide (ICN) + atomic iodine. *The Journal of Physical Chemistry*, 89(24):5141–5143, 1985.

- [16] Zewail, A. H. Femtochemistry. Past, present, and future. *Pure and applied chemistry*, 72(12):2219–2231, 2000.
- [17] Rose, T. S., Rosker, M. J., and Zewail, A. H. Femtosecond realtime observation of wave packet oscillations (resonance) in dissociation reactions. *The Journal of Chemical Physics*, 88(10):6672–6673, 1988.
- [18] Asbury, J. B. et al. Ultrafast heterodyne detected infrared multidimensional vibrational stimulated echo studies of hydrogen bond dynamics. *Chemical Physics Letters*, 374(3–4):362–371, 2003.
- [19] Asbury, J. B. et al. Vibrational echo correlation spectroscopy probes of hydrogen bond dynamics in water and methanol. *Journal of Luminescence*, 107(1–4):271–286, 2004.
- [20] Khundkar, L. R. and Zewail, A. H. Picosecond photofragment spectroscopy. IV. Dynamics of consecutive bond breakage in the reaction $C_2F_4I_2C_2F_4 + 2I$. *The Journal of Chemical Physics*, 92(1):231–242, 1990.
- [21] Zewail, A. H. F. Laser Control and Femtosecond Dynamics. Femtosecond Dynamics of Reactions: Elementary Processes of Controlled Solvation. *Berichte der Bunsengesellschaft für physikalische Chemie*, 99(3):474–477, 1995.
- [22] Pedersen, S., Bañares, L., and Zewail, A. H. Femtosecond vibrational transitionstate dynamics in a chemical reaction. *The Journal of Chemical Physics*, 97(11):8801–8804, 1992.
- [23] Chachisvilis, M. and Zewail, A. H. Femtosecond Dynamics of Pyridine in the Condensed Phase: Valence Isomerization by Conical Intersections. *The Journal of Physical Chemistry A*, 103(37):7408–7418, 1999.
- [24] Katrib, A. et al. Surface electronic structure and isomerization reactions of alkanes on some transition metal oxides. *Surface Science*, 377–379:754–758, 1997.
- [25] Zhong, D. et al. Femtosecond dynamics of valence-bond isomers of azines: transition states and conical intersections. *Chemical Physics Letters*, 298(1–3):129–140, 1998.
- [26] Zewail, A. H. Femtochemistry: Recent Progress in Studies of Dynamics and Control of Reactions and Their Transition States. *The Journal of Physical Chemistry*, 100(31):12701–12724, 1996.
- [27] Leland, B. A. et al. Picosecond fluorescence studies on intramolecular photochemical electron transfer in porphyrins linked to quinones at two different fixed distances. *The Journal of Physical Chemistry*, 89(26):5571–5573, 1985.
- [28] Schanze, K. S. et al. Studies of intramolecular electron and energy transfer using the fac-(diimine)ReI(CO)₃ chromophore. *Coordination Chemistry Reviews*, 122(1–2):63–89, 1993.
- [29] Douhal, A, Kim, S. K., and Zewail, A. H. Femtosecond molecular dynamics of tautomerization in model base pairs. *Nature*, 378(6554):260–263, 1995.

- [30] Zewail, A. H. *Femtochemistry: ultrafast dynamics of the chemical bond*, volume 1. World Scientific, 1994.
- [31] Zewail, A. H. Femtochemistry: Atomic-scale dynamics of the chemical bond. *The Journal of Physical Chemistry A*, 104(24):5660–5694, 2000.
- [32] Hannaford, P. *Femtosecond laser spectroscopy*. Springer Science & Business Media, 2005.
- [33] Smith, J. M., Lakshminarayan, C., and Knee, J. L. Picosecond measurements of vibrational dynamics using pump–probe laser photoelectron spectroscopy. *The Journal of Chemical Physics*, 93(6):4475–4476, 1990.
- [34] Stolow, A. and Underwood, J. G. Time-resolved photoelectron spectroscopy of nonadiabatic dynamics in polyatomic molecules. *Advances in chemical physics*, 139:497, 2008.
- [35] Nisoli, M. et al. Highly efficient parametric conversion of femtosecond Ti: sapphire laser pulses at 1 kHz. *Optics letters*, 19(23):1973–1975, 1994.
- [36] Wilhelm, T, Piel, J, and Riedle, E. Sub-20-fs pulses tunable across the visible from a blue-pumped single-pass noncollinear parametric converter. *Optics letters*, 22(19):1494–1496, 1997.
- [37] Glowacki, J. M. et al. Time-resolved pump-probe experiments at the LCLS. *Opt. Express*, 18(17):17620–17630, 2010.
- [38] De Ninno, G. et al. Chirped Seeded Free-Electron Lasers: Self-Standing Light Sources for Two-Color Pump-Probe Experiments. *Physical Review Letters*, 110:064801, 2013.
- [39] Jiang, Y. H. et al. Temporal coherence effects in multiple ionization of N_2 via XUV pump-probe autocorrelation. *Physical Review A*, 82:041403, 2010.
- [40] Allaria E. et al. Two-colour pump-probe experiments with a twin-pulse-seed extreme ultraviolet free-electron laser. *Nature Communications*, 4, 2013.
- [41] Arbeiter, M. and Fennel, T. Rare-gas clusters in intense VUV, XUV and soft x-ray pulses: signatures of the transition from nanoplasma-driven cluster expansion to Coulomb explosion in ion and electron spectra. *New Journal of Physics*, 13(5):053022, 2011.
- [42] Jurek, Z., Oszlanyi, G., and Faigel, G. Imaging atom clusters by hard X-ray free-electron lasers. *EPL (Europhysics Letters)*, 65(4):491, 2004.
- [43] Thomas, H. et al. Explosions of Xenon Clusters in Ultraintense Femtosecond X-Ray Pulses from the LCLS Free Electron Laser. *Physical Review Letters*, 108:133401, 2012.
- [44] Landers, A. et al. Photoelectron Diffraction Mapping: Molecules Illuminated from Within. *Physical Review Letters*, 87:013002, 2001.

- [45] Boll, R. et al. Femtosecond photoelectron diffraction on laser-aligned molecules: Towards time-resolved imaging of molecular structure. *Physical Review A*, 88:061402, 2013.
- [46] Rolles, D. et al. Femtosecond x-ray photoelectron diffraction on gas-phase dibromobenzene molecules. *Journal of Physics B: Atomic, Molecular and Optical Physics*, 47(12):124035, 2014.
- [47] Sorokin, A. A. et al. Multi-photon ionization of molecular nitrogen by femtosecond soft x-ray FEL pulses. *Journal of Physics B: Atomic, Molecular and Optical Physics*, 39(14):L299, 2006.
- [48] Sato, T. et al. Dissociative two-photon ionization of N₂ in extreme ultraviolet by intense self-amplified spontaneous emission free electron laser light. *Applied Physics Letters*, 92(15):–, 2008.
- [49] Jiang, Y. H. et al. Few-Photon Multiple Ionization of N₂ by Extreme Ultraviolet Free-Electron Laser Radiation. *Physical Review Letters*, 102:123002, 2009.
- [50] Jiang, Y. H. et al. EUV-photon-induced multiple ionization and fragmentation dynamics: from atoms to molecules. *Journal of Physics B: Atomic, Molecular and Optical Physics*, 42(13):134012, 2009.
- [51] Jiang, Y. H. et al. Tracing direct and sequential two-photon double ionization of D₂ in femtosecond extreme-ultraviolet laser pulses. *Physical Review A*, 81:021401, 2010.
- [52] Pedersen, H. B. et al. Crossed Beam Photodissociation Imaging of HeH⁺ with Vacuum Ultraviolet Free-Electron Laser Pulses. *Physical Review Letters*, 98:223202, 2007.
- [53] Pedersen, H. B. et al. Neutral and charged photofragment coincidence imaging with soft x rays on molecular ion beams: Breakup of H₃O⁺ at 13.5 nm. *Physical Review A*, 80:012707, 2009.
- [54] Lammich, L. et al. Fragmentation Pathways of H⁺(H₂O)₂ after Extreme Ultraviolet Photoionization. *Physical Review Letters*, 105:253003, 2010.
- [55] Chapman H. N. et al. Femtosecond X-ray protein nanocrystallography. *Nature*, 470(7332):73–77, 2011.
- [56] Neutze, R. et al. Potential for biomolecular imaging with femtosecond X-ray pulses. *Nature*, 406(6797):752–757, 2000.
- [57] Buth, C. et al. High-order harmonic generation enhanced by XUV light. *Optics letters*, 36(17):3530–3532, 2011.
- [58] Leeuwenburgh, J. et al. High-Order Harmonic Generation Spectroscopy of Correlation-Driven Electron Hole Dynamics. *Physical Review Letters*, 111:123002, 2013.
- [59] Bauer, M. et al. Direct observation of surface chemistry using ultrafast soft-X-ray pulses. *Physical Review Letters*, 87(2):025501, 2001.

- [60] Sorensen, S. L. et al. Femtosecond pump-probe photoelectron spectroscopy of predissociative Rydberg states in acetylene. *The Journal of Chemical Physics*, 112(18):8038–8042, 2000.
- [61] Nugent-Glandorf, L. et al. Ultrafast time-resolved soft x-ray photoelectron spectroscopy of dissociating Br₂. *Physical Review Letters*, 87(19):193002, 2001.
- [62] Wernet, P. et al. Real-time evolution of the valence electronic structure in a dissociating molecule. *Physical Review Letters*, 103(1):013001, 2009.
- [63] Liénard, A. La théorie de Lorentz et celle de Larmor. *Éclairage électrique*, 16:320–334, 1898.
- [64] Eland, J. H. D. *Photoelectron spectroscopy*. Butterworth & Co, second edition, 1984.
- [65] Margaritondo, G. The evolution of a dedicated synchrotron light source. *Physics today*, 61(5):37–43, 2008.
- [66] Schmöser, P., Dohlus, M., and Dohlus, J. *Self Amplified Spontaneous Emission*, volume 229 of *Springer Tracts in Modern Physics*, pages 103–120. Springer Berlin Heidelberg, 2009.
- [67] Franken, P. A. et al. Generation of Optical Harmonics. *Physical Review Letters*, 7:118–119, 1961.
- [68] Kleinman, D. A. Theory of Second Harmonic Generation of Light. *Physical Review*, 128:1761–1775, 1962.
- [69] Boyd, R. W. *Nonlinear optics*. Academic press, 2003.
- [70] Smirnova, O. and Ivanov, M. *Attosecond and XUV Physics*. Wiley-VCH Verlag GmbH & Co. KGaA, 2014.
- [71] P. B. Corkum. Plasma perspective on strong field multiphoton ionization. *Physical Review Letters*, 71(13):1994, 1993.
- [72] Lewenstein, M. et al. Theory of high-harmonic generation by low-frequency laser fields. *Physical Review A*, 49(3):2117, 1994.
- [73] Becker, W., Long, S., and McIver, J. K. Modeling harmonic generation by a zero-range potential. *Physical Review A*, 50(2):1540, 1994.
- [74] Paul, P. M. et al. Observation of a train of attosecond pulses from high harmonic generation. *Science*, 292(5522):1689–1692, 2001.
- [75] Muller, H. G. Reconstruction of attosecond harmonic beating by interference of two-photon transitions. *Applied Physics B*, 74(1):s17–s21, 2002.
- [76] Caillat, J. et al. Attosecond resolved electron release in two-color near-threshold photoionization of N₂. *Physical Review Letters*, 106(9):093002, 2011.
- [77] Mairesse, Y. and Quéré, F. Frequency-resolved optical gating for complete reconstruction of attosecond bursts. *Physical Review A*, 71(1):011401, 2005.

- [78] Sansone, G. et al. Isolated single-cycle attosecond pulses. *Science*, 314(5798):443–446, 2006.
- [79] Chini, M. et al. Characterizing ultrabroadband attosecond lasers. *Optics express*, 18(12):13006–13016, 2010.
- [80] Bertrand, J. B. et al. Linked attosecond phase interferometry for molecular frame measurements. *Nature Physics*, 9(3):174–178, 2013.
- [81] Itatani, J. et al. Attosecond Streak Camera. *Physical Review Letters*, 88:173903, 2002.
- [82] Kitzler, M. et al. Quantum theory of attosecond XUV pulse measurement by laser dressed photoionization. *Physical Review Letters*, 88(17):173904, 2002.
- [83] Schultze, M. et al. Powerful 170-attosecond XUV pulses generated with few-cycle laser pulses and broadband multilayer optics. *New Journal of Physics*, 9(7):243, 2007.
- [84] Goulielmakis, E. et al. Attosecond control and measurement: lightwave electronics. *Science*, 317(5839):769–775, 2007.
- [85] Drescher, M. et al. Time-resolved atomic inner-shell spectroscopy. *Nature*, 419(6909):803–807, 2002.
- [86] Goulielmakis, E., , et al. Direct measurement of light waves. *Science*, 305(5688):1267–1269, 2004.
- [87] Goulielmakis, E. et al. Isolated 170 as Pulse Generation in the XUV. *Acta Physica Polonica Series A*, 112(5):751, 2007.
- [88] Sansone, G. et al. Isolated Single-Cycle Attosecond Pulses. *Science*, 314(5798):443–446, 2006.
- [89] Kling, M. F. and Vrakking, M JJ. Attosecond electron dynamics. *Annual Review of Physical Chemistry.*, 59:463–492, 2008.
- [90] Itatani J. et al. Tomographic imaging of molecular orbitals. *Nature*, 432(7019):867–871, 2004.
- [91] Smirnova O. et al. High harmonic interferometry of multi-electron dynamics in molecules. *Nature*, 460(7258):972–977, 2009.
- [92] Uiberacker M. et al. Attosecond real-time observation of electron tunnelling in atoms. *Nature*, 446(7136):627–632, 2007.
- [93] Pfeiffer, A. N. et al. Attoclock reveals natural coordinates of the laser-induced tunnelling current flow in atoms. *Nature Physics*, 8(1):76–80, 2012.
- [94] Pfeiffer, A. N. et al. Recent attoclock measurements of strong field ionization. *Chemical Physics*, 414:84–91, 2013.
- [95] Weger, M. et al. Transferring the attoclock technique to velocity map imaging. *Optics express*, 21(19):21981–21990, 2013.

- [96] Torlina, L. et al. Interpreting attoclock measurements of tunnelling times. *Nature Physics*, 11(6):503–508, 2015.
- [97] Keldysh, L. V. Ionization in the field of a strong electromagnetic wave. *Soviet Physics JETP*, 20(5):1307–1314, 1965.
- [98] Ivanov, M. Yu, Spanner, M., and Smirnova, O. Anatomy of strong field ionization. *Journal of Modern Optics*, 52(2-3):165–184, 2005.
- [99] Reiss, H. R. Unsuitability of the Keldysh parameter for laser fields. *Physical Review A*, 82(2):023418, 2010.
- [100] Burke, P. G. *R-Matrix theory of atomic collisions*. Springer, 2011.
- [101] Atkins, P. W. and Friedman, R. S. *Molecular Quantum Mechanics*, 3rd Edition. Oxford University Press.
- [102] Mcweeny, R. *Quantum mechanics: methods and basic applications*. 1ed. Oxford, New York, Pergamon Press, 1973.
- [103] Lucchese, R. R. Effects of interchannel coupling on the photoionization cross sections of carbon dioxide. *The Journal of Chemical Physics*, 92(7):4203–4211, 1990.
- [104] De Francesco, R., Stener, M., and Fronzoni, G. TDDFT Calculations of NEXAFS Spectra of Model Systems for SO₂ Adsorbed on the MgO (100) Surface. *The Journal of Physical Chemistry C*, 111(36):13554, 2007.
- [105] Ruberti, M., Averbukh, V., and Decleva, P. B-spline algebraic diagrammatic construction: Application to photoionization cross-sections and high-order harmonic generation. *The Journal of chemical physics*, 141(16):164126, 2014.
- [106] Tennyson, J. Electron–molecule collision calculations using the R-matrix method. *Physics Reports*, 491(2–3):29–76, 2010.
- [107] Faure, A. et al. GTOBAS: fitting continuum functions with Gaussian-type orbitals. *Computer Physics Communications*, 144(2):224–241, 2002.
- [108] Taylor, J. R. *Scattering theory: The Quantum Theory of Nonrelativistic Collisions*. Dover, 2nd edition edition, 2012.
- [109] Bloch, C. Une formulation unifiée de la théorie des réactions nucléaires. *Nuclear Physics*, 4(0):503–528, 1957.
- [110] Buttle, P. J. A. Solution of Coupled Equations by R-Matrix Techniques. *Physical Review*, 160:719–729, 1967.
- [111] Hazi, A. U. Behavior of the eigenphase sum near a resonance. *Physical Review A*, 19:920–922, 1979.
- [112] Breit, G. and Wigner, E. Capture of slow neutrons. *Physical Review*, 49:519–531, 1936.
- [113] Combes, J.-M., Duclos, P., Klein, M., and Seiler, R. The shape resonance. *Communications in Mathematical Physics*, 110(2):215–236, 1987.

- [114] Mayer, I. Simple Theorems, Proofs, and Derivations in Quantum Chemistry. 1943.
- [115] <https://bse.pnl.gov/bse/portal>.
- [116] Bunker P. R. and P. Jensen. *Molecular symmetry and spectroscopy*. Academic Press, 1979.
- [117] Reid, K. L. Photoelectron Angular Distributions. *Annual Review of Physical Chemistry*, 54(1):397–424, 2003.
- [118] Yeh, J. J. and Lindau, I. Atomic subshell photoionization cross sections and asymmetry parameters: $1 \leq z \leq 103$. *Atomic data and nuclear data tables*, 32(1):1–155, 1985.
- [119] Dill, D. Resonances in Photoelectron Angular Distributions. *Physical Review A*, 7:1976–1987, 1973.
- [120] Southworth, S. H., et al. Channel coupling and shape resonance effects in the photoelectron angular distributions of the $3\sigma_g^{-1}$ and $2\sigma_u^{-1}$ channels of N_2 . *Physical Review A*, 33:1020–1023, 1986.
- [121] Bellm, S. M. and Reid, K. L. Reevaluation of the Use of Photoelectron Angular Distributions as a Probe of Dynamical Processes: Strong Dependence of Such Distributions from S_1 Paradifluorobenzene on Photoelectron Kinetic Energy. *Physical Review Letters*, 91:263002, 2003.
- [122] Stapelfeldt, H. and Seideman, T. *Colloquium* : Aligning molecules with strong laser pulses. *Reviews of Modern Physics*, 75:543–557, 2003.
- [123] Williams, J. B. et al. Imaging Polyatomic Molecules in Three Dimensions Using Molecular Frame Photoelectron Angular Distributions. *Physical Review Letters*, 108:233002, 2012.
- [124] Plésiat, E. et al. Relationship between polarization-averaged molecular-frame photoelectron angular distributions and geometry. *Physical Review A*, 88:063409, 2013.
- [125] Hansen, J. L. et al. Time-resolved photoelectron angular distributions from strong-field ionization of rotating naphthalene molecules. *Physical Review Letters*, 106(7):073001, 2011.
- [126] Rouzée, A. et al. Imaging the electronic structure of valence orbitals in the XUV ionization of aligned molecules. *Journal of Physics B: Atomic, Molecular and Optical Physics*, 47(12):124017, 2014.
- [127] Böwering, N. et al. Asymmetry in Photoelectron Emission from Chiral Molecules Induced by Circularly Polarized Light. *Physical Review Letters*, 86:1187–1190, 2001.
- [128] Tsubouchi, M. et al. Photoelectron Imaging on Time-Dependent Molecular Alignment Created by a Femtosecond Laser Pulse. *Physical Review Letters*, 86:4500–4503, 2001.
- [129] Godehusen, K. et al. A complete photoionization experiment with polarized atoms using magnetic dichroism and phase tilt measurements. *Physical Review A*, 58:R3371–R3374, 1998.

- [130] Motoki, S. et al. Complete photoionization experiment in the region of the $2g$ shape resonance of the N_2 molecule. *Journal of Physics B: Atomic, Molecular and Optical Physics*, 35(18):3801, 2002.
- [131] Reid, K. L., Leahy, D. J., and Zare, R. N. Complete description of molecular photoionization from circular dichroism of rotationally resolved photoelectron angular distributions. *Physical Review Letters*, 68:3527–3530, 1992.
- [132] Cooper, J. and Zare, R. N. Angular Distribution of Photoelectrons. *The Journal of Chemical Physics*, 48(2):942–943, 1968.
- [133] Hall, J. L. and Siegel, M. W. Angular Dependence of the Laser Photodetachment of the Negative Ions of Carbon, Oxygen, and Hydrogen. *The Journal of Chemical Physics*, 48(2):943–945, 1968.
- [134] Brink, D. M. and Satchler, G. R. *Angular momentum*. Clarendon Press, Oxford University Press, 1993.
- [135] Breit, G. and Bethe, H. A. Ingoing Waves in Final State of Scattering Problems. *Physical Review*, 93:888–890, 1954.
- [136] Fano, U. and Dill, D. Angular momentum transfer in the theory of angular distributions. *Physical Review A*, 6(1):185, 1972.
- [137] Suzuki, T. and Whitaker, B. J. Non-adiabatic effects in chemistry revealed by time-resolved charged-particle imaging. *International Reviews in Physical Chemistry*, 20(3):313–356, 2001.
- [138] Boll, R. et al. Imaging molecular structure through femtosecond photoelectron diffraction on aligned and oriented gas-phase molecules. *Faraday Discuss.*, 171:57–80, 2014.
- [139] Teramoto, T. et al. New approach for a complete experiment: $C1s$ photoionization in CO_2 molecules. *Journal of Physics B: Atomic, Molecular and Optical Physics*, 40(16):F241, 2007.
- [140] Geßner, O. et al. $4\sigma^{-1}$ Inner Valence Photoionization Dynamics of NO Derived from Photoelectron-Photoion Angular Correlations. *Physical Review Letters*, 88:193002, 2002.
- [141] Motoki, S. et al. Direct Probe of the Shape Resonance Mechanism in $2\sigma_g$ -Shell Photoionization of the N_2 Molecule. *Physical Review Letters*, 88:063003, 2002.
- [142] Kettunen, J. A. et al. Dissociation of As_4 clusters following valence photoionization and $3d$ core excitation. *Physical Review A*, 86:023201, 2012.
- [143] Nevo, I. et al. Laser-induced 3D alignment and orientation of quantum state-selected molecules. *Physical Chemistry Chemical Physics*, 11:9912–9918, 2009.
- [144] Pentlehner, D. et al. Laser-induced adiabatic alignment of molecules dissolved in helium nanodroplets. *Physical Review A*, 87:063401, 2013.

- [145] Nielsen, J. H. et al. Making the Best of Mixed-Field Orientation of Polar Molecules: A Recipe for Achieving Adiabatic Dynamics in an Electrostatic Field Combined with Laser Pulses. *Physical Review Letters*, 108:193001, 2012.
- [146] Omiste, J. J. et al. Theoretical description of adiabatic laser alignment and mixed-field orientation: the need for a non-adiabatic model. *Physical Chemistry Chemical Physics*, 13:18815–18824, 2011.
- [147] Ghafur Omair et al. Impulsive orientation and alignment of quantum-state-selected NO molecules. *Nature Physics*, 5(4):289–293, 2009.
- [148] Zeng, G. et al. Field-free molecular alignment and its application. *Laser Physics*, 19(8):1691–1696.
- [149] Benko, C. et al. Cavity-Enhanced Field-Free Molecular Alignment at a High Repetition Rate. *Physical Review Letters*, 114:153001, 2015.
- [150] Loriot, V. et al. Laser-induced field-free alignment of the OCS molecule. *Journal of Physics B: Atomic, Molecular and Optical Physics*, 40(12):2503, 2007.
- [151] Lucchese, R R et al. Molecular frame and recoil frame angular distributions in dissociative photoionization of small molecules. *Journal of Physics: Conference Series*, 141(1):012009, 2008.
- [152] Bomme, C. et al. Molecular-frame photoelectron angular distribution imaging studies of OCS S1s photoionization. *Journal of Physics B: Atomic, Molecular and Optical Physics*, 45(19):194005, 2012.
- [153] Wigner, E. P. and Eisenbud, L. Higher Angular Momenta and Long Range Interaction in Resonance Reactions. *Physical Review*, 72:29–41, 1947.
- [154] Lane, A. M. and Thomas, R. G. R-Matrix Theory of Nuclear Reactions. *Reviews of Modern Physics*, 30:257–353, 1958.
- [155] Blatt, J. M. and Weisskopf V.F. *Theoretical Nuclear Physics*. Wiley, New York, NY, 1952.
- [156] Burke, P G, Hibbert, A, and Robb, W D. Electron scattering by complex atoms. *Journal of Physics B: Atomic and Molecular Physics*, 4(2):153, 1971.
- [157] Noble C.J. and Nesbet R.K. CFASYM, a program for the calculation of the asymptotic solutions of the coupled equations of electron collision theory. *Computer Physics Communications*, 33(4):399–411, 1984.
- [158] Sanz, A. G. et al. An investigation into electron scattering from pyrazine at intermediate and high energies. *The Journal of Chemical Physics*, 139(18):–, 2013.
- [159] Mašín, Z. and Gorfinkiel, J. D. Shape and core excited resonances in electron collisions with diazines. *The Journal of Chemical Physics*, 137(20):–, 2012.
- [160] Sieradzka A. et al. Electron Scattering from Pyridine. *The Journal of Physical Chemistry A*, 118(33):6657–6663, 2014.

- [161] Blanco, M. A., Flrez, M., and Bermejo, M. Evaluation of the rotation matrices in the basis of real spherical harmonics. *Journal of Molecular Structure (THEOCHEM)*, 419(13):1927, 1997.
- [162] Sarpal, B. K. et al. Bound states using the R-matrix method: Rydberg states of HeH. *Journal of Physics B: Atomic, Molecular and Optical Physics*, 24(17):3685, 1991.
- [163] Tashiro, M. Application of the R-matrix method to photoionization of molecules. *Journal of Chemical Physics*, 132(13):134306, 2010.
- [164] J. Tennyson. A new algorithm for Hamiltonian matrix construction in electron-molecule collision calculations. *Journal of Physics B: Atomic and Molecular Physics*, 29(9):1817, 1996.
- [165] Medisauskas, L. et al. Submitted to Physical Review Letters.
- [166] Marr, G V et al. Angular distribution of photoelectrons from free molecules of N₂ and CO as a function of photon energy. *Journal of Physics B: Atomic and Molecular Physics*, 12(1):43, 1979.
- [167] Plummer, E. W. et al. Partial photoionization cross sections of N₂ and CO using synchrotron radiation. *Physical Review A*, 15:2339–2355, 1977.
- [168] Samson, J A R, Haddad, G N, and Gardner, J L. Total and partial photoionization cross sections of N₂ from threshold to 100 Å. *Journal of Physics B: Atomic and Molecular Physics*, 10(9):1749, 1977.
- [169] Grade, M. et al. Electron Impact Investigation of the Molecules SeS(g) and TeSe(g) Under High-Temperature Equilibrium Conditions. *Berichte der Bunsengesellschaft für physikalische Chemie*, 87(4):355–361, 1983.
- [170] Werner, H.-J. et al. MOLPRO, version 2012.1, a package of ab initio programs, 2012.
- [171] Baltzer, P. et al. Inner-valence states of N₂⁺ studied by uv photoelectron spectroscopy and configuration-interaction calculations. *Physical Review A*, 46:5545–5553, 1992.
- [172] Little, D. A. and Tennyson, J. An ab initio study of singlet and triplet Rydberg states of N₂. *Journal of Physics B: Atomic, Molecular and Optical Physics*, 46(14):145102, 2013.
- [173] Brigg, W. J. et al. Calculated photoionization cross sections using Quantemol-N. *Japanese Journal of Applied Physics*, 54(6S2):06GA02, 2015.
- [174] Lucchese, R. R. and McKoy, V. Studies of differential and total photoionization cross sections of carbon dioxide. *Physical Review A*, 26:1406–1418, 1982.
- [175] Lucchese, R. R. and McKoy, V. Vibrational effects in the photoionization shape resonance leading to the C²Σ_g⁺ state of CO₂⁺. *Physical Review A*, 26:1992–1996, 1982.
- [176] Roy P. et al. On the photoionization shape resonance associated to the C²Σ₂⁺ state of CO₂⁺. *Chemical Physics Letters*, 109(6):607–614, 1984.

- [177] Kelkensberg, F. et al. XUV ionization of aligned molecules. *Physical Review A*, 84:051404, 2011.
- [178] Samson, J. A. R. and Gardner, J. L. Fluorescence excitation and photoelectron spectra of CO₂ induced by vacuum ultraviolet radiation between 185 and 716 Angstroms. *Journal of Geophysical Research*, 78(19):3663–3667, 1973.
- [179] Gustafsson, T. et al. Partial photoionization cross sections of CO₂ between 20 and 40 eV studied with synchrotron radiation. *Physical Review A*, 17:175–181, 1978.
- [180] Siggel, M. R. F. et al. Shaperesonanceenhanced continuum–continuum coupling in photoionization of CO₂. *The Journal of Chemical Physics*, 99(3):1556–1563, 1993.
- [181] Brion, C.E. and Tan, K.H. Partial oscillator strengths for the photoionization of N₂O and CO₂ (20–60 eV). *Chemical Physics*, 34(2):141–151, 1978.
- [182] Dunning, T. H. Gaussian basis sets for use in correlated molecular calculations. I. The atoms boron through neon and hydrogen. *The Journal of Chemical Physics*, 90(2):1007–1023, 1989.
- [183] Knowles P. J. and Werner, H. J. An efficient second-order MC SCF method for long configuration expansions. *Chemical Physics Letters*, 115(3):259–267, 1985.
- [184] Werner, H. J. and Knowles, P. J. A second order multiconfiguration SCF procedure with optimum convergence. *The Journal of Chemical Physics*, 82(11):5053–5063, 1985.
- [185] Gorfinkiel, J. D. and Tennyson, J. Electron impact ionization of small molecules at intermediate energies: the molecular R -matrix with pseudostates method. *Journal of Physics B: Atomic, Molecular and Optical Physics*, 38(11):1607, 2005.
- [186] Friedrich, B. and Herschbach, D. Alignment and Trapping of Molecules in Intense Laser Fields. *Physical Review Letters*, 74:4623–4626, 1995.
- [187] Kumar, G. R. et al. Molecular pendular states in intense laser fields. *Physical Review A*, 53:3098–3102, 1996.
- [188] Seideman, T. Revival Structure of Aligned Rotational Wave Packets. *Physical Review Letters*, 83:4971–4974, 1999.
- [189] Zeng, G. et al. Field-free molecular alignment and its application. *Laser Physics*, 19(8):1691–1696, 2009.
- [190] Wilkinson, I. and B. J. Whitaker. Some remarks on the photodynamics of NO₂. *Annual Reports on the Progress of Chemistry, Section C: Physical Chemistry*, 106:274–304, 2010.
- [191] Wörner H. J. et al. Conical Intersection Dynamics in NO₂ Probed by Homodyne High-Harmonic Spectroscopy. *Science*, 334(6053):208–212, 2011.
- [192] Ruf, H. et al. High-harmonic transient grating spectroscopy of NO₂ electronic relaxation. *The Journal of Chemical Physics*, 137(22):–, 2012.
- [193] M. Richter et al. *arXive preprint* . 2015.

- [194] Mairesse, Y. et al. High Harmonic Spectroscopy of Multichannel Dynamics in Strong-Field Ionization. *Physical Review Letters*, 104:213601, 2010.
- [195] Smirnova, O. and Ivanov, M. Multielectron High Harmonic Generation: simple man on a complex plane, chapter 7 in *Attosecond and XUV physics*, edited by T. Schultz and M. Vrakking . Wiley, 2013.
- [196] Le, A. T. et al. Quantitative rescattering theory for high-order harmonic generation from molecules. *Physical Review A*, 80:013401, 2009.
- [197] Mclean, A. D. and Chandler, G. S. Contracted Gaussian-basis sets for molecular calculations. 1. 2nd row atoms, $Z=11-18$. *Journal of Chemical Physics*, 72:5639–48, 1980.
- [198] Brundle, C. R. et al. Electronic Structure of NO₂ Studied by Photoelectron and Vacuumuv Spectroscopy and Gaussian Orbital Calculations. *The Journal of Chemical Physics*, 53(2):705–715, 1970.
- [199] Baltzer, P. et al. An experimental study of the valence shell photoelectron spectrum of the NO₂ molecule. *Chemical Physics*, 237(3):451–470, 1998.
- [200] Chang, H. B. and Huang, M. B. A Theoretical Study on the Electronic States and O-Loss Photodissociation of the NO₂⁺ Ion. *ChemPhysChem*, 10(3):582–589, 2009.
- [201] Harvey, A. G et al. An R-matrix approach to electron–photon–molecule collisions: photoelectron angular distributions from aligned molecules. *Journal of Physics B: Atomic, Molecular and Optical Physics*, 47(21):215005, 2014.
- [202] Bixon, M. and Jortner, J. Intramolecular Radiationless Transitions. *The Journal of Chemical Physics*, 48(2):715–726, 1968.
- [203] Jortner, J. et al. *Advances in Photochemistry*, pages 149–309. John Wiley & Sons, Inc., 2007.
- [204] Domcke, W. and Stock, G. *Advances in Chemical Physics*, pages 1–169. John Wiley & Sons, Inc., 2007.
- [205] Kinsey J L. Laser-Induced Fluorescence. *Annual Review of Physical Chemistry*, 28(1):349–372, 1977.
- [206] Armstrong, L. et al. Resonant multiphoton ionization via the Fano autoionization formalism. *Physical Review A*, 12:1903–1910, 1975.
- [207] Dixit, S. N. and Lambropoulos, P. Theory of photoelectron angular distributions in resonant multiphoton ionization. *Physical Review A*, 27:861–874, 1983.
- [208] Lin, C. Y., McCurdy, C. W., and Rescigno, T. N. Complex Kohn approach to molecular ionization by high-energy electrons: Application to H₂O. *Physical Review A*, 89:012703, 2014.
- [209] Toffoli, D. et al. Molecular frame and recoil frame photoelectron angular distributions from dissociative photoionization of NO₂. *The Journal of Chemical Physics*, 126(5):–, 2007.

- [210] Worth, A. G. and Cederbaum L. BEYOND BORN-OPPENHEIMER: Molecular Dynamics Through a Conical Intersection. *Annual Review of Physical Chemistry*, 55(1):127–158, 2004.
- [211] <https://ccpforge.cse.rl.ac.uk/gf/project/ukrmol-scripts/>.
- [212] Arasaki, Y. et al. Time-resolved photoelectron spectroscopy of wavepackets through a conical intersection in NO₂. *The Journal of Chemical Physics*, 132(12):–, 2010.
- [213] Feynman, R. P. Forces in Molecules. *Physical Review*, 56:340–343, 1939.
- [214] Hirst, D. M. Ab initio potential energy surfaces for excited states of the NO₂⁺ molecular ion and for the reaction of N⁺ with O₂. *The Journal of Chemical Physics*, 115(20):9320–9330, 2001.
- [215] Carr, J. M. et al. UKRmol: a low-energy electron- and positron-molecule scattering suite. *European Physics Journal D*, 66:58, 2012.
- [216] Fang, T. K. and Ho, Y. K. Strong electric-field effects on the structure profiles of doubly excited resonances in He ground-state photoionization. *Physical Review A*, 60:2145–2150, 1999.
- [217] Chung, K. T., Fang, T. K., and Ho, Y. K. Resonances of helium in a DC field. *Journal of Physics B: Atomic, Molecular and Optical Physics*, 34(2):165, 2001.
- [218] Harries, J. R. et al. Double Photoexcitation of Helium in a Strong dc Electric Field. *Physical Review Letters*, 90:133002, 2003.
- [219] Sàthe, C. et al. Double Excitations of Helium in Weak Static Electric Fields. *Physical Review Letters*, 96:043002, 2006.
- [220] Kips, A., Vassen, W., Hogervorst, W., and Dando, P. A. Scaled-energy spectroscopy of helium $|M| = 1$ Rydberg atoms in a static electric field. *Physical Review A*, 58:3043–3050, 1998.
- [221] Morgan, H. D. and Ederer, D. L. Photoionization cross section of helium for photon energies 59-67 eV: The $(sp, 2n+)^1P^o$ Rydberg series of autoionizing resonances. *Physical Review A*, 29:1901–1906, 1984.
- [222] Heslar, J. and Chu, S. I. *Ab initio* study of high-lying doubly excited states of helium in static electric fields: Complex-scaling generalized pseudospectral method in hyperspherical coordinates. *Physical Review A*, 86:032506, 2012.
- [223] Y. K. Ho. Electric-field effects on the 2p2 3Pe and 3Po states of H- below the H(N=2) threshold. *Journal of Physics B: Atomic, Molecular and Optical Physics*, 28(18):4025+, 1995.
- [224] Halka, M. Effects of static electric field on the photoionization spectra of two-electron atoms and ions. *Radiation Physics and Chemistry*, 75:2228, 2006.
- [225] Tennyson, J. and Noble, C. J. RESON—A program for the detection and fitting of Breit-Wigner resonances. *Computer Physics Communications*, 33(4):421–424, 1984.

- [226] Dunning, T. H. Gaussian basis sets for use in correlated molecular calculations. I. The atoms boron through neon and hydrogen. *The Journal of Chemical Physics*, 90(2):1007–1023, 1989.
- [227] Harvey, A. G. *Electron Re-scattering from Aligned Molecules using the R-matrix Method*. PhD thesis, 2010.
- [228] Ott, C. et al. Reconstruction and control of a time-dependent two-electron wave packet. *Nature*, 516(7531):374–378, 2014.
- [229] Woon, D. E. and Dunning, T. H. Gaussian basis sets for use in correlated molecular calculations. IV. Calculation of static electrical response properties. *The Journal of Chemical Physics*, 100(4):2975–2988, 1994.
- [230] Oza, D. H. Phase shifts and resonances for electron scattering by He^+ below the $N=2$ threshold. *Physical Review A*, 33:824838, 1986.
- [231] Nakata, M. The MPACK (MBLAS/MLAPACK); a multiple precision arithmetic version of BLAS and LAPACK. 2010.
- [232] McCurdy, C. W., Baertschy, M., and Rescigno, T. N. Solving the three-body Coulomb breakup problem using exterior complex scaling. *Journal of Physics B: Atomic, Molecular and Optical Physics*, 37(17):R137, 2004.
- [233] McCurdy, C. W., Horner, D. A., Rescigno, T. N., and Martín, F. Theoretical treatment of double photoionization of helium using a B -spline implementation of exterior complex scaling. *Physical Review A*, 69:032707, 2004.
- [234] Simon, B. The definition of molecular resonance curves by the method of exterior complex scaling. *Physics Letters A*, 71(2–3):211–214, 1979.
- [235] Halley, M. H., Delande, D., and Taylor, K. T. The combination of R-matrix and complex coordinate methods: application to resonances in the diamagnetic Rydberg spectrum of Li. *Journal of Physics B: Atomic, Molecular and Optical Physics*, 25(21):L525, 1992.
- [236] M. Yu. Ivanov. Coulomb corrections and polarization effects in high-intensity high-harmonic emission.
- [237] Baker, S. et al. Probing proton dynamics in molecules on an attosecond time scale. *Science*, 312(5772):424–427, 2006.
- [238] Vozzi, C. et al. Controlling two-center interference in molecular high harmonic generation. *Physical Review Letters*, 95:153902, 2005.
- [239] P Salières et al. Imaging orbitals with attosecond and Ångström resolutions: toward attochemistry? *Reports on Progress in Physics*, 75(6):062401, 2012.
- [240] Levesque, J. et al. Polarization state of high-order harmonic emission from aligned molecules. *Physical Review Letters*, 99(24):243001, 2007.
- [241] Pedatzur, O. et al. Attosecond tunnelling interferometry. *Nature Physics*, 11(10):815819, 2015.

- [242] Lein, M. et al. Role of the intramolecular phase in high-harmonic generation. *Physical Review Letters*, 88(18):183903, 2002.
- [243] Kanai, T., Minemoto, S., and Sakai, H. Quantum interference during high-order harmonic generation from aligned molecules. *Nature*, 435:470–474, 2005.
- [244] Zhou, X. et al. Molecular recollision interferometry in high harmonic generation. *Physical Review Letters*, 100:073902, 2008.
- [245] Li, W. et al. Time-resolved dynamics in N_2O_4 probed using high harmonic generation. *Science*, 322:1207–1211, 2006.
- [246] Smirnova, O. Private communications.
- [247] Haessler S. et al. Attosecond imaging of molecular electronic wavepackets. *Nature Physics*, 6(3):200–206, 2010.
- [248] Mairesse, Y. et al. Attosecond Synchronization of High-Harmonic Soft X-rays. *Science*, 302(5650):1540–1543, 2003.
- [249] Homeier, H. H.H. and Steinborn, E. O. Some properties of the coupling coefficients of real spherical harmonics and their relation to Gaunt coefficients. *Journal of Molecular Structure (Theochem)*, 368:31–37, 1996.